UNIVERSITY OF CRETE

DEPARTMENT OF MATERIALS SCIENCE

MASTER THESIS

BY: Minoas C. Chairetis

***SUPERVISOR**: Professor Pavlos Savvidis*

Committee members: Professors: Pavlos Savvidis, Constantinos Stoumpos, Nikolaos Pelekanos

Fabrication and characterization of 2D Halide Perovskite Crystals for Polaritonic Devices

Microelectronics Research Group (MRG)

Table of Contents

Table of Figures

Εισαγωγή

Στη διατριβή αυτή, ο κύριος στόχος ήταν να δημιουργηθεί μία χημική συνταγή για τη δημιουργία δισδιάστατου κρυστάλλου περοβσκίτη αλογονιδίου και επίσης μια τεχνική επεξεργασίας τελευταίας τεχνολογίας, προκειμένου να ενσωματωθεί σε οπτικές κοιλότητες. Δύο μέθοδοι χρησιμοποιήθηκαν για να δημιουργηθεί όσο το δυνατόν καλύτερης ποιότητας κρύσταλλος: η μέθοδος υγρής αποφολίδωσης (Liquid Exfoliation) και η μέθοδος διαλύματος (Solution method). Χρησιμοποιώντας τεχνικές όπως XRD και εικόνες μικροσκοπίας/SEM, χαρακτηρίσαμε επιτυχώς τη δομή των υλικών και με οπτικές μετρήσεις όπως τη φωτοφωταύγεια (Photoluminescence), την ανακλαστικότητα (Reflectivity), όπως και μετρήσεις θερμοκρασιακής εξάρτησης και εξάρτησης ισχύος ακτινοβολίας, εξήγαμε δεδομένα σχετικά με την εξιτονική εκπομπή του υλικού. Η μέθοδος υγρής αποφολίδωσης δεν ήταν επιτυχής λόγω της παραγωγής φθαρμένων κρυστάλλων και πολύ μεγάλου πάχους, και προκειμένου να εισαχθεί ο περοβσκίτης σε κοιλότητες, χρειαζόμασταν λεπτότερο πάχος κρυστάλλου, καθώς και καθαρή και μεγάλη εξιτονική εκπομπή. Η δεύτερη μέθοδος μας παρείχε πολύ καλύτερα αποτελέσματα τόσο στο σχήμα όσο και στη δομή των υλικών όσο και στην εξιτονική τους εκπομπή. Με το υλικό να βελτιστοποιείται με επιτυχία, ενσωματώθηκε σε δύο τύπους οπτικών κοιλοτήτων σε θερμοκρασία δωματίου. Ο πρώτος τύπος ονομάζεται "ανοιχτή-κοιλότητα", ο οποίος αποτελείται από ένα «Κατανεμημένο Ανακλαστήρα Μπραγκ» (Distributed Bragg Reflector-DBR) με τον κρύσταλλο περοβσκίτη στην κορυφή. Με λευκό φως, χτυπήσαμε το DBR υπό γωνία 89 μοιρών για να δημιουργήσουμε ένα πολωμένο οπτικό τρόπο ταλάντωσης κοντά στην εξιτονική εκπομπή του κρυστάλλου και να εξερευνήσουμε την αλληλεπίδρασή τους. Αυτή η τεχνική μας παρέχει πλεονεκτήματα, όπως λιγότερα βήματα ανάπτυξης λόγω της ανάγκης για μόνο για μια δομή DBR και παράγει επίσης μόνο έναν οπτικό τρόπο ταλάντωσης, συμπεριφερόμενο σαν μία πολύ μικρού πάχους κοιλότητα. Τέλος, χρησιμοποιήσαμε το βελτιωμένο υλικό σε μία κλασσική DBR μικροκοιλότητα και με επιτυχώς δημιουργήσαμε πολαριτονική κατάσταση σε θερμοκρασία περιβάλλοντος.

Abstract

The main aim of this work was to fabricate high quality thin 2D Halide perovskite crystals and use them to demonstrate strong light-matter coupling in various device geometries. We explored two alternative methods to fabricate crystals, namely, liquid exfoliation and solution method. We characterized the material structure using XRD as well as microscope/SEM techniques and employ optical measurements such as PL, Reflectivity, Power and Temperature dependence, to characterize exciton emission properties in this material. Liquid exfoliation method produced relatively small sized perovskite crystals not compatible with their introduction inside wavelength sized cavity. The second method, provided us with the much better results both in crystal size and structure as well as excitonic emission. The successfully optimized material was then incorporated inside optical cavity and on top of a Bragg reflector. Large angle white light reflectivity measurements at room temperature revealed the appearance of resonant mode residing at the surface of the Bragg mirror whose coupling with overlaying perovskite excitons was studied. Finally, strong-light matter coupling at room temperature was obtained when incorporating such crystals inside DBR mirror-based cavities demonstrating the great promise these materials pose for real world polaritonic applications.

1 Theoretical background

1.1 Introduction

Perovskite crystals have emerged as promising materials in the realm of advanced photonics and optoelectronics. Their exceptional optical properties and versatile synthesis methods have opened new avenues for cutting-edge device applications. This thesis explores the synthesis of perovskite crystals and their potential role in the development of polaritonic devices, where light and matter interact in unique and powerful ways.

In the pages that follow, we will analyze and describe perovskite crystal synthesis, diving into their chemical composition, crystal structure, and methods for optimizing the material. Afterwards, we go into the fundamental principles of polaritons, which are hybrids of light and matter, and examine how perovskite crystals can be introduced into different types of cavities in order to achieve polariton state.

1.2 Light – Electromagnetic waves

Light is a fundamental phenomenon in physics. It is the result of the oscillation of electric and magnetic fields as they propagate through space. These oscillations occur perpendicular to the direction of light's travel, constituting a transverse wave. Light exhibits both wave-like and particle-like characteristics, which is known as wave-particle duality. This duality is a cornerstone of quantum mechanics and is exemplified by the behavior of light, where photons, discrete quanta of light, exhibit both wave interference patterns and particle-like energy quantization. Light is characterized by its wavelength and frequency, with different wavelengths giving rise to the visible spectrum of colors. The electromagnetic spectrum encompasses a broad range of light, including radio waves, microwaves, infrared, visible, ultraviolet, X-rays, and gamma rays, each with distinct properties and applications [1,2]

1.2.1 Polarization

Polarization of light is a fundamental aspect of lights behavior that is closely tied to the orientation of the oscillating electric and magnetic fields within an electromagnetic wave. To understand polarization, we need to recognize the relationship between the direction of these oscillations and the direction of wave propagation. When we have linear polarization, we speak about two polarizations, s and p. [3,4]

When light propagates in a vacuum, it is unpolarized, which means that it can be described as a mix between the two linear polarizations s and p. Unpolarized, light has an equal amount of power in each two linear polarizations.

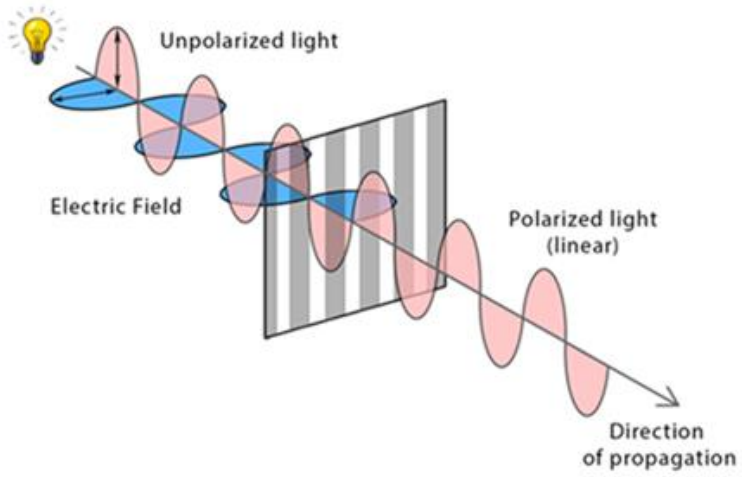

FIGURE 1-1: LIGHT AS AN ELECTROMAGNETIC WAVE

Display of light as an electromagnetic wave as well as its 2 polarizations. Both polarizations are perpendicular to the axis of propagation (usually z-axis). The two-polarization propagating perpendicularly to the z-axis are the Transverse Electric (TE) Polarization (p) and Transverse Magnetic (TM) Polarization (s). After going through a linear polarizer that is put correctly only for one of the two polarizations to be allowed through, exactly that happens and we can only observe the polarization desired.

Image source: ScienceFacts.net/Polarization of Light

1.2.2 Fresnel equations – S and P polarizations

To put the two linear polarizations into perspective, we need to assume a situation of light hitting an interface. Let's assume a light ray that hits a plane of incidence at an angle θ (**Fig 1-2**). S and P polarizations refer to the plane in which the electric field of light is oscillating. S polarization -also called Transverse Electric (TE)- is the linear polarization component of the wave that is normal to the plane of incidence and P polarization -also called Transverse Magnetic (TM)- is the component parallel to the plane of incidence. To quantify these statements, we can use the Fresnel equations. These equations describe the reflection and transmission amplitudes of light when it hits a surface between two mediums. By applying the boundary conditions of electromagnetic waves that require that E and B components parallel to an interface to be continuous at the interface. The formulas that describe them are:

$$r_s = \frac{n_1 \cos(\theta_1) - n_2 \cos(\theta_2)}{n_1 \cos(\theta_1) + n_2 \cos(\theta_2)} \qquad \text{EQ. 1-1}$$

S component

$$t_s = \frac{2n_1 \cos(\theta_1)}{n_1 \cos(\theta_1) + n_2 \cos(\theta_2)} \qquad \text{EQ. 1-2}$$

$$r_p = \frac{n_2 \cos(\theta_1) - n_1 \cos(\theta_2)}{n_2 \cos(\theta_1) + n_1 \cos(\theta_2)} \qquad \text{EQ. 1-3}$$

P component

$$t_p = \frac{2n_1 \cos(\theta_1)}{n_2 \cos(\theta_1) + n_1 \cos(\theta_2)} \qquad \text{EQ. 1-4}$$

Where r is the reflection coefficient (reflected amplitude divided by incident amplitude) and t is the transmission coefficient (transmitted amplitude divided by incident amplitude)

Although reflection and transmission are dependent on polarization, for normal incidence there is no distinction between them so all polarization states have a single set of Fresnel coefficients.

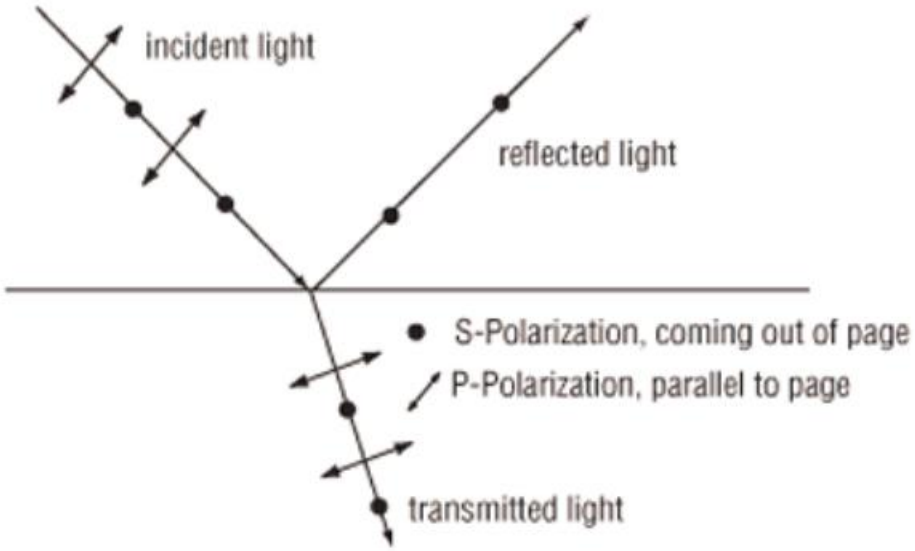

FIGURE 1-2 : S AND P POLARIZATIONS OF LIGHT

When referring to polarization states, the s component refers to the polarization plane perpendicular to the plane of incidence. S polarization is also called Transverse Electric. P polarization refers to the polarization plane parallel to the plane of incidence. P polarization is also called TM

1.2.3 Brewster Angle

In 1815, Sir David Brewster conducted experiments using superior-quality materials and successfully demonstrated that this angle indeed depended on the refractive index, a principle now known as Brewster's law [5,6]. The Brewster angle, denoted as θ_B, plays a significant role in optics, particularly when dealing with the interaction of light with dielectric surfaces [7]. It represents the angle of incidence at which the reflected light is completely polarized parallel to the surface, while there is no reflected light in the perpendicular plane. This phenomenon can be described by the Brewster's Law equation:

$$\tan(\theta_B) = \frac{n_2}{n_1} \qquad \text{EQ. 1-5}$$

Here, θ_B is the Brewster angle, n_1 is the refractive index of the first medium (typically the dielectric material), and n_2 is the refractive index of the second medium (often air). Brewster's law is directly derived from Snell's Law:

$$n_1 \sin(\theta_1) = n_2 \sin(\theta_2) \qquad \text{EQ. 1-6}$$

The Brewster angle is not only a fundamental optical concept but also finds practical applications. It is frequently employed to reduce glare from glass surfaces, such as in anti-reflective coatings for eyeglasses or camera lenses and can also be a very practical in optical setups and measurements.

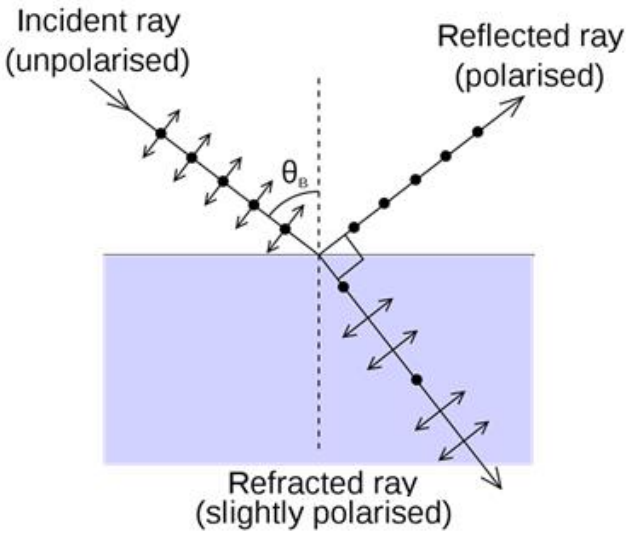

FIGURE 1-3: BREWSTER ANGLE

Image representing how the angle of incidence plays a crucial role onto the genera light manipulation. As seen, unpolarized light coming from medium 1 -usually air- hits the interface and the reflected light becomes almost completely polarized, due to the angle of incidence being the critical Brewster angle, creating a 90^0 angle between refracted and reflected rays.

Image source: Wikipedia/Brewster's Angle

1.3 Semiconductors

A solid material whose electrical properties lie between those of a conductor and an insulator is called a semiconductor. These materials, often composed of elements from groups III and V or II and VI in the periodic table, possess unique electrical properties that lie between those of conductors and insulators. Under appropriate conditions, it can either conduct or block the flow of current based on specific requirements. Semiconductors are what an engineer would use to manipulate current flow in a system for example. In every solid material, there are approximately 10^{23} atoms per cubic centimeter, and their electrons occupy different energy levels. Due to interactions with neighboring atoms, the energy levels of electrons combine and integrate. This results in the formation of multiple non-discrete bands (**Fig.1-4**) with each band filling up with electrons until it reaches its maximum capacity. The last level that is occupied in this manner is called the Fermi level and the energy of the last occupied level in a Fermi system at a given temperature is called Fermi energy. In semiconductors, the Fermi level is located between the energy bands. The band just below the Fermi level is filled with electrons and is called the Valence Band, while above the Fermi level, there are bands that lack electrons, with the lowest of these called the Conduction Band.

Between the Valence Band and the Conduction Band, there is a region where electron states are not allowed. The energy difference between the upper limit of the Valence Band and the lower limit of the Conduction Band is called the energy gap, and it is the energy required for an electron to move from the Valence Band to the Conduction Band. As an electron jumps from the Valence Band to the Conduction Band, it leaves behind a vacant position that can be considered as a new particle with the same effective mass as the electron but with opposite charge. This particle is called a hole. In essence, to manipulate a material that falls under the umbrella of semiconductors, we just need to provide a certain amount of energy – that energy being of various types such as an electric field or a laser pump- and from there, multiple devices such as transistors, computational chips etc. can be produced [8].

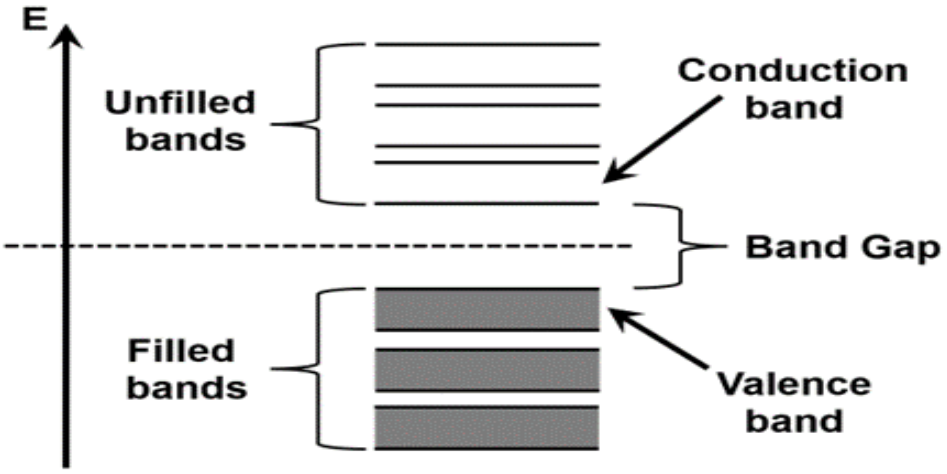

FIGURE 1-4: SEMICONDUCTOR

Simple representation of a semiconductor band structure. Electrons fill the bands resulting at the last electron filled band that is called "valence band". When energy is introduced into this system – either optical or electrical-, the electrons go to the upper band, called the "conduction band". Between the valence and conduction band, there is gap, which represents the amount of energy the system needs for an electron to go to the conduction band.

Image source: Collins, Philip G. and Avouris, Phaedon. Scientific American. Nanotubes for Electronics. Retrieved April 5, 2006.

1.4 Excitons

Excitons, as quasiparticles in semiconductors, arise from the strong interaction between an excited electron and the resulting hole in the valence band [9]. When an electron absorbs energy and transitions from the valence band to the conduction band, a positively charged hole is formed. The electron and hole, despite being physically separated, are electrically attracted to each other due to their opposite charges. This attraction leads to the formation of an exciton – a quasi-particle with distinct properties from those of an individual electron or hole. The interaction between the two charges results in the creation of an excitonic state, where the electron orbits the hole in a fashion similar to how an electron orbits the nucleus in a hydrogen atom. The energy released during the formation of this bound state is the binding energy. The binding energy of an exciton, denoted as $\mathbf{E_b^n}$, quantifies the strength of this binding.

Binding Energy

The binding energy of an exciton can be determined by the equation [8-11]:

$$\mathbf{E_b^n} = -\frac{\mathbf{R^*}}{\mathbf{n^2}} \qquad \text{EQ. 1-7}$$

where n represents the principal quantum number and R* corresponds to the effective Rydberg energy given by:

$$\mathbf{R^* = \frac{\mu e4}{2\hbar^2(4\pi\varepsilon_0\varepsilon)^2}} \qquad \textbf{EQ. 1-8}$$

With $\boldsymbol{\mu = [(m_e^*)^{-1} + (m_h^*)^{-1}]^{-1}}$ being the reduced mass of the electron (m_e) and hole (m_h) system, $\hbar$ the reduced Planck constant, e the charge of an electron, ε the relative permittivity of the material.

The principal quantum number describes the spatial distribution and energy of the excitonic wave function. The negative sign in Equation 1 indicates the attractive Coulomb interaction between the electron and hole, resulting in a bound state.

The total energy of an exciton, denoted as E_x, can be expressed as the difference between the bandgap energy (E_g) and the binding energy (E_b):

$$\mathbf{E_X = E_G - E_B = E_G - \frac{R^*}{n^2}} \qquad \textbf{EQ. 1-9}$$

The Bohr Radius is:

$$\boldsymbol{\alpha_{ex}^b = \alpha_b^H \frac{R_0^*}{R^*\varepsilon_r}} \qquad \textbf{EQ. 1-10}$$

With:

- $\boldsymbol{\alpha_{ex}^b}$ **= Exciton Bohr radius**
- $\boldsymbol{\alpha_b^H}$**=5.29*10^{-11}m Hydrogen Bohr radius**
- $\boldsymbol{R_0^*}$ **= 13.6 eV → Rydberg energy**
- $\boldsymbol{\varepsilon_r}$ **= general permittivity**

This equation reflects that the exciton energy lies below the energy of an unbound electron-hole pair by the amount of the binding energy. The exciton energy is influenced by the material's bandgap and the specific quantum state of the exciton. When an exciton cannot retain its energy, it undergoes a process called exciton relaxation or decay. This can happen through several mechanisms, including radiative and non-radiative processes.

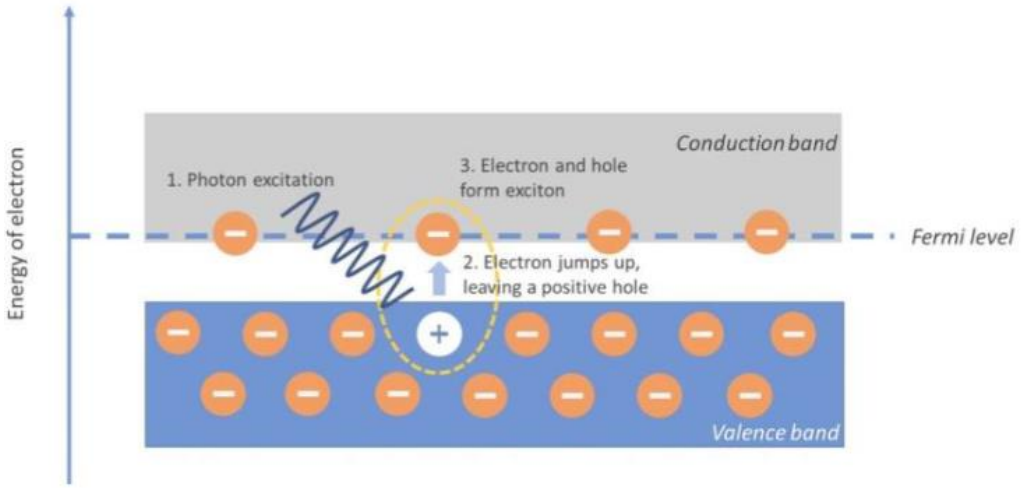

FIGURE 1-5: EXCITON STATE

This figure presents a simple representation of how an exciton is "created". A form of energy – be it light or electric current- passes through the medium, exciting electrons from the valence band enough to overcome the bandgap energy and as such go to the conduction band. The interaction between electron in the conduction band and hole in the valence band is what is called an exciton.

Image Source: Fast-moving excitons observed for first time in metal, unlocking potential to speed up digital communication by City University of Hong Kong

Photoluminescence (PL)

Photoluminescence is a phenomenon in which a material absorbs photons (light particles) and then re-emits them as light of a longer wavelength, typically in the visible or near-infrared range. This process involves the absorption of energy by the material's electrons, which causes them to transition from lower-energy states to higher-energy states. Subsequently, these electrons return to lower-energy states by releasing the excess energy in the form of photons, leading to the emission of light. Photoluminescence is a key concept in understanding the behavior of materials in various scientific and technological applications, including semiconductors, nanomaterials, and biological systems [8,12].

As the excited electrons return to their lower-energy states, they recombine with the holes. During this recombination process, the excess energy acquired during excitation is released as photons. These emitted photons have longer wavelengths (lower energy) than the absorbed photons, as the energy difference between the initial and final states of the electrons is preserved in the form of light energy. The emitted photons are detected as light emission,

leading to a photoluminescence signal. The color (wavelength) of the emitted light depends on the energy levels involved in the electronic transitions and the band structure of the material.

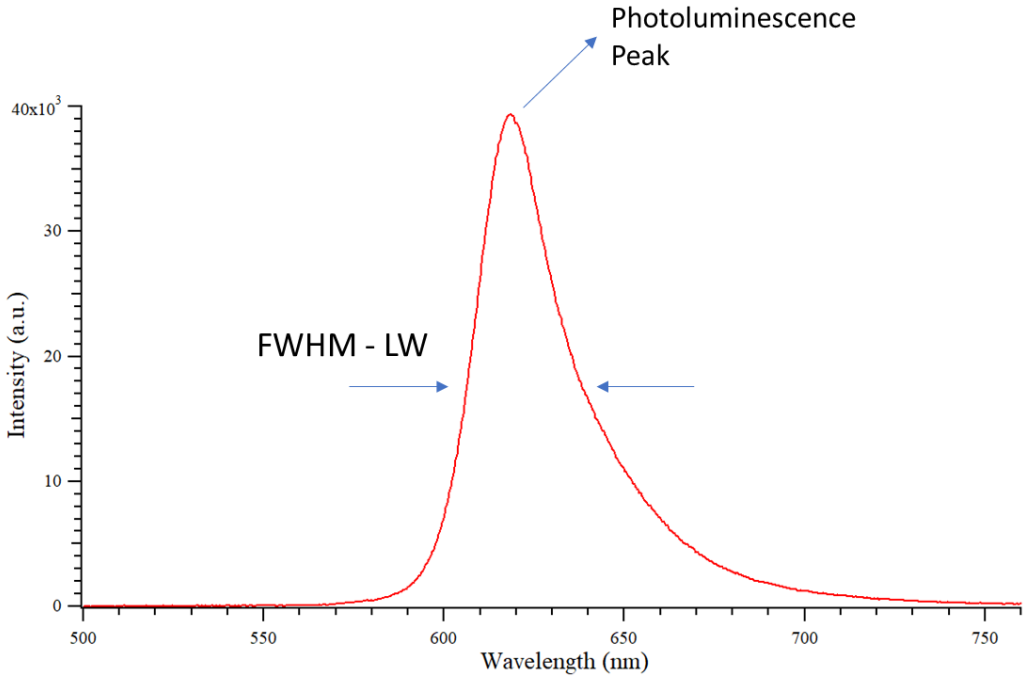

FIGURE 1-6: PHOTOLUMINESCENCE (PL)

Photoluminescence representation displaying the basic characteristics. The peak of the PL curve displays the wavelength of the exciton emission and the Linewidth of Full Width Half Maximum displays the stability of the emission. Linewidth is interconnected with the Binding Energy of the exciton and as such, the narrower the curve, the more stable the emission.

1.5 Quantum Wells

To further illustrate and calculate an electron-hole interaction (exciton), we can consider a simple quantum well (QW). Put simply, QWs are typically a sandwich structured by a thin layer (~ nm) of a semiconductor (e.g., GaAs) between two layers (of equal thickness) of another semiconductor (e.g., AlGaAs), **Fig.1-7**. We assume that the perpendicular direction to the layers is the z axis. In addition, we take as granted that the bandgap of semiconductor A (Eg_A) is smaller than B (Eg_B) [8,13]. This basically creates a containment. Because of the bandgap difference, a QW is created in the GaAs region and low energy carriers are confined. For the basic QW model the general solved wavefunction is:

$$\Psi_n(z) = \sqrt{\frac{2}{L}}\sin(k_n z) \quad \text{WITH } K_N = \frac{n\pi}{L} \qquad \text{EQ. 1-11}$$

With:

- **L = QW thickness**
- **k = wavevector of each state**
- **n = principal quantum number (n > 0)**

- **L = thickness of QW**

From the wavefunction, we can derive the discrete energies of the system:

$$E_n = \frac{\hbar^2 k_n^2}{2m_\omega^*} = \frac{\hbar^2}{2m_\omega^*}\left(\frac{n\pi}{L}\right)^2 \qquad \text{EQ. 1-12}$$

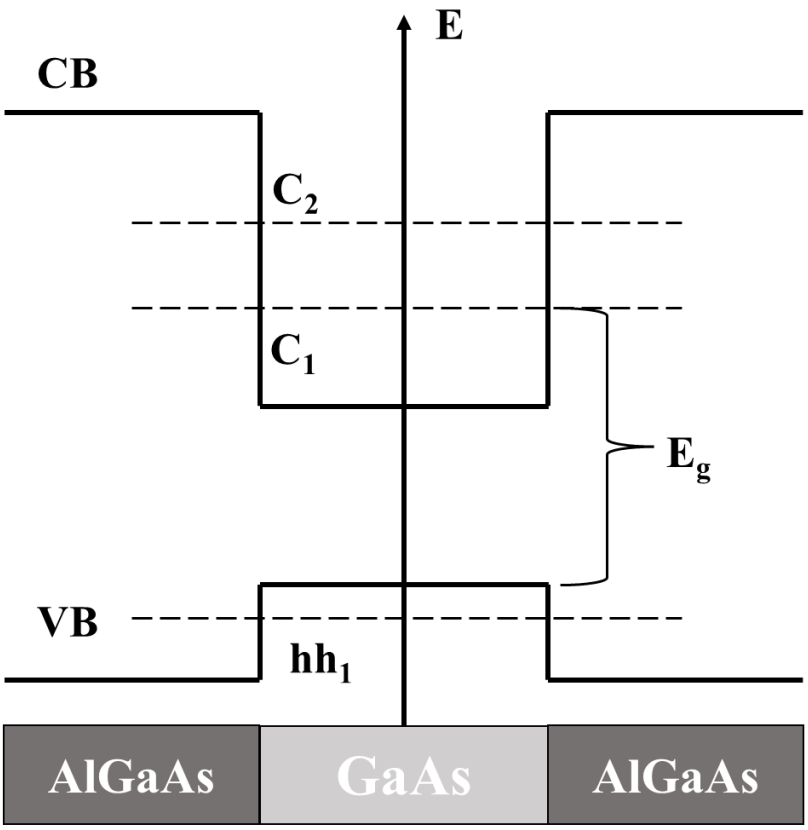

FIGURE 1-7: SCHEMATIC REPRESENTATION OF A QUANTUM WELL

This is schematic image of what a quantum well looks like. Like semiconductor theory, the Valence Band is below, also showing the heavy hole. The two AlGaAs layers act as potential barriers for the GaAs layer in between, making excited electron able to only go into the C1 or C2 states as the don't have enough energy to go further, making them confined spatially.

1.6 Fabry-Perot Cavities

Optical (micro)cavities have generally been developed for the purpose of successfully confining light, therefore increasing the photon life inside it and by that increasing the interaction of it with the active medium. Specifically, we will focus on the Fabry-Perot

architecture. Initially introduced by Charles Fabry and Alfred Perot for interferometric analyses, this cavity consists of two planar mirrors which are as parallel as possible and between them a certain medium. If the mirrors possess high reflectivity properties, the light fringes become sharper and this can be then employed in high-resolution spectral analyses. Through the years, this architecture became a very useful tool for laser setups as a passive optical structure able to tune emission properties embedded inside. In the figures below, we see an optical representation of this system [8,14].

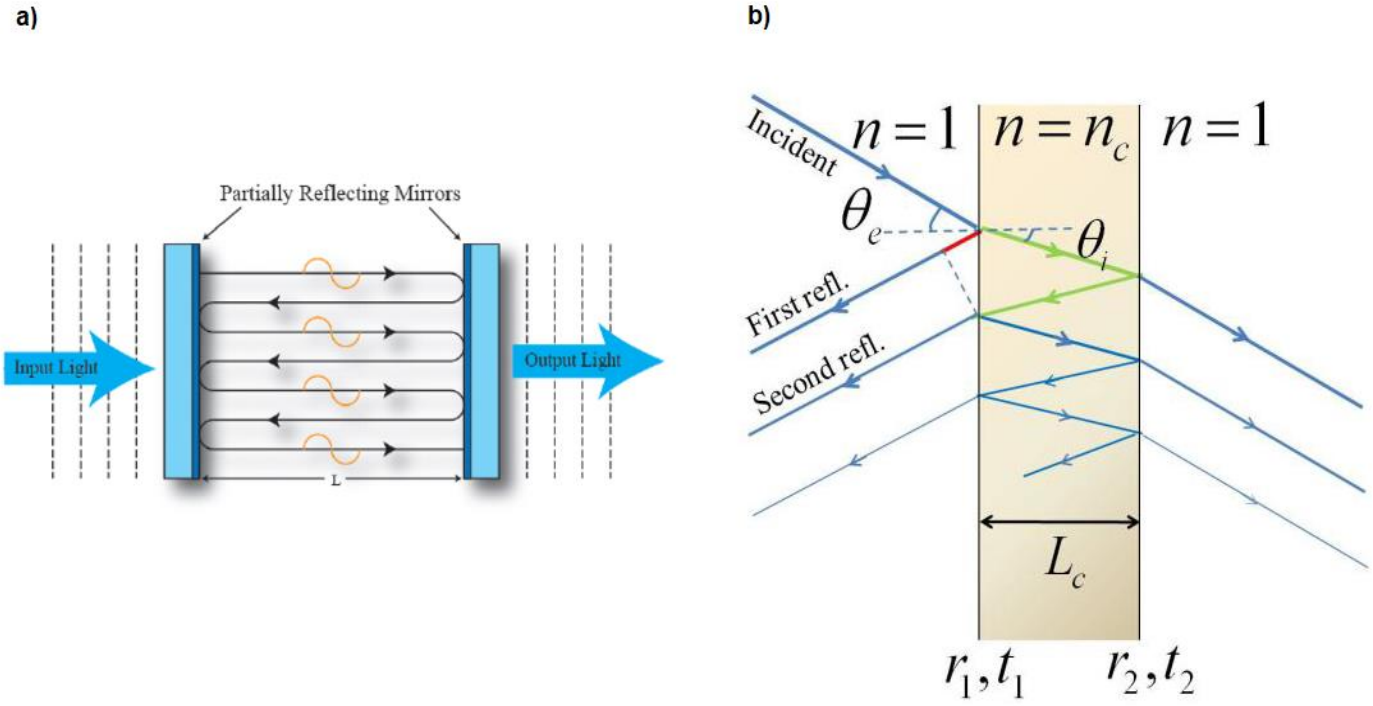

FIGURE 1-8: FABRY-PEROT CAVITY-CONSTRUCTIVE INTERFERENCE
Both pictures exhibit essentially how a mode is realized inside a cavity. Light which is confined between two high quality mirrors and undergoes constructive interference which consequently realizes the mode.
Image source: [8]

In the figures above, we can see the path of light inside the cavity. As seen in figure b, light passes inside the cavity and if the adjustments (cavity thickness, refractive indices of mirrors and correct geometry), light constructively interferes and losses decrease significantly. The whole reflectivity obeys the following equation:

$$\mathbf{R_c + T_c = 1} \qquad \textbf{EQ. 1-13}$$

With R_c being reflectance and T_c transmission. By calculating the reflectivity through transfer matrix, we show in the figure below the reflectivity minima (or transmission maxima) which correspond to optical resonant modes confined in the cavity. These modes are characterized by:

$$\mathbf{k_0\delta = 2q\pi} \qquad \textbf{EQ. 1-14}$$

With:

- $\mathbf{k_0 = \frac{2\pi}{\lambda}}$
- $\mathbf{\delta = 2n_c L_c \cos(\theta_i)}$ → **light path inside the cavity times the medium's refractive index (n_C).**
- **q being an integer.**

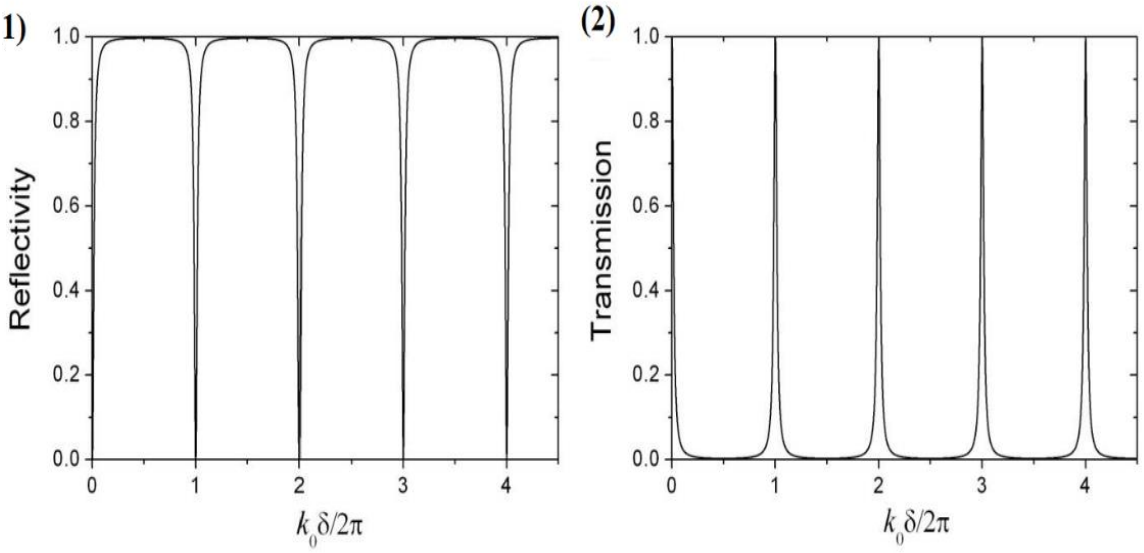

FIGURE 1-9: CAVITY MODES

Simulation of the cavity modes in both a reflectivity and a transmission measurement. In a cavity, reflectivity (resp. transmission) is ideally almost 1 (resp. 0) and the mode reaches almost zero (resp. 1).
Image source: [8]

In a dispersion measurement the energy of the cavity modes is shown in the figure below:

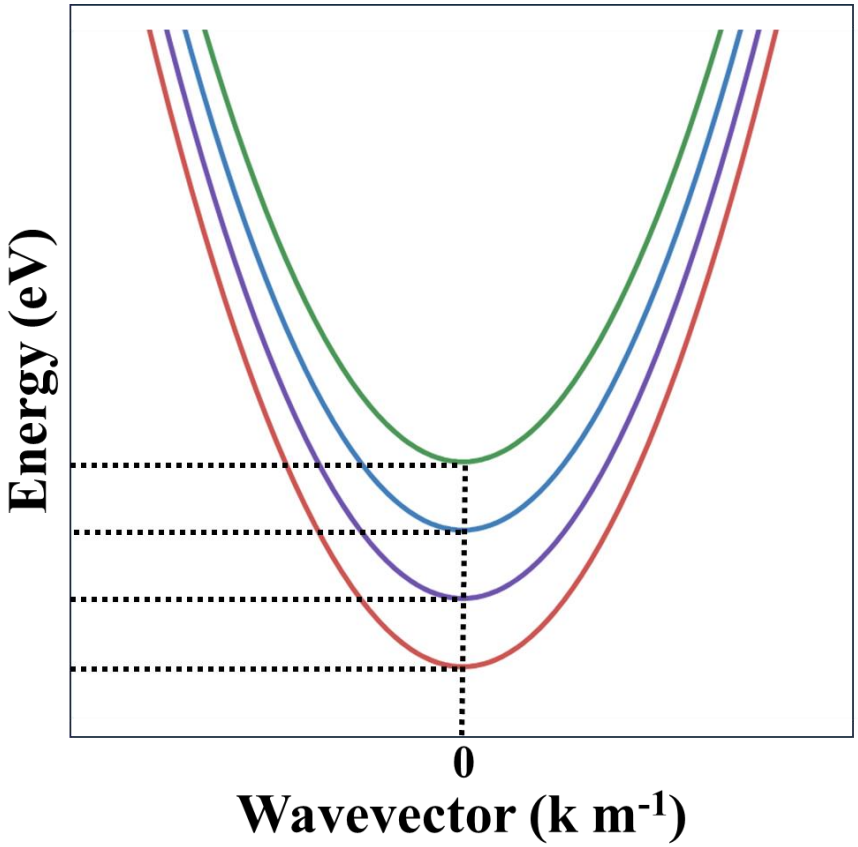

FIGURE 1-10: DISPERSION REPRESENTATION OF CAVITY MODES

This plot, is a schematic of an angular dispersion in an optical cavity. There are 4 modes in total all having different Energies at zero momentum. To find the thickness of this cavity we need only to follow two consecutive energy modes and fine their zero momentum energy values. With the cavity's refractive index known, we have all the necessary information about the thickness of the cavity.

Followed by their equation

$$E(K) = E_{m,ph} + \frac{H^2 k^2}{2m^*_{ph}} \qquad \text{EQ. 1-15}$$

$$m_{ph} = \frac{m\pi H n_c}{cL_c} \qquad \text{EQ. 1-16}$$

- **m_{ph} = photon mass**
- **m = mode number**
- **n_c = cavity refractive index**
- **L_C = Cavity thickness**

As follows from the equations, the refractive index plays an immediate role to the curvature of the modes.

The cavity's thickness L_c is calculated from the following equation:

$$L_c = \frac{\lambda_1 \lambda_2}{2n(|\lambda_1 - \lambda_2|)} \qquad \text{EQ. 1-17}$$

- **λ_1,λ_2 = consecutive wavelength peaks**
- **n = refractive index of the medium**

1.6.1 Q-Factor

The Q factor refers to the quality factor of a resonant optical system. It characterizes the behavior of optical resonators, such as optical cavities, microcavities, and photonic crystal structures. The Q factor in optics is analogous to the Q factor in other fields, like electronics and mechanics, but it pertains specifically to the behavior of light waves [8,**Error! Reference source not found.**].

The Q factor in optics is a measure of the efficiency and selectivity of an optical resonator in trapping and circulating light at a specific wavelength. It quantifies how well the resonator can store and sustain light within its structure before the light energy is lost due to absorption or scattering. A higher Q factor indicates a resonator that can store light for a longer time and over a narrower range of wavelengths.

Mathematically, the Q factor in optics is defined as:

$$Q = \frac{\omega_c}{\Delta\omega} = \frac{E_c}{\Delta E} \approx \frac{\lambda_c}{\Delta\lambda} \qquad \text{EQ. 1-18}$$

Where E, λ represent the photon energy and wavelength respectively. When $\boldsymbol{\lambda_c \gg \Delta\lambda}$, the ≈ approximation is valid. Conclusively, the Q-factor measures efficiency in the optical by taking into account the FWHM. As it becomes narrower, the quality of the cavity increases.

1.7 Distributed Bragg Reflectors (DBRs)

A Distributed Bragg Reflector (DBR) serves as a fundamental building block within optics, notably in lasers and photonic systems, facilitating the creation of efficient mirrors targeted at specific light wavelengths. It is constructed by strategically layering two distinct materials, each characterized by a different refractive index. These layers are meticulously engineered to harness a pronounced reflective effect within a particular range of wavelengths. It takes form

through the alternation of layers comprising two materials, each distinguished by its unique refractive index. Usually, one material exhibits a higher refractive index (referred to as the high-index material), while the other manifests a lower refractive index (referred to as the low-index material). As light transitions across the interface between materials with distinct refractive indices, a portion of the light is reflected, and another part is transmitted. This reflected light engages in constructive or destructive interference, contingent upon the layers' thicknesses and refractive indices. This interaction gives rise to a series of closely spaced reflection peaks, with each peak corresponding to a specific wavelength. For constructive interference to manifest, the following equation must be obeyed [8,15].

$$\mathbf{d} = \frac{\boldsymbol{\lambda}}{\mathbf{4n}} \qquad \text{EQ. 1-19}$$

where:

- **d = layer thickness**
- **λ = Bragg wavelength**
- **n = Refractive index**

1.7.1 Transfer Matrix Method

To craft a DBR, firstly simulation is needed. The usual simulation is called “Transfer Matrix Method (TMM)”. The transfer matrix method is a mathematical approach that simplifies the analysis of electromagnetic wave interactions with layered structures. In this approach, every layer is symbolized by a transfer matrix that elucidates alterations in the electric field of light upon entry and exit from the layer. This matrix factors in the layer's refractive index and thickness. By sequentially multiplying these matrices for each layer within a multi-layer arrangement, it becomes possible to compute how the characteristics of light evolve as it traverses the complete stack. In the figure below, there is a simulated DBR of ten pairs of TaO5/SiO2 and the same system but with air medium in between showing the cavity mode [8**Error! Reference source not found.**].

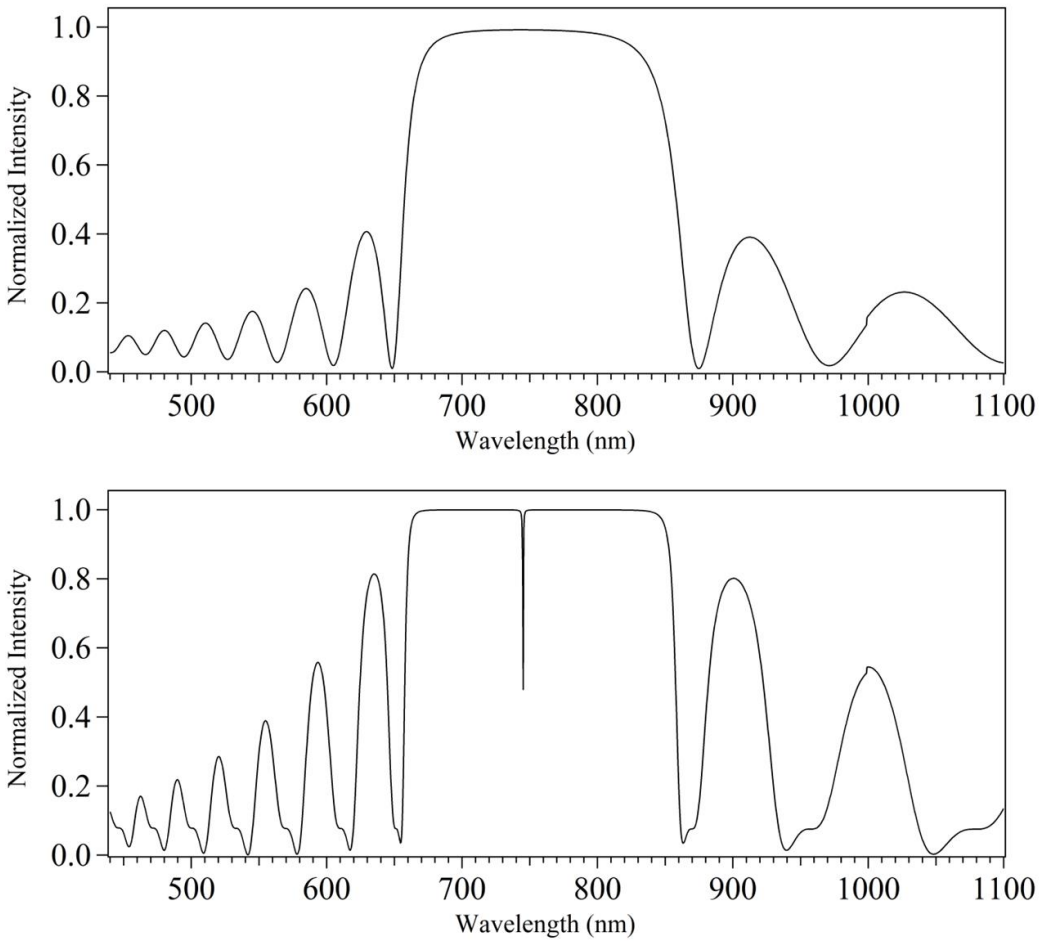

FIGURE 1-11: DISTRIBUTED BRAGG REFLECTOR (DBR)

10 Pair (TaO5/SiO2) DBR reflectivity simulations.

a) Representation of a DBR reflectivity displaying the Bragg modes as well as the distinct stopband where reflectivity tends to go to 1 with center wavelength at 745 nm.

b) Representation of a DBR cavity. In a cavity, two DBRs are facing each other and with correct thickness, a resonant mode at appears at the middle of the stopband.

1.8 Exciton – Polaritons

Polaritons are pseudo-particles formed by the coupling of electromagnetic waves and the excitation of electric dipoles. They are created when photons (modes) and excitons undergo strong coupling. Due to imperfections in the crystalline system, polaritons are destroyed at the crystal's surface attributed to light losses and weak coupling with excitons. In semiconductor microcavities, polaritons are created with the coupling of the cavity's photon (mode) and a significantly larger exciton, resulting in an observable longer lifetime. Due to the microcavity's properties, there are considerably fewer photon losses, leading to more frequent couplings and therefore more polaritons. These polaritons exhibit both light-like and matter-like properties. They behave as bosons, which makes them potentially condense into a macroscopic state known as Bose-Einstein condensation. If the coupling is weak, it can be treated as a simple perturbation, and the system can be approximated by photons and excitons without interaction, known as weak coupling. Conversely, if the coupling is strong, referred to as “strong coupling interaction”, the system includes interaction between photons and excitons. The resulting new pseudo-particle is called a polariton, describing this particular state [8].

In a microcavity, the exciton-photon detuning is defined as $\delta = Ec - Ex$, where Ec is the independent energy of the photon in the cavity and Ex is the independent energy of the exciton. The detuning changes experimentally either by changing the temperature or by altering the cavity's thickness. In weak coupling, in absorption measurements of the system, as the energy of the photon approaches that of the exciton, we observe that the absorption peaks of the two entities merge without interacting and simply put, “pass each other by”. In strong coupling however, there is a minimum energy distance between the two peaks due to the now robust interaction. This minimum distance is called **Rabi splitting = $\hbar\Omega$**. This behavior is experimental evidence of polariton creation. Representing this behavior on an energy-detuning diagram reveals two distinct branches of the polariton, the Upper Polariton Branch (UPB) and Lower Polariton Branch (LPB), and this is called anti-crossing. Examples of such diagrams are shown below."

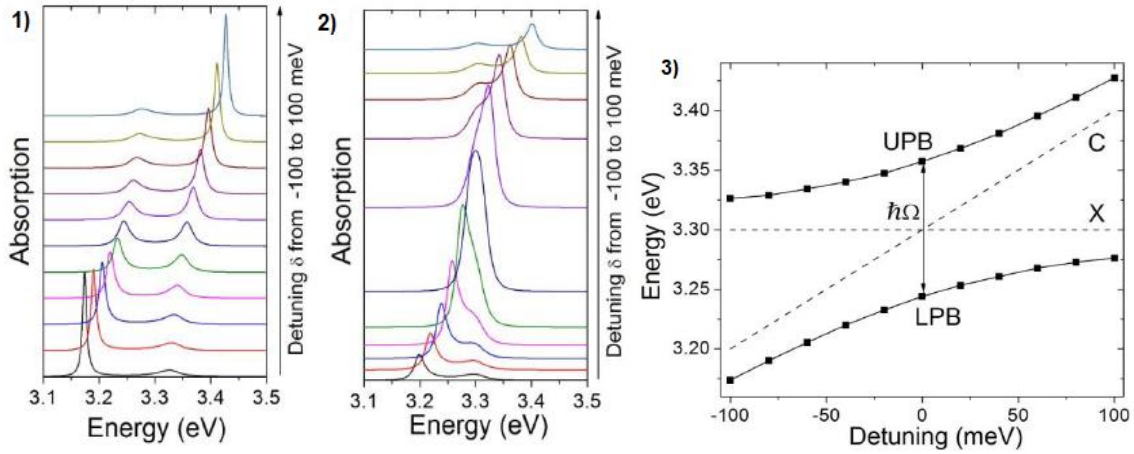

FIGURE 1-12: WEAK AND STRONG COUPLING REGIME

a, b) Plot onto the right is displaying a system abiding by the strong coupling regime realizing a polariton. What is seen is that one peak stays frozen in one place and the other is steadily progressing towards it. At a certain energy distance (Rabi splitting), the two peaks do not approach each other anymore due to their robust interaction (strong coupling). On the contrary, when the interaction of the entities is weak, it is seen through the two peaks simply interchanging.
c) In this figure, with dashed lines is displayed the strong coupling regime which is indicated through the exciton and photon lines crossing each other and on the other hand, the bold line presents an anticrossing, forming two polariton branches known as Upper Polariton Branch (UPB-Representing the exciton) and Lower Polariton Branch (LPB-Representing the photon).
Image source: [8]

1.8.1 Quantum description of Exciton-Photon Coupling

The quantum description of a polariton is based on electromagnetism. Initially, in its classical form, it treats photons as an electromagnetic field and excitons as dipole oscillators. The energy of the exciton is described through the dipole oscillator relationship. Subsequently, in its quantum form, the photon-exciton coupling is described as a coupled oscillator, ignoring exciton-exciton interactions. It assumes that the exciton and the photon have known wave vectors k, and their states are $|X_k>$ and $|Ph_k>$, respectively, with $\mathbf{a_k^\dagger}$ και $\mathbf{b_k^\dagger}$ being the creation and annihilation operators, respectively. Based on these, the Hamiltonian describing the system – without considering the photon-exciton interaction yet – is:

$$\mathbf{H_k^0 = E_X(k) b_k^\dagger b_k + E_{ph}(k)\, \alpha_k^\dagger a_k} \qquad \text{EQ. 1-20}$$

Where $\mathbf{E_X}$ and $\mathbf{E_{ph}}$ are the energies of the exciton and the photon for wave vector k, respectively. The eigenstates of $\mathbf{H_k^0}$ can be written as $|\mathbf{n_k^X}, \mathbf{n_k^{ph}}>$, where $\mathbf{n_k^X}$ and $\mathbf{n_k^{ph}}$ are the numbers of excitons and photons in the system, respectively. These states are called "bare" states, as they describe non-coupled particles with independent physical properties. The interaction between exciton and photon also includes optical transitions, with their Hamiltonian being:

$$\mathbf{H_k^{int} = g(b_k^\dagger a_k + \alpha_k^\dagger b_k)} \qquad \text{EQ. 1-21}$$

Where $\mathbf{b_k^\dagger a_k}$ (respectively $\boldsymbol{\alpha_k^\dagger b_k}$) represents the absorption of the photon (emission respectively) and $\boldsymbol{\alpha_k^\dagger b_k}$ represents the exciton creation (destruction respectively).

The systems complete Hamiltonian is as follows:

$$\mathbf{H_k = H_k^0 + H_k^{int} = E_X(k) b_k^\dagger b_k + E_{ph}(k) \alpha_k^\dagger a_k + g(b_k^\dagger a_k + \alpha_k^\dagger b_k} \quad \textbf{EQ. 1-22}$$

Now we reform the Hamiltonian in a matrix form as such:

$$\begin{pmatrix} \mathbf{E(k)_X} & \mathbf{g} \\ \mathbf{g} & \mathbf{E(k)_{ph}} \end{pmatrix}$$

Through this matrix, the energy eigenvalues can be obtained:

$$\mathbf{E_{LP}(k) = \frac{E_X(k) + E_{ph}(k)}{2} - \frac{\sqrt{(E_X(k) - E_{ph}(k))^2 + 4g^2}}{2}} \quad \textbf{EQ. 1-23}$$

$$\mathbf{E_{UP}(k) = \frac{E_X(k) + E_{ph}(k)}{2} + \frac{\sqrt{(E_X(k) - E_{ph}(k))^2 + 4g^2}}{2}} \quad \textbf{EQ. 1-24}$$

With those energies' normalized eigenvectors being:

$$\mathbf{(C_X(k)\ C_{ph}(k))} \text{ AND } \mathbf{(C_{ph}(k)\ -C_X(k))} \quad \textbf{EQ. 1-25}$$

In which we have:

$$\mathbf{C_X(k) = \frac{1}{\sqrt{1 + (\frac{E_{LP}(k) - E_X(k)}{g})^2}}} \quad \textbf{EQ. 1-26}$$

$$\mathbf{C_{ph}(k) = \frac{1}{\sqrt{1 + (\frac{g}{E_{LP}(k) - E_X(k)})^2}}} \quad \textbf{EQ. 1-27}$$

For **zero detuning** and **k = 0**,

$$\mathbf{E_{UP}(0) - E_{LP}(0)} = h\Omega$$

With **Ω** being the **Rabi splitting**.

From these equations we have $E_{LP}(k)$ and $E_{UP}(k)$ being the Lower Polariton Energy branch (LP) and Upper Polariton Energy branch (UP) and these energies are effectively the eigenenergies of the coupled system. The two coefficients $C_X(k)$ and $C_{ph}(k)$ are known as the Hopfield coefficients and they obey the following equation

$$\mathbf{|C_X(k)|^2 + |C_{ph}(k)|^2 = 1} \quad \textbf{EQ. 1-28}$$

From **eq. 1.23**, the states $||LP_k>> = ||1,0>>$ and $||UP_k>> = ||0,1>>$ can be re-expressed as:

$$\mathbf{||LP_K>> = C_X(k)|X_K> + C_{ph}(k)|P_{HK}>} \quad \textbf{EQ. 1-29}$$

$$||UP_K>> = C_{ph}(k)|X_K> - C_X(k)|P_{HK}> \quad \text{EQ. 1-30}$$

Therefore, the $|C_X(k)|^2$ and $|C_{ph}(k)|^2$ are fractions of the exciton (photon, respectively) and photon (exciton, respectively). Below, a diagram is shown with the Hopfield coefficients as a function of detuning, as well as an energy - wavevector diagram illustrating the distinct energies of the polaritons (UPB and LPB) for zero detuning. Such an energy - momentum diagram with two separate branches serves as further evidence for the existence of polaritons in experimental measurements of angular dispersion.

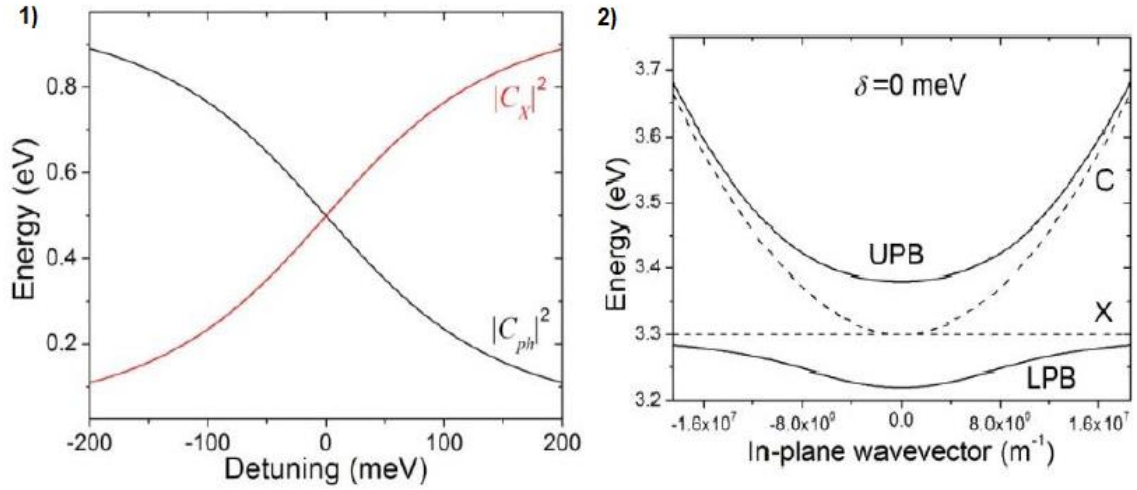

FIGURE 1-13:POLARITON STATE – HOPFIELD COEFFICIENTS

This figure exhibits the Hopfield coefficients of exciton (RED) and Photon (Black) in a plot of Energy vs Detuning.
Angular Dispersion of lower and upper polariton branches in a microcavity at zero detuning (Dashed Lines) and positive detuning (Bold Lines).
Image source: [8]

2 2D MATERIALS

Two-dimensional materials, including graphene, carbon nitride, and pseudo-2D materials, have gained attention in research circles due to their wide-ranging applications in optics, sensing, energy, electronics, and more. These materials exhibit unique characteristics owing to their distinct dimensions, leading to variations in their optical and electrical properties due to electron confinement. Moreover, a notable feature is their exceptionally high surface-to-bulk ratio,

Primarily, these materials consist of sheet-like layers, characterized by strong hydrogen bonds within the plane and comparatively weaker van der Waals bonds perpendicular to it. Consequently, they manifest many intriguing properties and have a good degree of adjustability [17-19].

2.1 Perovskite Crystals – Properties

Following up, this work means to introduce methods of optimization of perovskite crystals through chemical syntheses, fabrication and growth techniques.

With origins in the 19th century, Perovskite crystals derive their name from a mineral boasting a similar crystal arrangement. Their history within materials science is substantial, and they have garnered recognition for their exceptional traits and practical uses. This traces back to their discovery in the Ural Mountains of Russia, credited to Lev Perovski, a Russian mineralogist, in 1839 [20]. However, it wasn't until the later part of the 20th century that researchers began delving into the potential of perovskite oxides across various technological domains.

A pivotal moment for perovskite crystals occurred during the 1980s, when certain perovskite oxide compounds exhibited high-temperature superconductivity [21]. This discovery uncovered the material's intriguing and unconventional optoelectronic characteristics, like tunable bandgap energies, large room temperature excitonic emissions and used multiple methods of fabrication [22-24].

2.1.1 Perovskite structure and optical properties (3D vs 2D)

Perovskites in general possess multiple properties that are mainly derived from their structural properties as well as fabrication manipulation. Initially discovered as an ore, with characteristic formula $CaTiO_3$ and orthorhombic structure.3D halide perovskites have the molecular formula ABX3, where A represents organic or inorganic monovalent cations (e.g., MA+, FA+, Cs+), B is divalent cations within the cubic crystal, and X stands for halogens (Cl−, Br−, I−). General, 3D perovskite structures exhibit low binding energy and due to their bulky nature, it is difficult to implement them in for optical devices. However, their 2D counterpart is proving to obtain more useful properties. The formation of a 2D perovskite involves the introduction of an organic functional group into a 3D perovskite. This is achieved by adopting a Ruddlesden-Popper crystal structure with the chemical formula$(RNH_3)_2A_{n-1}\,B_nX_{3n+1}$, where 'n' can be any integer (1, 2, 3, 4, and so on). In this structure, $(A_{n-1}B_nX_{3n+1})^{2-}$represents a conducting layer derived from the original 3D perovskite, such as cesium lead iodide ($CsPbI_3$) [25]. This

conducting layer is effectively separated or isolated by R-NH_3, which is a large aliphatic or aromatic alkyl ammonium spacer cation. Examples of spacer cations include butylammonium (BA) and phenethylammonium (PEA). When 'n' equals infinity ($n = \infty$), it corresponds to a typical 3D perovskite structure. When 'n' is equal to 1 ($n = 1$), it signifies a pure 2D structure, and for intermediate values of 'n,' it represents a quasi-2D structure [26-28]. In contrast to 3D perovskites, 2D perovskites exhibit an enhanced hydrophobicity in their structure, primarily attributed to the organic spacer cation. Additionally, these spacer cations can decelerate secondary reactions, rendering the material less susceptible to moisture. Furthermore, the nearly constant conductivity within the perovskite conductor layer, along with the conductive insulation provided by the organic spacer layer, gives rise to a naturally occurring multiple quantum well structure [29,30]. Here, the organic spacer layer serves as a "barrier," while the perovskite layer acts as a "reservoir." When a 2D material is stimulated, the confinement effect leads to an increase in binding energy, resulting in the formation of excitons rather than electrons and holes. Experiments have also demonstrated a preference for charge migration along the iodide surface, known as "well transfer." Reducing the value of 'n' reveals distinct exciton absorption and peak emission phenomena, causing a blue shift.

Furthermore, 2D layered perovskites break free from the constraints of the tolerance factor concept, offering remarkable structural adaptability [31]. The continuous adjustability of exciton absorption and excitation energy, achieved through the quantum confinement effect by altering parameters like 'n' and 'R' [32-34], proves their versatility.

Lastly, a standout advantage of 2D perovskites over their 3D counterparts lies in their adaptability through the molecular design of the spacer cation. Alterations such as changing the ammonium ion, varying the alkyl chain length, or introducing π-conjugated fragments enable a wide spectrum of applications for 2D perovskites, driven by their diverse photoelectric properties and compositional design possibilities.

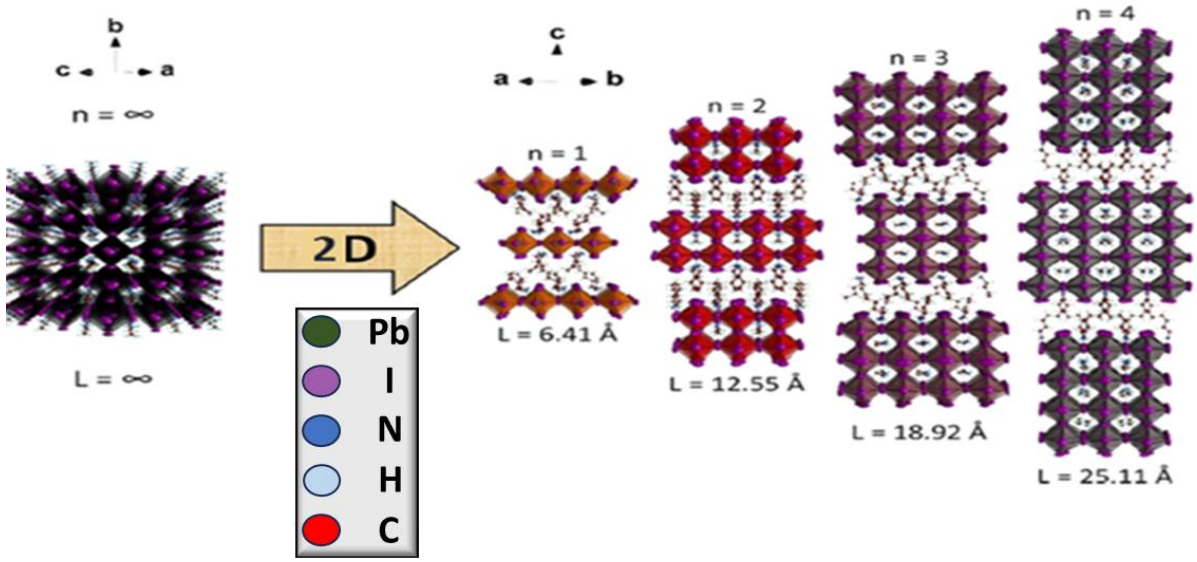

FIGURE 2-1:3D VS 2D LEAD IODIDE PEROVSKITE CRYSTAL

3D Perovskites vs 2D Perovskites. The crystal in its 3D form can be forced into self-assembly onto a 2D structure by introducing a suitable organic compound. This organic material acts as "molecular scissor", and invades between the perovskite, making it assemble into layers. Image source: [27]

2.1.2 Perovskite QWs

As mentioned, 2D perovskites possess the interesting property of being natural quantum wells due to their structure. This allows through chemical fabrication tuning, to adjust optical properties such as exciton binding energy – through spacer changes- and also photoluminescence wavelength tune – through the n value-. [27,33]

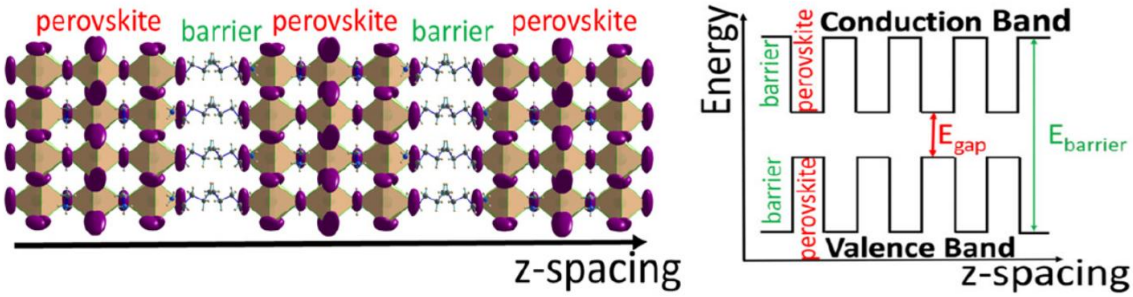

FIGURE 2-2: QUANTUM WELL CORRELATION WITH PEROVSKITE STRUCTURE

Perovskite structure performing as a natural Quantum Well. The crystal structure is inorganic and has a natural V that is less than the organic barrier, hence the ability of the perovskite structure to confine electrons in plane.
Image source: [27]

2.1.3 Perovskite Optical characteristics

As shown below (**Fig. 2-3,2-4**), by tuning the crystals chemical synthesis, we can achieve different exciton emissions and with ease so as to match the demands of what the experiment needs. For example, if the needs of an excitonic peak is at around 650 nm, the crystal can be simply made with different chemical components with the same chemical synthesis and simply adjust the individual amounts of reactants used. By doing this, the crystal's structure will now have 4 layers between the organic barrier and the "QW" now possesses different thickness, thus producing the different excitonic emission needed. As such, the new crystal can now obey the different demands of the system [25].

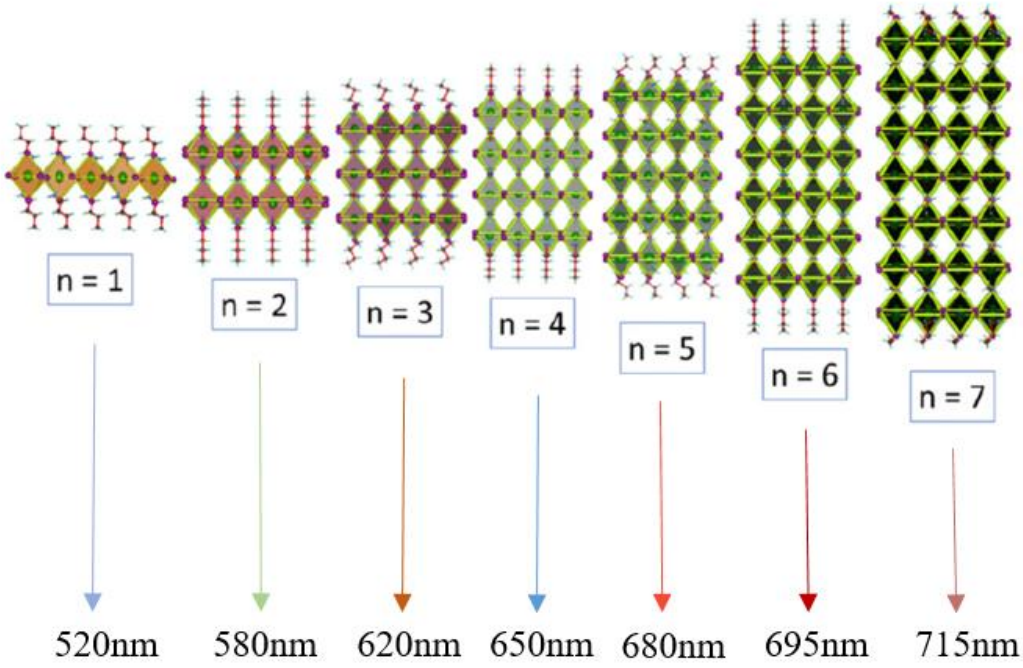

FIGURE 2-3: PEROVSKITE "N" STRUCTURES WITH CORRESPONDING EXCITON EMISSIONS

2D structure of Perovskite Crystal for different n values. As mentioned, n values can be tuned through tinkering of the initial synthesis formula, therefore changing the thickness of the QWs. This has as a result, different exciton energies and as such, emissions. Image source: [25]

Further evaluation of the optical properties of the 2D perovskite crystal in **Fig. 2-4**. As exhibited, the perovskite crystal's behavior -be it in 3D or 2D- does not depend on the "n" value. This means that we expect the same optical behavior -emission wavelengths peaks of course are different- between the different crystal's regardless of their initial "n" character. We also observe that the absorption of the perovskite has a small energy difference ranging from 10-15 nm regarding its PL exciton peak. This is assigned to the Band gap of the different n crystals [27]. Finally, the sharp absorption edges of the crystals suggest direct band gap.

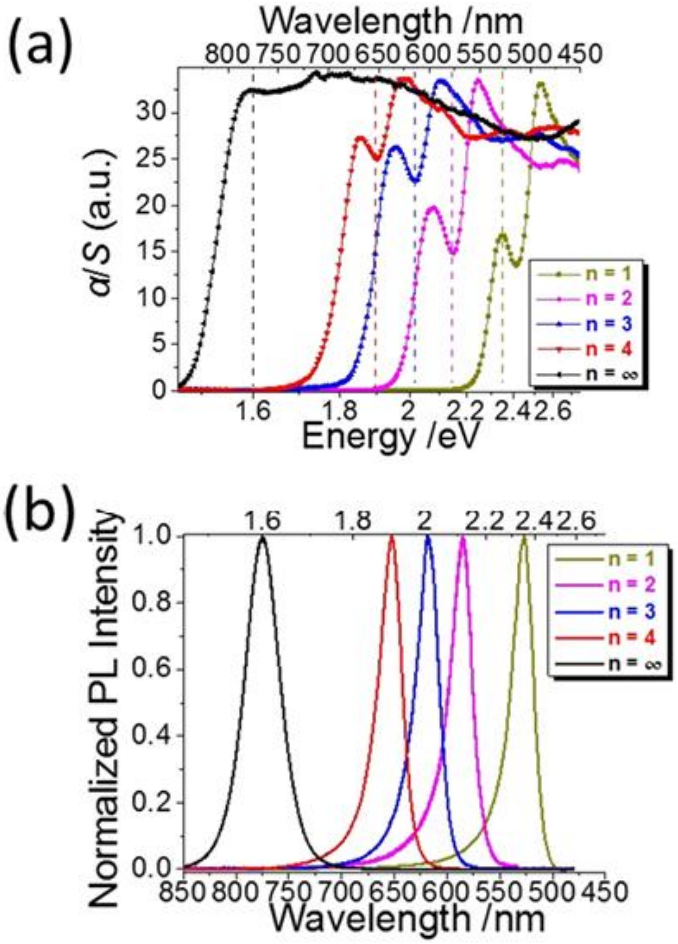

FIGURE 2-4: PHOTOLUMINESCENCE PEROVSKITE CRYSTALS N = 1-7

Different Pl and Absorption spectra for multiple values of n. By changing the formula of the perovskite, we can achieve different values of n and thus achieving easily, tunable exciton emission. In addition to this, we also observe that the crystal's optical behavior is hardly "n" dependent meaning that in both PL and Absorption spectra, the optical behavior of the perovskite is basically the same regardless of its "n" value. The n = ∞ value indicates 3D structure.

Image source: [27]

2.1.4 Perovskite Reflectivity

The reflectivity of perovskite materials depends on various factors such as the composition, crystal structure, and surface morphology. In general, perovskite materials exhibit high reflectivity in the visible and near-infrared regions due to their high refractive index and low absorption coefficient. However, the reflectivity can be affected by the presence of defects, impurities, and surface roughness, which can lead to scattering and absorption of light [35-39]. The crystal in general is uniaxial [35], which adds its birefringence into the equations. This ultimately means that, the reflectivity measurements will change according to what polarization we are collecting into the measurement itself.

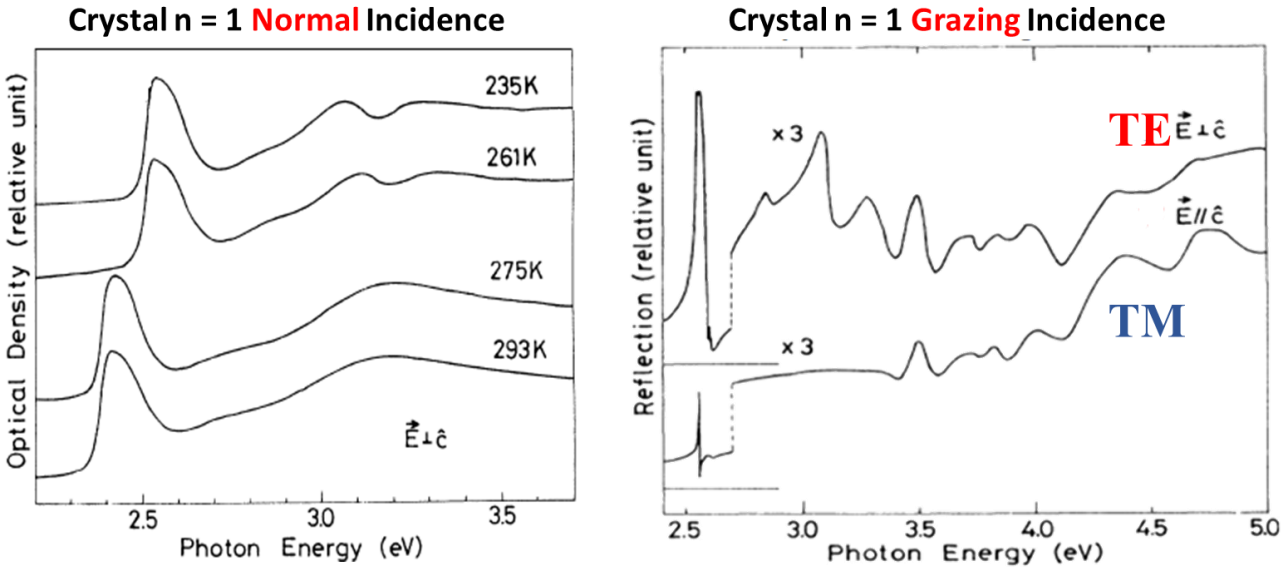

FIGURE 2-5: PEROVSKITE CRYSTAL N = 4 REFLECTIVITY MEASUREMENTS FOR NORMAL AND GRAZING INCIDENCE

Reflectivity measurements in a perovskite of n = 4 value in both room and low temperature. (a): Room temperature reflectivity at normal incidence depicting that the signal has both crystal reflectance and exciton nature. (b) Low temperature and polarization dependent measurements at grazing incidence suggesting that for perpendicular polarization (TM), intensity rises and sharpness falls and vice versa for parallel polarization (TE). Finally, by comparing the room and low temperature measurements we deduct that the measurement signal is hard to acquire due to the crystal's scattering.
Image source: [37]

As indicated by Fig. 2-5, the reflectivity of the material, not only is extremely different at room temperature compared to its low temperature counterpart, but it also contains polarization preference [37,39]. In room temperature and with normal incident light (**Fig. 2-5 (a)**), the reflectivity of the crystal is like a peak, corresponding to both exciton and crystal reflection nature. Also, the first phase transition of the crystal is visible. In low temperature however, the situation changes dramatically. In **Fig. 2-5(b)**, we see the reflectivity measurement at grazing incidence and at 1.6 K. Due to the crystal's high scattering property, the reflectivity signal had to be times 3 so as to be included into the plot visibly. This proves that the crystal surface can -and will- most likely be rough, making it difficult to collect the signal. Furthermore, we can see the polarization dependance as well. In the upper curve of (b), the polarization vector is

perpendicular to the growth axis of the crystal (meaning TM Polarization) and we can see that its intensity is high and its sharpness low. In the other curve, the polarization is parallel to the growth axis (meaning TE Polarization) and from this is seen that the intensity falls significantly but the sharpness gets better. Finally, we can safely suggest, that the perovskite's optical behavior possesses minor changes in behavior corresponding to "n" values. Important distinction, the perovskite reflectivity is in general much easier to measure under low temperature environments.

2.1.5 Temperature Dependence and Phase transitions

Another interesting property that arises from the different n values, is the structural change that births from different temperatures in which the crystal is introduced. Taking for example the n = 3 crystal structure, we can clearly see that upon arriving temperature of approximately T = 150 K, there is a clearly visible blue shift as the perovskites PL goes from ~ 620 nm to ~ 610 nm. This is called a "phase transition" [27,40]. Near room temperature environments, methylammonium halide perovskites (3D) are generally structured as orthorhombic. At the first phase transition, the structure of the 3D crystal undergoes a change, from cubic to tetragonal hence the change in its photoluminescence. Despite the fact that information is known about the 3D n = 1 crystal, the structural changes for the homologous n =1 -4 2D crystals are not yet fully known. Sure enough, we can know that these transitions exist due to their direct result in the optical behavior of the compounds. For, example, the n = 3 crystal displays 3 visible phase transitions:

1st: 270 K – PL Emission: ~615 nm

2nd: ~150 K – PL Emission: 600 nm

3rd: 50 K – PL Emission: ~ 610 nm

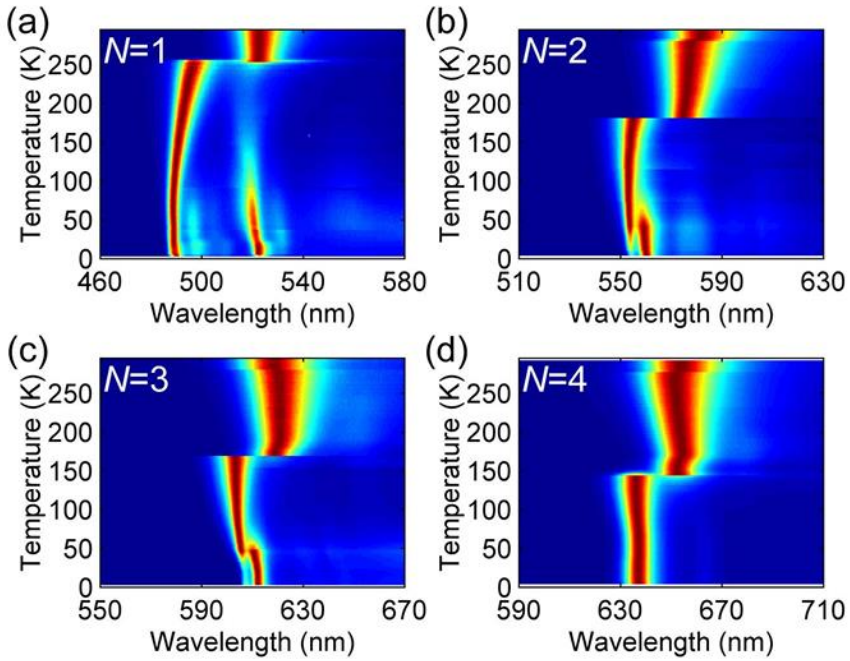

FIGURE 2-6: PEROVSKITE CRYSTAL N = 1-4 TEMPERATURE DEPENDENCE
Temperature Dependent Measurements for different n values of Perovskite. As it is seen from the plots, the perovskite structure depends on the temperature and we can optically observe this phenomenon through PL. For example, the n=3 perovskite makes a distinct phase transition at around 150K, abruptly shifting its emission from approx. 620 nm to 610 nm and another one at approximately 50K.
Image source: [25]

2.2 State of the Art

In 2023, polariton applications in general, represent a rapidly advancing field with significant potential. They have many applications like highly efficient polariton lasers, quantum information processing, nonlinear optics, sensing, quantum simulation, optomechanical applications and terahertz. [41-46]. Moreover, polaritons contribute to the exploration of fundamental physics and condensed matter science. One very interesting property of polariton states, is Bose-Einstein condensation (BEC) [47,48]. A wide variety of methods and techniques is being integrated for the realization of polariton states and BEC as well as numerous active mediums. One of the standard ways to realize polariton state is to implement a DBR microcavity with an active exciton medium material in between so as to have strong interaction between light and matter. Under this scope, a number of reliable material categories has come to be semiconductors like GaAs quantum wells and others [49,50]. In this point of view, there are many more materials able to successfully realize polariton states. Firstly, there is a variety of Transition Metal Dichalcogenides (TMDs) like MoS_2, WS_2 -both in room and low temperature environments,[51,54] as well as organic materials like organic dyes etc. [55,58]. Under the motivation of this thesis, one of the most upcoming materials is the perovskite crystal. Now the perovskites have been implemented in various types, structures and environments for polariton states as well as solar cells, transistors etc. Many works have been done in the perovskite n = 1 3D structure in both pure inorganic and hybrid organic-inorganic

forms at room and low temperature [59-63]. Moreover, there have been various works done in the perovskites n = 1 2D form for photovoltaics [64] as well as solar cells [65], transistors [66] and polaritonic devices [67,68]. In addition, work has been done in 0D perovskite crystal analyzation [69,70] for LEDs and/or detectors [71,74]. For the purposes of this thesis' motivation, there are more techniques so as to realize strong coupling regime like implementing the method of angle resolved – open cavity approach [75,76] which will be analyzed here with the active medium being 2D lead iodide perovskite as will the standard cavity method approach.

2.2.1 High – Angle strong coupling realization in DBR Half-Cavity

In addition to the standard cavity exciton-polaritons, there is another technique that can be implemented in order for a system to realize strong coupling regime. This application revolves around just one DBR and the medium either on top of it or QWs epitaxied between its layers [75]. In the standard version, to create a mode, you need two DBRs so as to create the electromagnetic resonance between them-a.k.a. mode-. But in this method, you can achieve a resonant evanescent mode onto the DBR at an angle of incidence approximately at 89^0. This high-angle incidence mode, can be accessed from the side of the DBR without any need for a prism or a grating and it is confined between the reflection of the interface of first layer of the DBR and the air above it. Surface Bloch waves (SBWs) have been a well-established phenomenon for an extended period. They manifest as localized waves occurring at the junction between a one-dimensional (1D) quarter-wave stack and an unbounded medium characterized by a lower refractive index, such as air. The initial theoretical descriptions delved into the study of entirely localized eigenmodes within semi-infinite multilayers. These descriptions considered solutions with exponential decay along the growth direction, both within the medium of lower refractive index (e.g., air) and within the multilayer structure itself. These modes are authentic interface modes, and as such, they are entirely confined within the multilayer structure, possessing in-plane wave vectors ($k_{\parallel}$) that extend beyond the boundaries defined by the light cone.

2.2.2 DBR wavelength shift vs Angle of Incidence

As the angle of incidence of the light gets larger, the reflectivity of a DBR will not remain the same [77,**Error! Reference source not found.**]. To understand that, we need to recall Snell's Law of refraction from **eq. 1-6** and the DBR's angular dependance from **eq. 1-14**.

Eq. 1-14: $\mathbf{k_0\delta = 2q\pi}$

In which **δ** has an angular dependence. As such when the optical path is at normal incidence, cos(θ) takes the value of 1 and basically ignored. But as the angle θ gets larger, cos(θ) cannot be neglected anymore and plays a role which increases in importance as the angles of incidence get bigger. The DBR's stopband starts blueshifting as the angles of incidence become larger and the Bragg modes start to become extinguished. This process is shown for 5 different angles of incidence in **Fig. 2-7**.

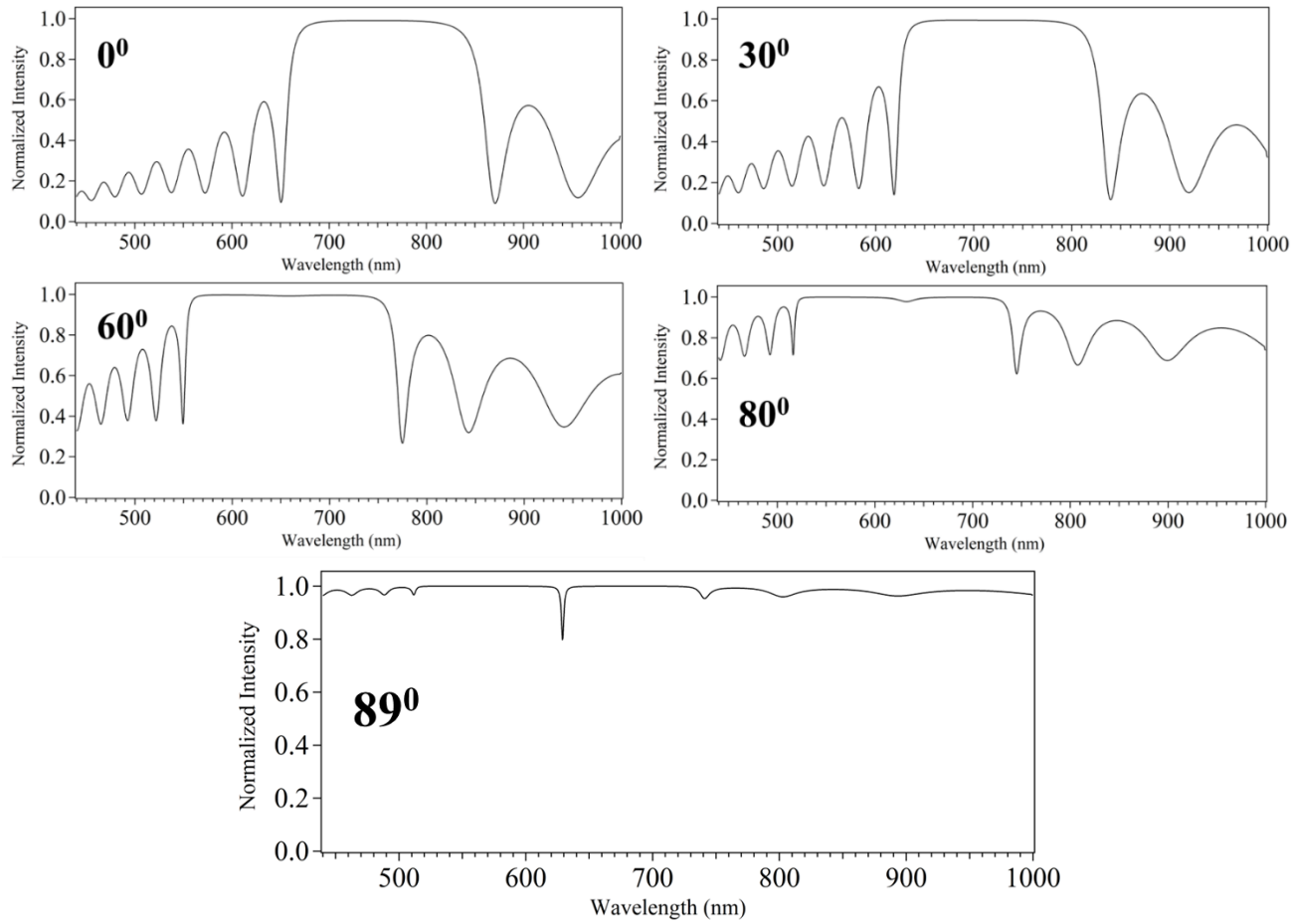

FIGURE 2-7: DBR VS ANGLE REFLECTIVITY SIMULATION

DBR Angular dependance reflectivity measurements simulation. As calculated, we exhibit through different angles of incidence, that the DBR reflectivity has a visible stopband blueshift as well as its Bragg modes clearly extinguishing because of the optical path's angular dependence. At 80^0, the resonant mode starts appearing because the reflectivity coefficients start getting close to π, thus having a phase shift which provides polarization dependent resonant mode.

2.2.3 Critical angle mode realization (Brewster-Cavity)

To delve into the content of this chapter, it is essential to establish a clear understanding of "Surface Bloch waves." These waves, also referred to as surface electromagnetic waves, represent a distinctive optical phenomenon that manifests at the interfaces of periodic structures like photonic crystals and diffraction gratings. Their emergence is the consequence of constructive interference among light waves at the surface of such structured materials. In contrast to bulk electromagnetic waves that freely traverse through open space, Surface Bloch waves remain confined to the material's surface, bearing unique characteristics. They are confined waves between a 1-dimensional quarter wave stack and a semi-infinite medium of lower refractive index. [79].

This system can basically be introduced a finite quarter wave stacked DBR and a mode that is confined on the first layer of it. At normal incidence, the reflectivity measurement will behave as expected, realizing the DBR's Bragg modes and stopband. As the angle of incidence gets bigger, the whole situation splits into two, between the two polarizations of light.

For all the possible in-plane wavevectors (k-vector), at Transverse Electric (TE) polarization the situation remains the same. Whatever the incidence angle of light, for TE polarization nothing will happen, because there is 0^0 reflection shift to all in-plane wavevectors within the light cone, meaning that it doesn't depend on the angle and remains consistent for all angles.

For the Transverse Magnetic polarization, the circumstances change. As the in-plane wave vector (k-vector) increases to angles beyond the Brewster angle for the top material/air interface, there's a significant change in the amplitude reflectivity coefficient. The Brewster angle is the angle at which light incident on a dielectric surface becomes purely polarized. Beyond the Brewster angle, the change in the amplitude reflectivity coefficient results in the addition of a π (pi) phase shift to the reflected light. This means that the reflected light undergoes a phase inversion compared to the incident light. This phase shift can have a significant impact on interference patterns within the DBR. Due to this phase shift and other factors, the first layer of the DBR (which is typically the high refractive index material) now supports a resonant mode at the center of the stopband inside the light cone. However, this mode is generally very obscure due to the strong imbalance between the DBR's reflectivity and the reflectivity of the first layer-air interface. This imbalance is equalized only at the approach of the critical angle $\approx 90^0$, where the reflectivity of the DBR and the first/layer interface is almost the same. At this point, the resonant mode appears strongly at the center of the stopband. Because this mode realization has similarity with the critical Brewster angle, the half-cavity mode will be called Brewster Cavity mode (BC mode).

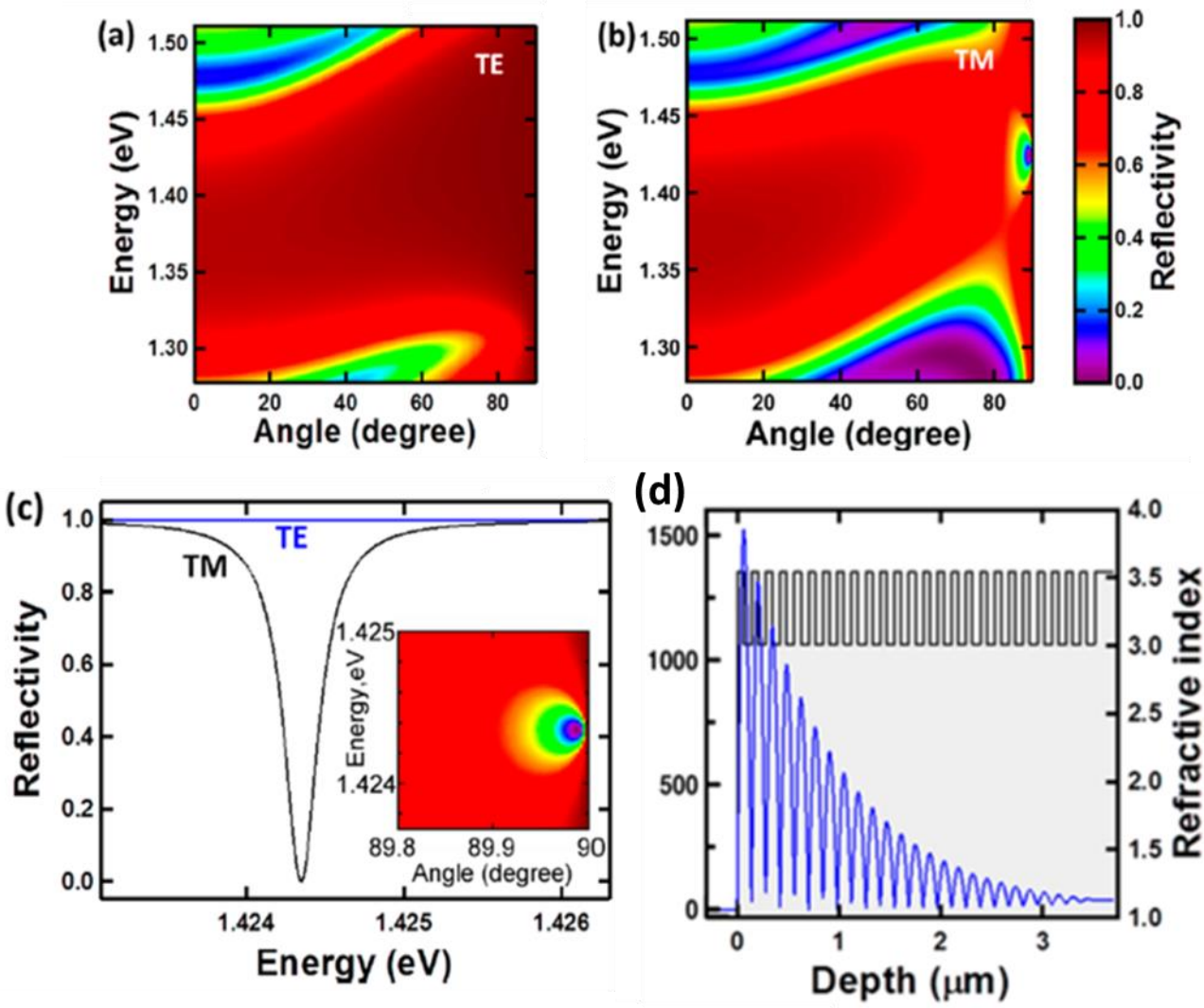

FIGURE 2-8: TM POLARIZATION EVANESCENT MODE REALIZATION

a, b) Transverse Magnetic (TM) vs Transverse Electric (TE) Polarization Reflectivity vs angle of incidence calculation of a ten-pair GaAs/AlAs DBR. For a quarter wave stack DBR, as the angle of incidence approaches the critical angle of almost 90^0, in the TM polarization, the half-cavity evanescent mode is realized. As per the TE polarization, the mode disappears.

c) TE vs TM polarization reflectivity vs Energy. As seen, the TM mode appears only in the realization of the "Brewster angle" and TE polarization reaches peak reflectivity.

d)Field distribution of the system showing a strongly confined mode in the air/first DBR layer interface.

Image source: [75]

The figure above is a theoretical calculation of a 10 pair GaAs/AlAs DBR. The number of pairs was kept small so as to easily depict the BC mode. Noting that for a bigger number of pairs, the BC mode becomes much sharper e.g., for 25 pairs the Q-factor corresponds to ~ 5400 for the TM polarization (TE polarization retains its high reflectivity.) In **Fig. 2-8-d**, the field distribution of the BC mode is presented, illustrating a well-confined standing wave near the interface between air and the Distributed Bragg Reflector (DBR). At the air/DBR interface,

there exists a node, attributed to a π phase shift, and this node repeats at all even DBR interfaces. Conversely, at every odd DBR interface, there is an antinode in the field distribution.

It is important to note that the first layer's thickness can be tuned differently to get similar and better effects. Any top layer that possesses thickness obeying $\frac{p\lambda}{2} + \frac{\lambda}{4}$,with p being an integer, will consequently realize a TM BC mode. In contrast, if the thickness obeys $\frac{p\lambda}{2}$, the BC mode will appear in TE polarization [75]. This thickness tune can prove quite advantageous, considering that the Fresnel coefficients in the TE polarization are larger than the TM polarization ones thus in the TE polarization we will produce higher reflectivity. The Q-Factor of the aforementioned DBR is simulated at 5400, but by introducing a top λ/2 stack, it can exhibit a Q-Factor of 34000. In (**Fig. 2-9**), we present a simulation of this statement. The TM mode has a linewidth of **7 nm.** The TE mode on the other hand has a linewidth of **1 nm**. The Q-factor of the TM mode is 87 and for the TE mode is 629. Conclusively the Q-factor difference is large, making the TE polarization mode a better candidate.

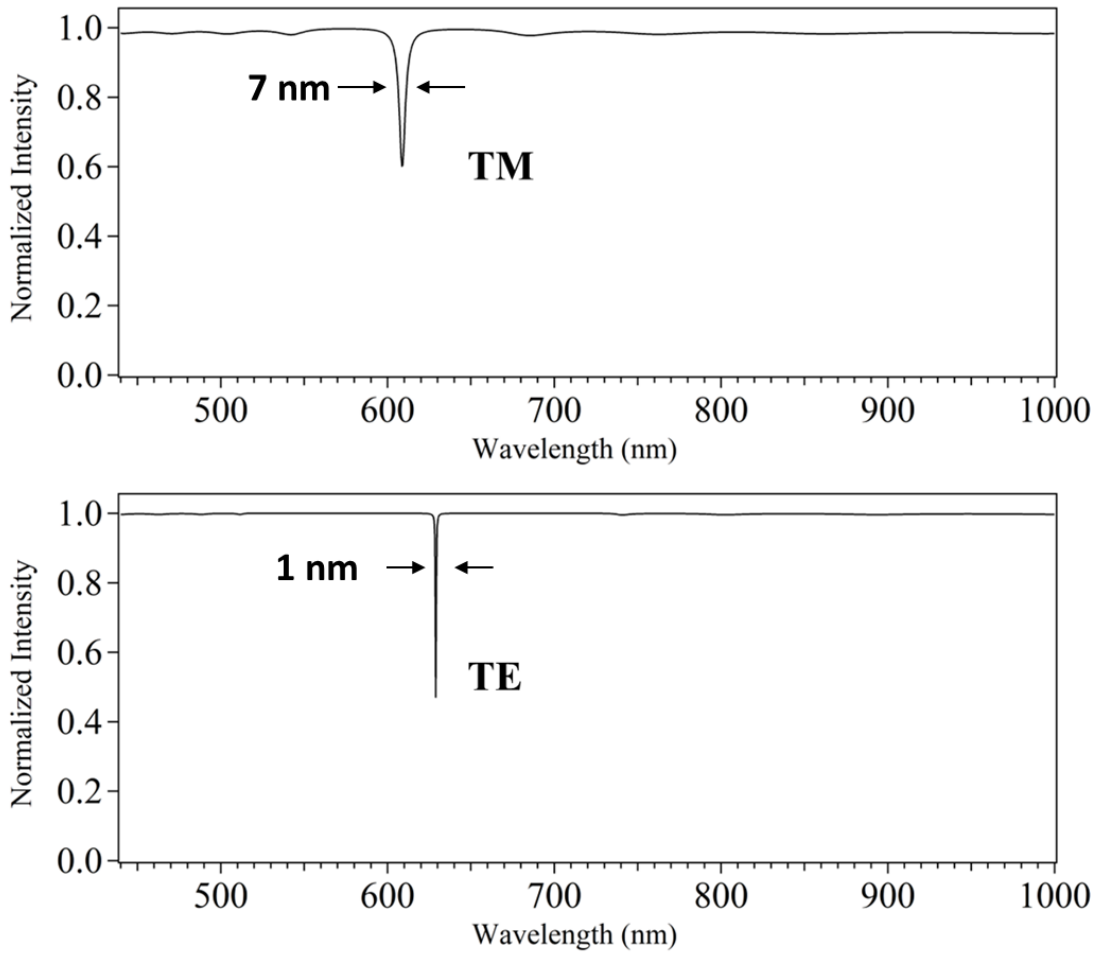

FIGURE 2-9: DBR STRUCTURES REFLECTIVITY MEASUREMENT WITH UPPER LAYER BEING OF QUARTER WAVE THICKNESS (TOP GRAPH) AND HALF WAVE THICKNESS (BOTTOM HALF) AT GRAZING INCIDENCE.

*In these two graphs we present the difference of the resonant mode between a DBR structure with a λ/4 thickness on the top layer and another with λ/2 thickness on the top layer. The structure with the quarter wave on top, produces a resonant mode in the TM polarization and the half wave produces it in the TE polarization. Main difference is the linewidths of the modes. The linewidth of the TE polarization mode is **1 nm** and the TM polarization mode is **7 nm.** The TE mode is much sharper than the TM.*

2.2.4 Brewster Cavity Strong-Coupling Regime

Covering the resonant mode, we move to introduce an actual system that can achieve strong coupling as well as how we can attain and calculate it.

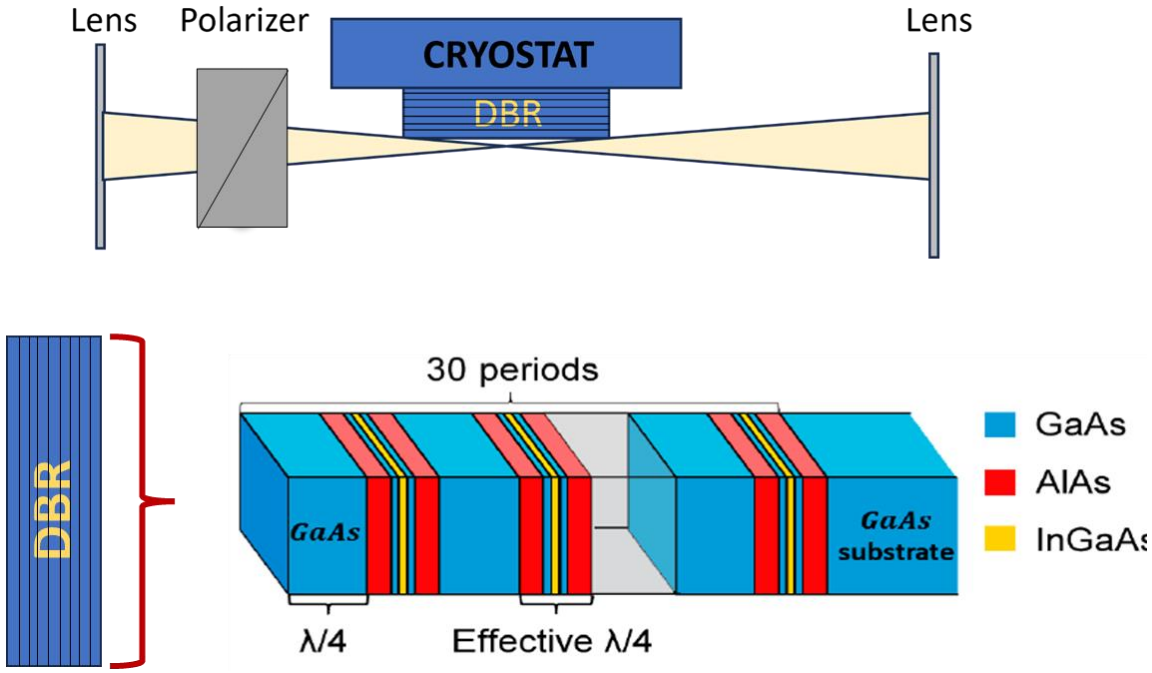

FIGURE 2-10: HIGH-ANGLE SETUP – QW/DBR EFFECTIVE CAVITY

Setup for High-Angle (Brewster), reflectivity towards strong coupling realization. The optical pathway is a straightforward one, having a lens to focus the light at the DBR-QW at grazing incidence. Afterwards, it is polarized and collected/collimated ending into the slits of a spectrometer.
Lower Image Source: [75]

Displayed in **Fig. 2-10**, the optical pathway for this particular method is explained. The exciton medium used is a DBR that has built-in QWs with quarter wave effective thickness so as to produce the Brewster Cavity mode in the TM polarization. The sample is put into a cryostat and cooled until approximately 15K, and a white light source is focused upon it at grazing incidence. Afterwards, the signal is conveyed into a TM polarizer and then collected into a spectrometer. The results are shown below.

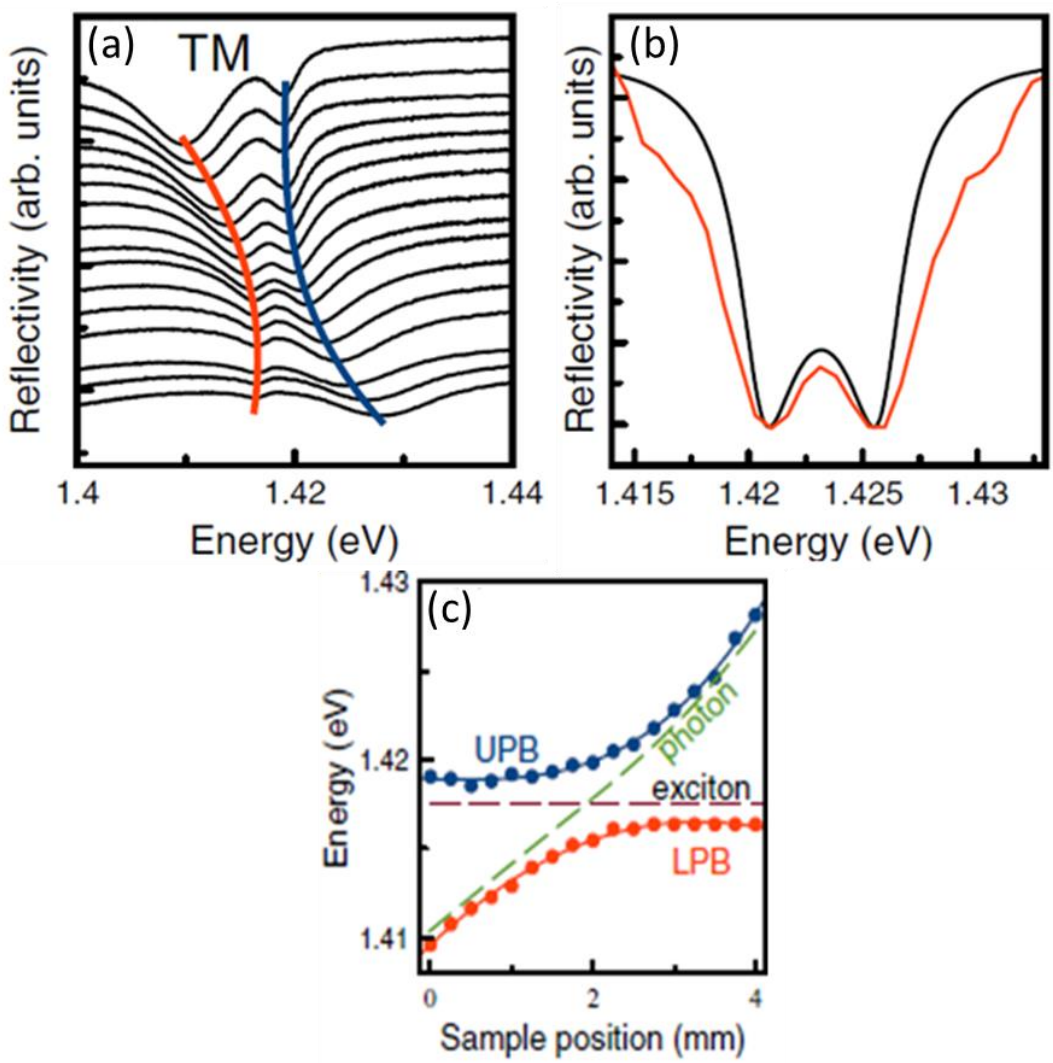

FIGURE 2-11: REFLECTIVITY MEASUREMENTS REAVEALING STRONG COUPLING REGIME

Brewster-Cavity in the strong coupling regime. (a) displays the experimental reflectivity vs detuning measurement, which reveals clear anticrossing. (b), (c) are theoretical calculations designed to fit and ultimately prove that the system is in fact in the strong coupling regime. From (b), which shows both experiment and simulation, the Ravi splitting is calculated at Ω = 5 meV. Image source: [75]

In those high-angles, light becomes highly directionally dependent. Reflectivity measurements vs detuning as displayed in **Fig. 2-11 (a)**, clearly prove that the system is in the strong coupling regime revealing clear anticrossing. Using a 2D theoretical model, it can be calculated with agreement to the experiment that the mode and exciton evidently anticross, revealing the Upper Polariton Branch and the Lower Polariton Branch. The reflectivity peaks are displayed vs sample position and with the help of simulation, the Rabi splitting is calculated at **Ω = 5 meV**.

2.3 Motivation

Subsequently, the drive of this experimental work is to achieve thorough optimization of the perovskite material. This ultimately means that we will test and adjust chemical formulas so as to possess a complete high quality crystal formula well – behaved both in structural and in optical properties. As this is completed, we shall move onto the two projects that were explored. The first project searches the possibility of introducing the perovskite material onto a Half-Cavity DBR and thus exploring strong coupling regime in such a system (**Fig. 2-12(a)**). The second project was a joint work done in collaboration with a colleague and it was to introduce this optimized material into a standard DBR microcavity so as to again explore strong coupling regime (**Fig. 2-12 (b)**).

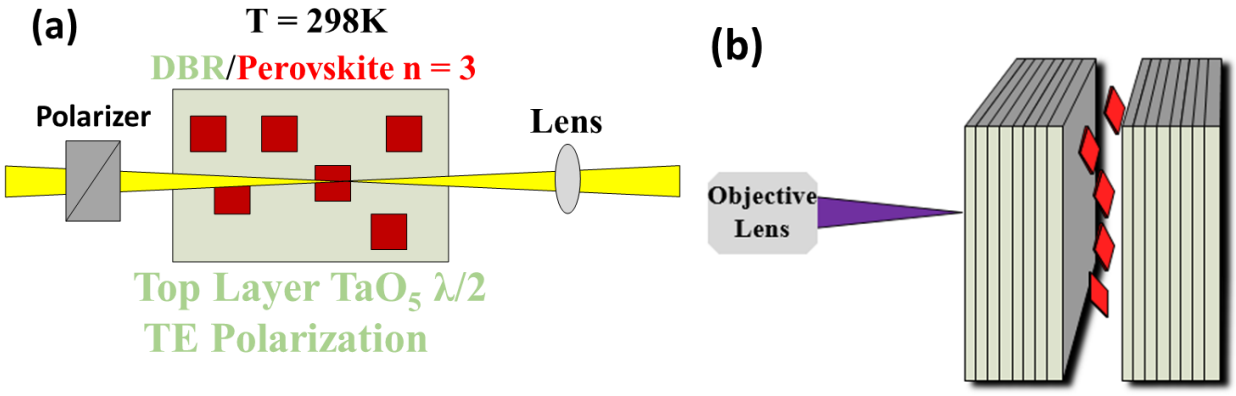

FIGURE 2-12: SKETCH REPRESENTATION OF THE TWO PROJECTS THAT WILL TAKE PLACE IN THIS THESIS

(a) *Image presenting the first experimental system for an optimized perovskite crystal introduced onto a DBR Half-Cavity in order to realize strong coupling regime.*

(b) Image presenting the second system which is a standard DBR microcavity with the perovskite material introduced between the two mirrors again for polariton application.

3 Experimental Results

The experimental part of this thesis is divided into 3 chapters. The first chapter is focused in the perovskite crystal and how to optimize its fabrication as well as optical behavior. The second chapter is one of the two projects that were underwent. Specifically, a particular setup was used to attempt strong coupling regime with a perovskite crystal deposited upon a custom grown DBR creating a "half cavity", in a certain light angle of incidence, particularly $\approx 89^0$. The way this procedure works will be further analyzed in its respective chapter. The third chapter, is focused in creating a standard microcavity with the perovskite crystal being the active medium so as to again realize strong coupling.

3.1 Experimental Setups

In this sub-chapter, the setups created for all the experiments and measurements done are shown in the figures below. Divided as:

1. Photoluminescence/Reflectivity/Dispersion 0 degrees Setup. (**Fig. 3-1**)
2. Photoluminescence/Reflectivity/Imaging 60 degrees Setup. (**Fig. 3-2**)
3. Reflectivity ~ 90 Degrees Setup. (**Fig. 3-3**)

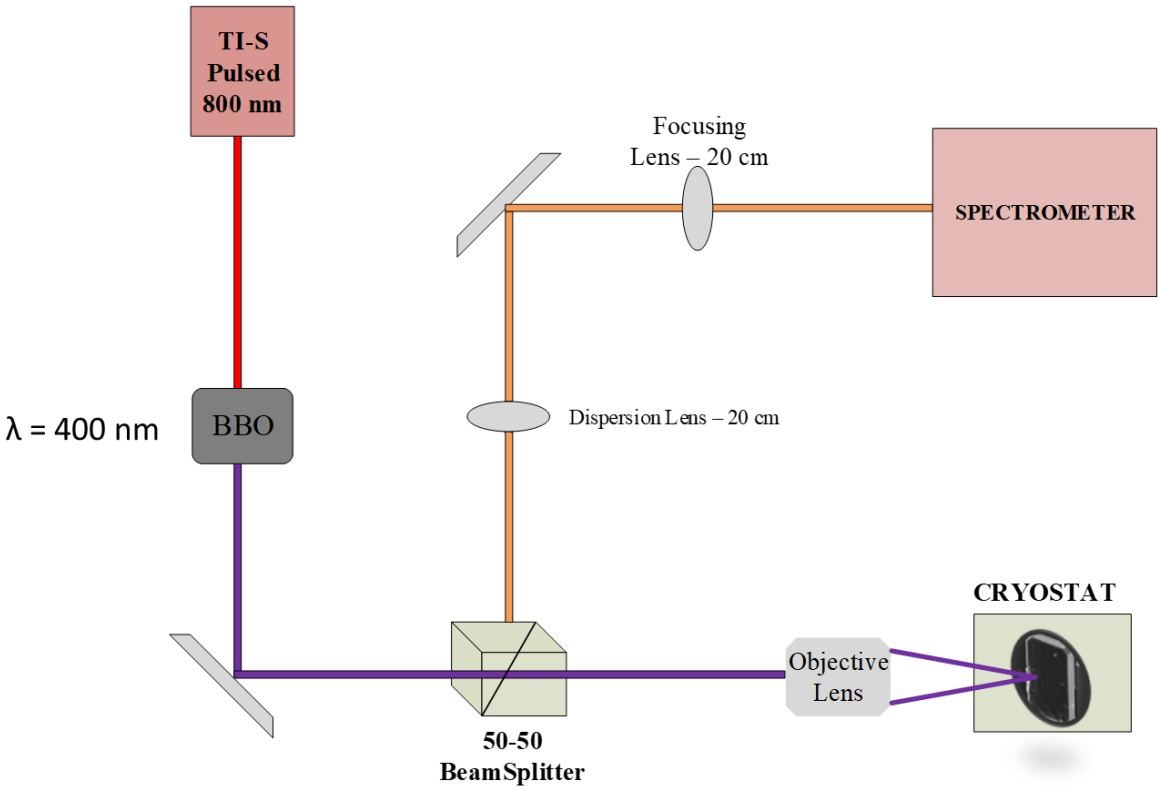

FIGURE 3-1:*NORMAL INCIDENCE OPTICAL SETUP*

Photoluminescence-Reflectivity-Dispersion setup. Starting from a Ti:S 800nm Pulsed Laser, we change the wavelength to 400 nm with a BBO (Birefringent material that is used for frequency doubling, phase matching etc.). After this, the laser passes through a Beam splitter and through an objective lens that lets the laser be introduced onto the substrate at a zero-degree angle with a spot size of 3 micrometers. The signal then gets through the same objective and into focused into the spectrometer.

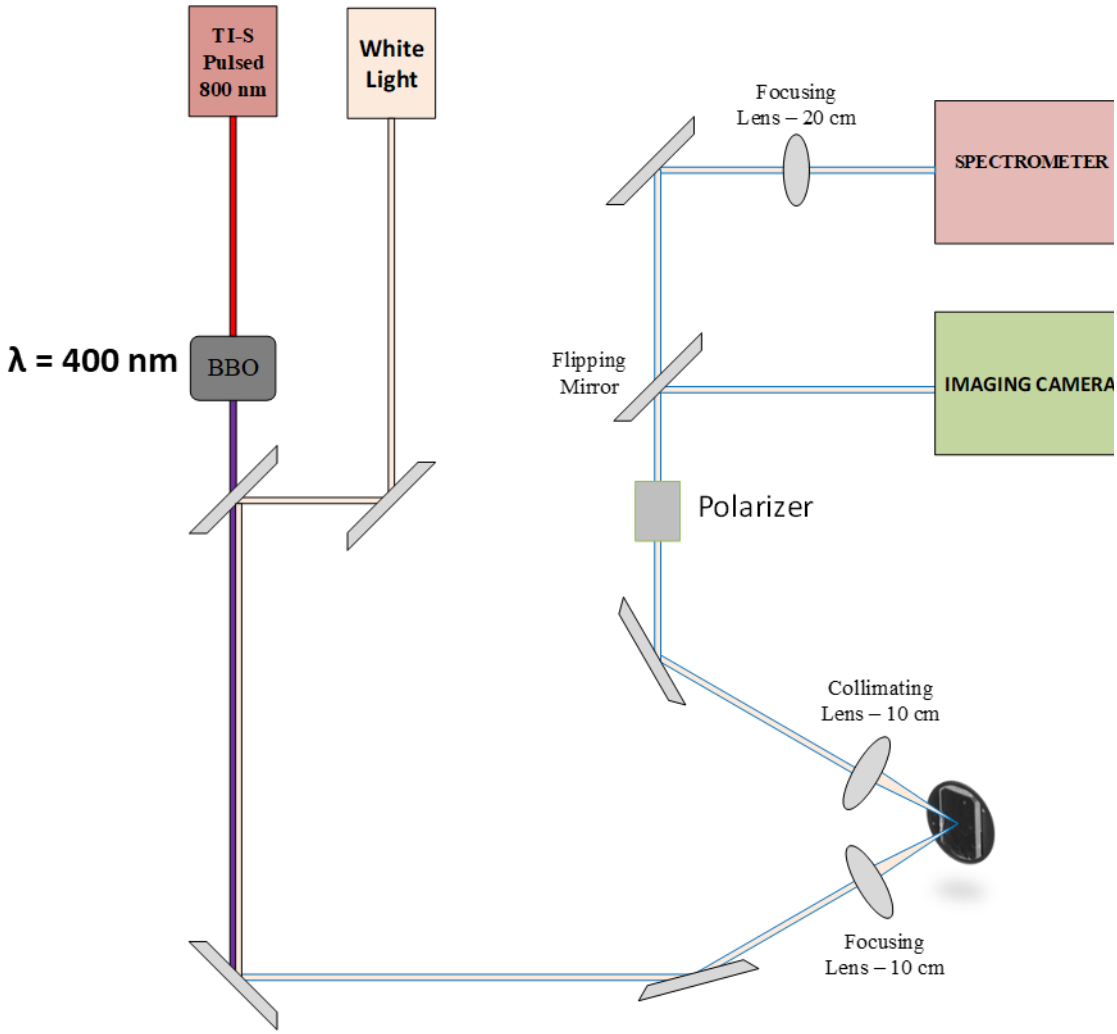

FIGURE 3-2: *60⁰ OPTICAL SETUP*

Photoluminescence-reflectivity-imaging setup. Starting with a Ti:S 800nm laser and a White light Tungsten lamp, we align the two separate light sources into the same optical pathway. The light then indices at a 60-degree angle and gets focused onto the substrate through an achromatic lens of focal length 10 mm. The signal then gets collimated by another 10 mm lens and either gets focused into an imaging camera or into the spectrometer depending on the measurement nature.

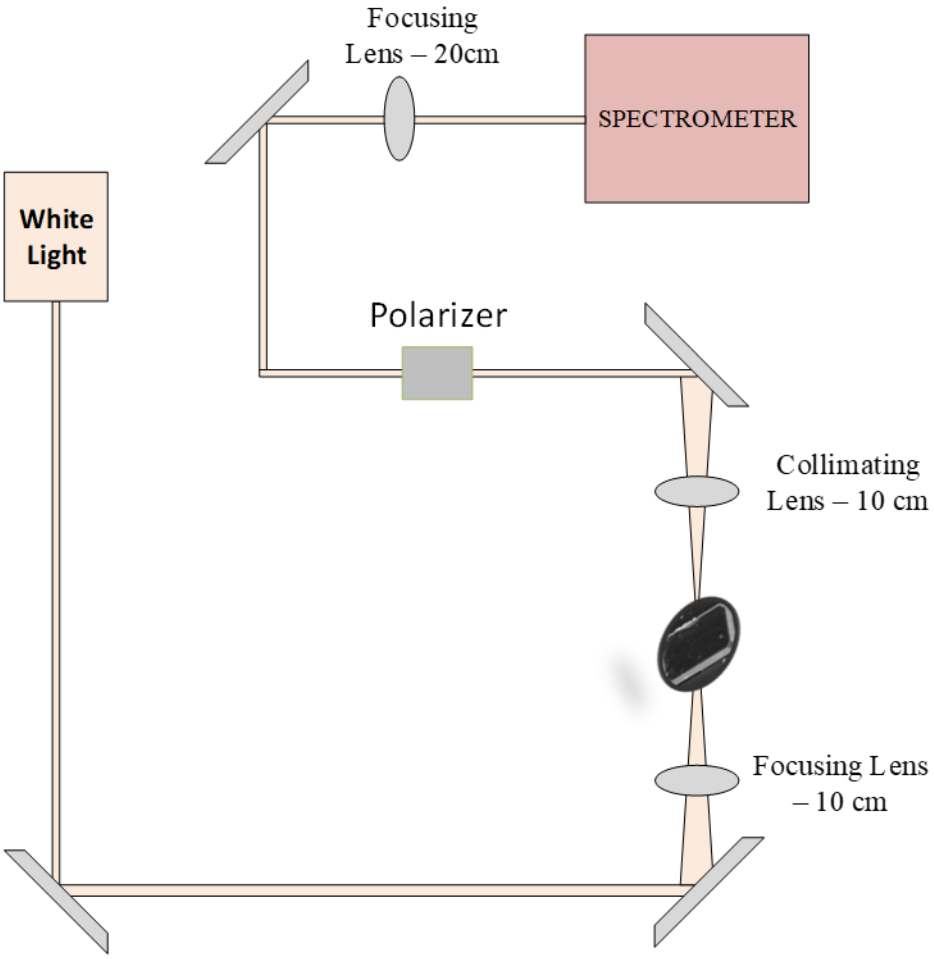

FIGURE 3-3:*GRAZING INCIDENCE OPTICAL SETUP*

High-Angle (Approximately 90 Degrees) Reflectivity Setup. Starting from a White light source, we illuminate the substrate at an angle of approximately 90 Degrees which is focused with a 10 mm Lens and also collimated by another one. The signal afterwards, can pass through a polarizer and focused into the spectrometer.

3.2 Perovskite crystal optimization

In this chapter, the main focus was to optimize the material which will be used as a medium for strong coupling realization. There are many types of perovskite crystals with various ways of fabrication, growth, structure and optical properties. This particular work contains one particular structure of perovskite called Ruddlesen – Popper perovskite. Particularly, this experiment used Butylammonium Methylammonium Lead Iodide ($(HA)_2(MA)_2Pb_3Br_{10}$), specifically a tri-layer (n=3) which is a Halide Perovskite as it will be mentioned again on the synthesis part. This structure is not as extensively analyzed as its n=1 counterpart.

3.3 Liquid Exfoliation Method

The procedure of liquid exfoliation involves the separation of layers within a crystal using a suitable solvent and ultrasonic agitation. To achieve successful exfoliation, the crystal material must possess weak out-of-plane bonds. The process begins by dispersing the material in a solvent, forming a suspension. Ultrasonic agitation is then applied, typically using high-frequency sound waves, which create pressure variations in the solvent. These pressure fluctuations induce mechanical forces that act on the crystal, promoting the delamination of layers along the weakly bonded planes. As a result, the layers are separated and suspended within the solvent [80,81].

The effectiveness of liquid exfoliation depends on several factors, including the properties of the solvent, the concentration of the material, and the duration and intensity of the ultrasonic treatment. The choice of solvent is crucial as it should provide sufficient solvation for the crystal material and minimize interlayer interactions. Additionally, the ultrasonic agitation should be carefully controlled to avoid excessive heating or damage to the material.

Liquid exfoliation has been widely employed for various 2D materials, including graphene and transition metal dichalcogenides, as well as emerging materials such as perovskites. The resulting exfoliated flakes or nanosheets exhibit a significantly increased surface area, facilitating their utilization in various applications such as electronics, energy storage, and catalysis. The material is placed in a suitable solvent, and through ultrasonic agitation, the layers of the crystals are separated [82,83]. For this process to be successful, the active material used must have weak out-of-plane bonds. With exfoliation, it is possible to achieve a very large surface area on the order of up to 1000 m^2/g. This method is widely used for other 2D materials such as graphene. Specifically, perovskite materials have strong in-plane hydrogen bonds and weak out-of-plane Van der Waals bonds. Due to this property, the crystals can be exfoliated, resulting in the formation of multiple nanometer-thick layers.

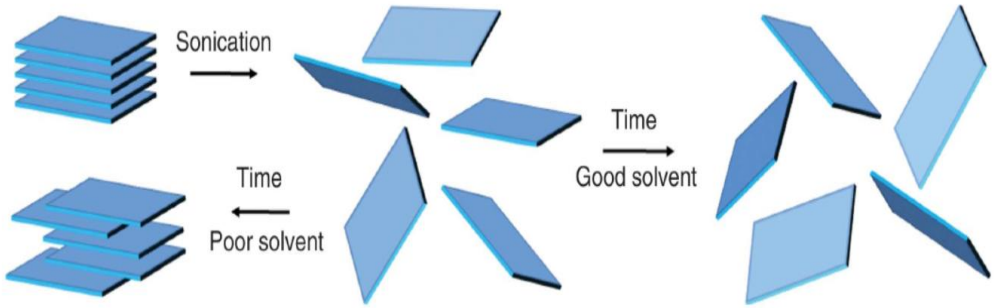

FIGURE 3-4:*LIQUID EXFOLIATION PROCESS*

Liquid exfoliation Procedure. Initially, a vial with a layered material and solvent inside is introduced into a sonicator. Afterwards, through the sonicator's waves, the material's weak out of plane bonds start breaking which results in realizing multiple layers with the passage of time.
Image source: [82]

3.3.1 Crystal formation

Starting with the first method of optimization, liquid exfoliation. After the crystal was formed, it was put in a Polystyrene/Toluene solution for humidity protection and into a sonicator bath for exfoliation, The whole procedure is shown in the figure below. Following that, a sample was collected from the vial for spin coating onto a substrate (mostly silicon for testing and after optimization we could proceed to a DBR).

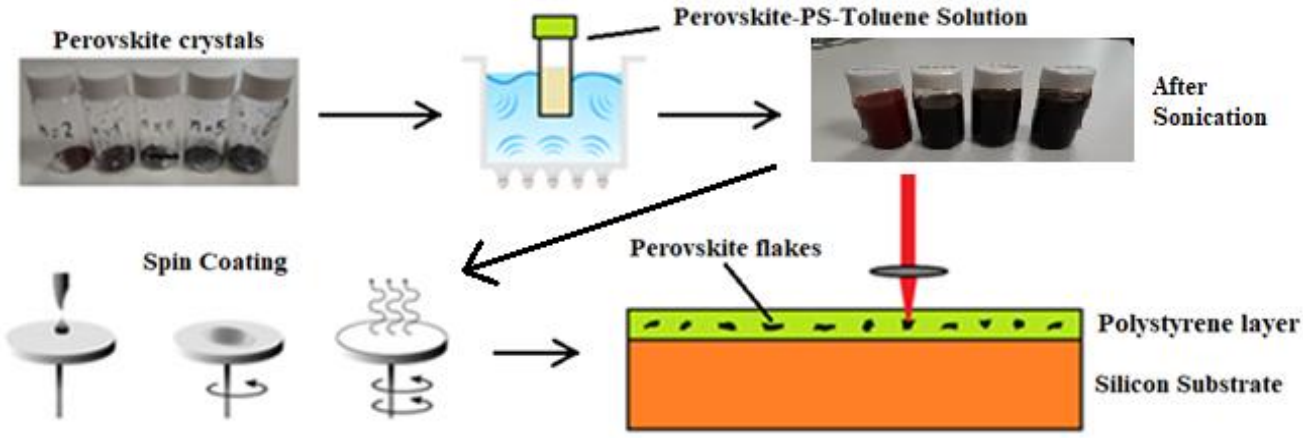

FIGURE 3-5: ***LIQUID EXFOLIATION PEROVSKITE FABRICATION***

Whole Liquid Exfoliation Procedure. Starting from vials containing the perovskite crystals, we then add solvent mixed with PS. This step provides us with a final solution of Perovskite-PS-Toluene. The reason for the solvent is for optimal sonication conditions and the reason for PS is for the final result to be into a polymer matrix for better spin coating results. After sonication, the solution is then spin coated onto the desired substrate (Silicon, glass or DBR) and let to dry in ambient conditions. Afterwards, the sample is ready to be measured.

Generally, this procedure was used due to its initially promising possibilities of adjusting the thickness of the perovskite crystals by controlling it with spin coating. It is important for the perovskite crystal to have controlled thickness because it will be put into cavities and cavities -either half-cavity or standard cavity- require small thickness for less losses.

3.3.2 Optical and Structural Characterization

The characterization mainly done was Photoluminescence measurements. As per **Fig. 3-6,3-7**, the sample was measured using a Ti:S pulsed laser –Mira Coherent- that produces 800 nm wavelength but as it passes through a BBO crystal, the wavelength that ultimately excites the material is 400nm. Initially, the results of course were not optimal as it is shown in **Fig. 3-6**.

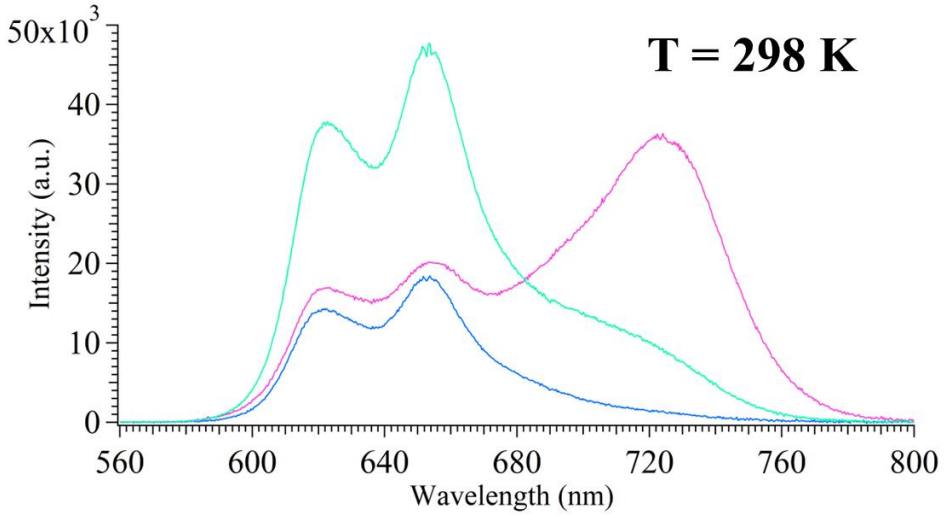

FIGURE 3-6*: INITIAL LIQUID EXFOLIATION PL MEASUREMENTS*

First PL measurements after liquid exfoliation procedure. There appear multiple peaks which are at: 620 nm (n = 3), 655 nm (n =4) and 720 nm (Edge Effect). Multiple peaks indicate that the crystal structure contains multiple values of "n".

The first tries show that the perovskite's exciton emission is not pure. The PL shows multiple peaks, varying from 620nm –n=3- to 650nm – n=4 – as well as a peak at 720 nm known as "edge effect". The edge effect peak generally refers to cracks at the edges of the crystal and all-around bad uniformity, realizing that 720 nm peak.

After controlling as capable as possible the spin coating speed/time parameters as well as the chemical formula's composition, the results were more promising from the perspective of photoluminescence exciton emission but the structure of the crystal was still far from standard results. The figures below show the final PL results as well as microscope and SEM measurements displaying the structure of the crystal.

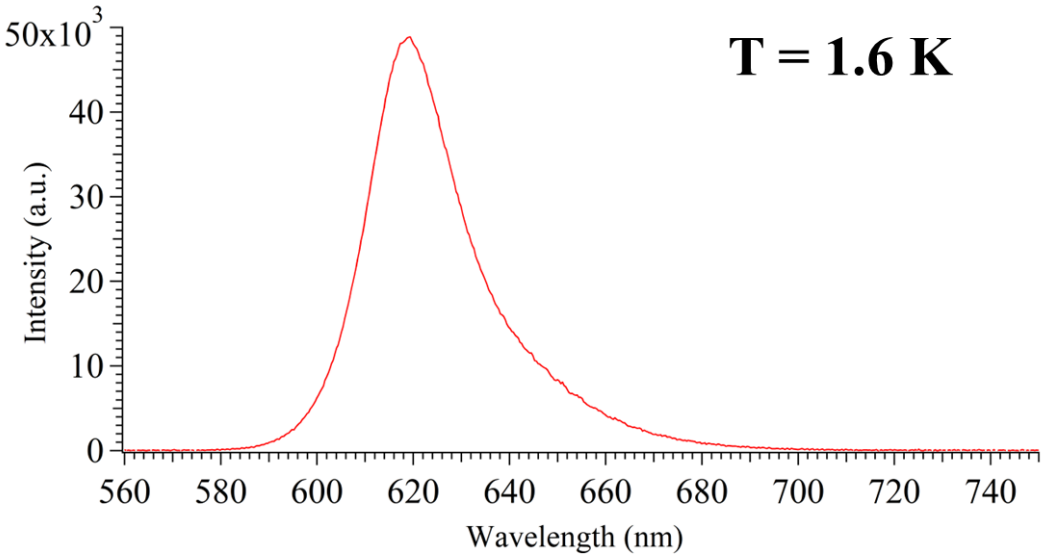

FIGURE 3-7: *FINAL LIQUID EXFOLIATION PL MEASUREMENTS*

Final PL measurement after procedure optimization. The measurement above, although it satisfies optical purity, is a unique measurement in the way that in the whole surface of the sample, this particular purity came from only one spot. Conclusively, even if the PL is satisfactory, the bad uniformity of the substrate brings a very large constraint.

As it is exhibited in the figure above, the optical behavior of the crystal was managed to have the desired excitonic emission. We can clearly see only one peak at 620 nm -n=3- with linewidth of 25 nm. Conclusively, from the photoluminescence, we see that the crystal has the correct exciton emission. The bigger issue with this method comes from the crystal structures.

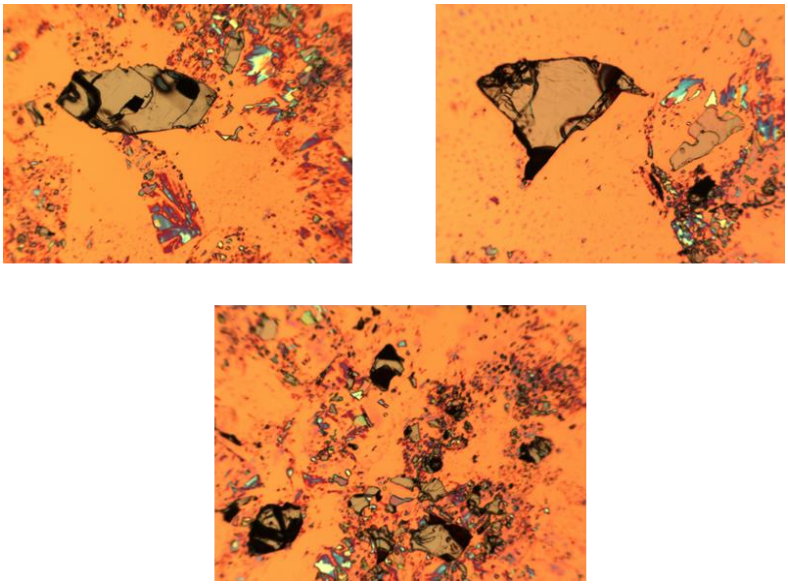

FIGURE 3-8: *MICROSCOPE PICTURES OF LIQUID EXFOLIATED CRYSTALS*

Microscope n =3 Perovskite crystals after the liquid exfoliation procedure. As displayed, the crystals have seemingly completely random shapes and sizes as well as cracks. This suggests that this particular procedure for this perovskite system proves inadequate.

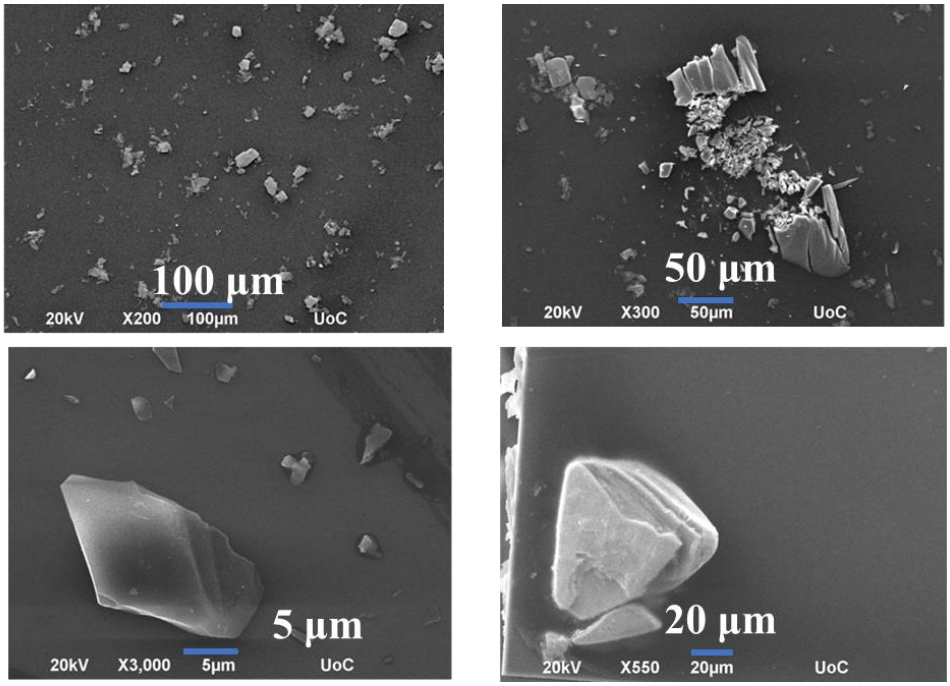

FIGURE 3-9*: SEM IMAGES OF LIQUID EXFOLIATED CRYSTALS*

SEM pictures of n =3 Perovskite crystals after the liquid exfoliation procedure. As it was partially shown with the Microscope pictures, the same basic principle applied with the SEM pictures. The crystals are very scarce and randomly shaped onto the substrate, not providing uniformity. As it was said above, this procedure does not satisfy.

From the microscope and SEM measurements, we take the following conclusions. The crystal does not have the correct shape (usually a rectangle type of shape) and also has large thicknesses of 15 μm. We also observe many crystals that were seriously damaged with visible cracks as well as many samples having very little number of crystals. As such, even if the sample provides somewhat better photoluminescence measurements, the number of the crystals onto a substrate is considerably low.

3.3.3 Conclusions

Summarizing the whole procedure, the perovskite crystals were too damaged in this method and they didn't have the correct thickness and shape overall. Best thickness achieved were close to 10 μm and the shape of the crystals was not achieved. It is essential for the crystals to have small thicknesses because they are being optimized so as to be incorporated into cavities. In addition, this method had too many parameters to control, such as spin coating time and/or acceleration as well as the need to find the correct amount of Polystyrene/toluene solution for the sample to be protected. All of the above couldn't be sufficiently optimized using this method. We needed a better method to attain a better crystal structure.

3.4 Solution Method

Following up, the second method that was implemented for the crystal optimization is called the solution method. In this chapter, we show the whole journey, from synthesis to fabrication to characterization and optimization of the perovskite crystals. In particular, our perovskite crystals obey the structure of 2D Halide Perovskites with the **Halide** component here being: **Iodide (I)**

3.4.1 Synthesis

The whole procedure of the crystal synthesis is as follows:

Materials: Lead oxide (PbO 99.9%), hydroiodic acid (HI, 57% w/w in H_2O), hypophosphorous acid (H_3PO_2, 50 w/w in H_2O) and butylamine (BA) (>99.5%) were purchased from Merck and used as received. Methylammonium chloride (MACl from 37% HCl and 99% Methylamine) was synthesized in the crystal chemistry lab of University of Crete.

Synthesis of **$(BA)_2(MA)_2Pb_3I_{10}$ (n=3).**

$PbO_{(s)}$ (39.51mg, 1.77mmol) and methylamine (104μL, 1.2mmol were added in a 20mL scintillation vial and dissolved in a mixture of $HI_{(aq)}$ (2.6mL) and $H_3PO_{2(aq)}$ (0.26 mL), under continuous stirring at 125°C. When the solution became clear, the butylamine (75μL, 0.76mmol) was added. After 10 minutes, stirring was discontinued and the reaction was allowed to cool naturally to ambient temperature. After 10 minutes, dark red, plate-like crystals precipitated at the bottom of the vial. The resultant precipitate was isolated via suction filtration. Yield: (~51%).

The final vial, contains perovskite crystal solution with Hydrogen Iodide. In order for it to be used, it first needs to be brought to a correct temperature of approximately 80-90^{0}C and with a pipette, dropped onto the substrate. As the system cools, perovskite crystals can be seen growing live. As a general consequence of this particular method, we can easily tune the initial amounts of reactants to achieve the desired n value.

The whole formula was synthesized and tuned by our colleagues in the crystal lab dpt. Run by **Prof. Stoumpos**, which are: **Marios Triantafylloy, Apostolos Pantousas, Eleni C. Macropulos**.

In addition to the well-made chemical formula, a fabrication procedure was also devised so as to produce the optimal sample uniformity and to avoid crystal damage. In the figure below, is the whole setup that was used. When the materials are brought to a temperature of 70^0, a predetermined amount of it is then transferred onto a substrate with a pipette. The substrate sits upon a custom-made aluminum base. Immediately afterwards, the substrate is covered with a superstrate (generally the same type of the substrate), and from the top pushed by an also custom-made aluminum cap. The whole structure is uniformly pressured by two magnets from the bottom and top. This magnet/DBR setup (**Fig. 3-10**) was a joint idea by myself and Emmanouil Mavrotsoupakis who was a collaborator in the laboratory.

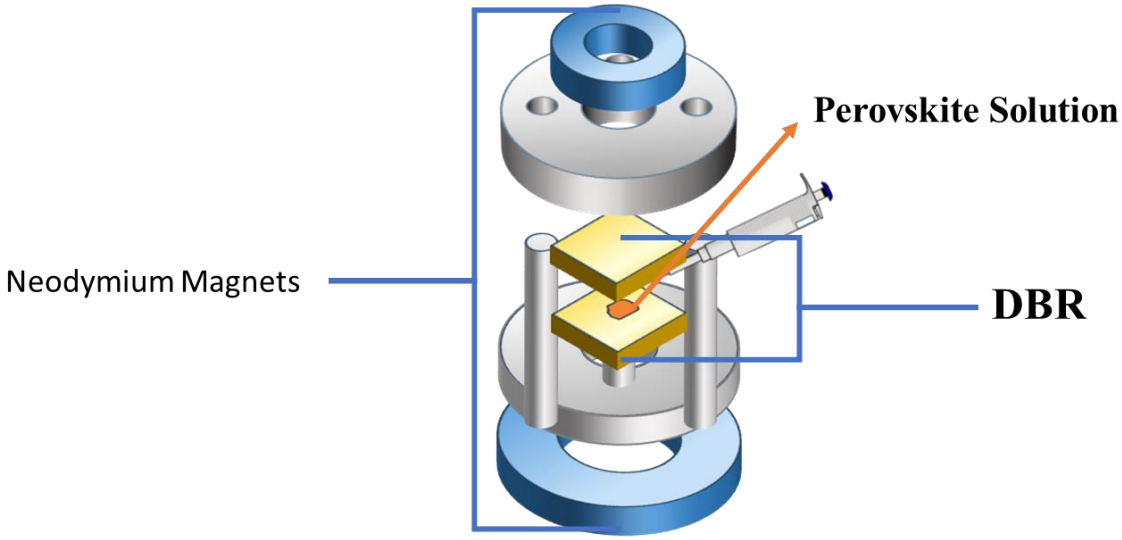

FIGURE 3-10: SOLUTION METHOD FABRICATION SETUP

Fabrication procedure of the method. After the perovskite solution is heated to 80-90^{0}C, it is immediately dropped onto the substrate and then into the aluminum setup which is pushed by a uniform magnetic force. This results to a very uniform sample.

3.4.2 Structural Characterization

At first, various "n" crystals were produced so as to explore the structure tunability of the formula. Particularly, there were crystals manufactured successfully from n=1 to n=4. Initially, microscope/SEM and XRD measurements for the aforementioned n values are shown below. Noting that the XRD measurements were executed by Eleni C. Macropulos which was one of the crucial members that also took part in the synthesis of the perovskite solution formula.

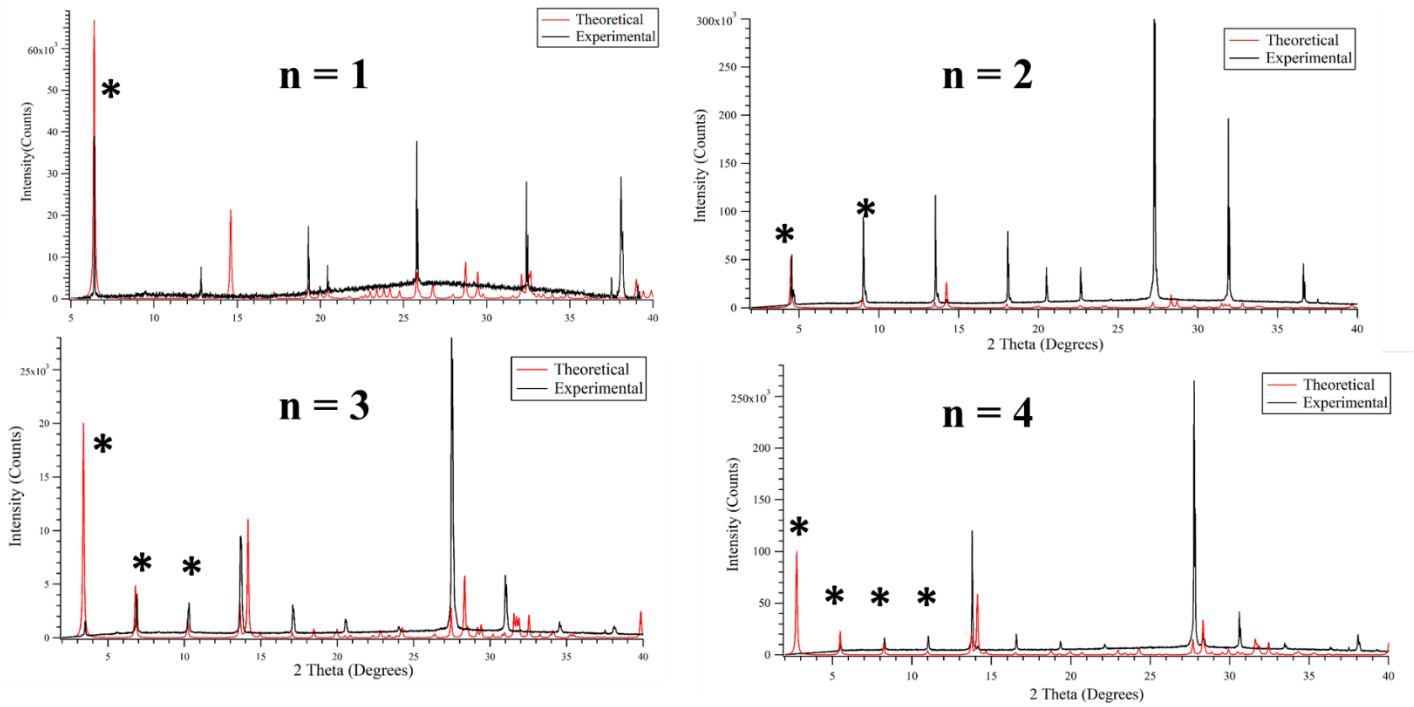

FIGURE 3-11: XRD MEASUREMENTS FOR PEROVSKITE CRYSTALS N = 1-4

Theoretical XRDs (Red) vs Experimental XRDs (Black) for n=1,2,3,4. The crystal's structural purity is proved by the data very satisfactory. This is indicated by the correct multiplicity of the peaks below and around 15^0-theoretical correspondence-, that are accurate indicators of a layered perovskite structure.

Following up for this statement, in **Fig. 3-11**, the XRD measurements that were done to n = 1-4 suggest high crystal structural quality of the crystal compared with its theoretical counterpart. The crystal's "n" value is extracted through observing the plot's peaks at around 0 to 15 degrees [27]. In this range, depending on the "n" value, we expect the same amount of low angle of peaks. For example, the n =1 XRD measurement exhibits only one peak in the aforementioned range and the n = 3 depicts three peaks. Important note, the measurements were done on a partially wet crystal incorporated onto a SiO_2 substrate. This fact directly affects the large intensities of certain peaks in the measurements and because of this, it proves difficult for certain peaks to appear because of the high intensity of those that are in the spectra. Moreover, for the XRD measurement of the perovskite crystal n =4, the first peak of the quadruple multiplicity is not visible experimentally. This problem arises due to the difficulty of the XRD machine to not properly recognize peaks in very small angles probably because of alignment issues. Continuing with the crystal's images below.

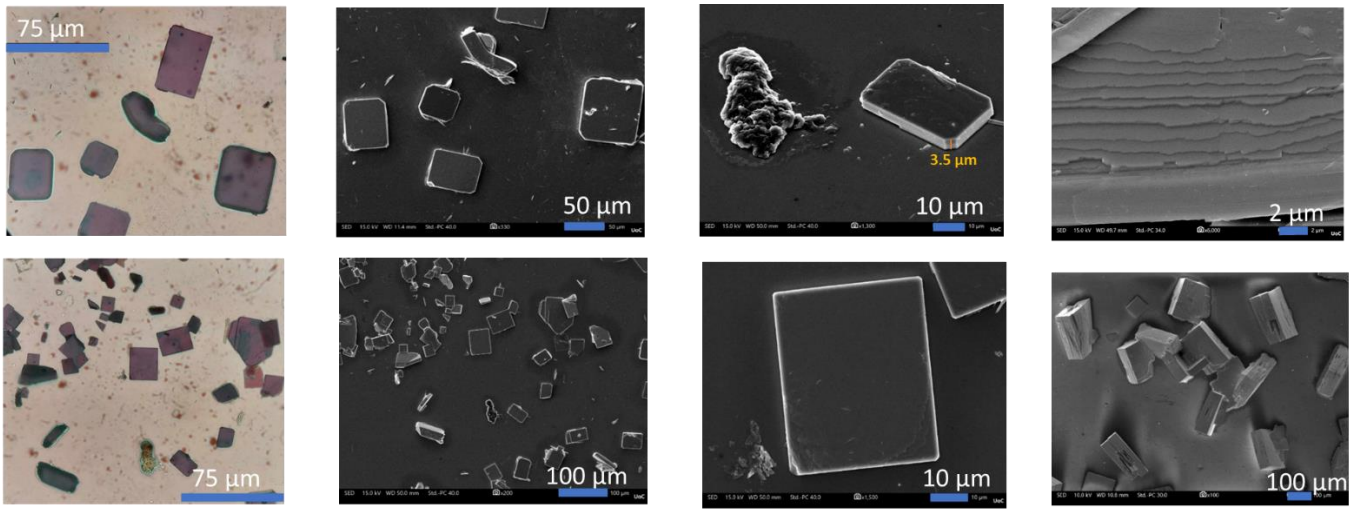

FIGURE 3-12: MICROSCOPE AND SEM IMAGES FOR SOLUTION METHOD N = 3 PEROVSKITE CRYSTAL
Microscope and SEM measurements of n=3 Perovskite crystal. It is clearly exhibited, that the crystal is obviously layered and that the sample has an overall high crystal distribution as well as many of the individual crystals are proven to be of high quality through their orthogonal/tetragonal structure.

The pictures of the crystals are convincing enough to state that the crystal's overall structural integrity is of good quality. Most crystals individually, possess a nice orthogonal structure and also have clean and clear surfaces. The material, is clearly layered with the layers being apparent in the upper right image. Lastly, crystal vs sample surface distribution is displayed to be very high, providing with a sample that can be mapped in a large area and has good quality material. Important note, even if the crystals mostly display good quality, there are many cases indicating the unfortunate randomness of angle development on the substrates and in addition to this disadvantage, the crystals have a relatively high thickness -resulting from the initial chemical formula's composition to thickness ratio- which needs more adjustments for it to be incorporated into cavities. This, as it will be analyzed later in the next chapter- might prove a difficult obstacle for certain measurements and projects.

3.4.3 Optical Characterization

Leaving the structural characterization, we proceed to assess and analyze its optical emission with measurements such as PL/Reflectivity/Power and Temperature dependence. Below there are various optical measurements of the perovskite crystal explaining its quality as well as the road to its accurate development.

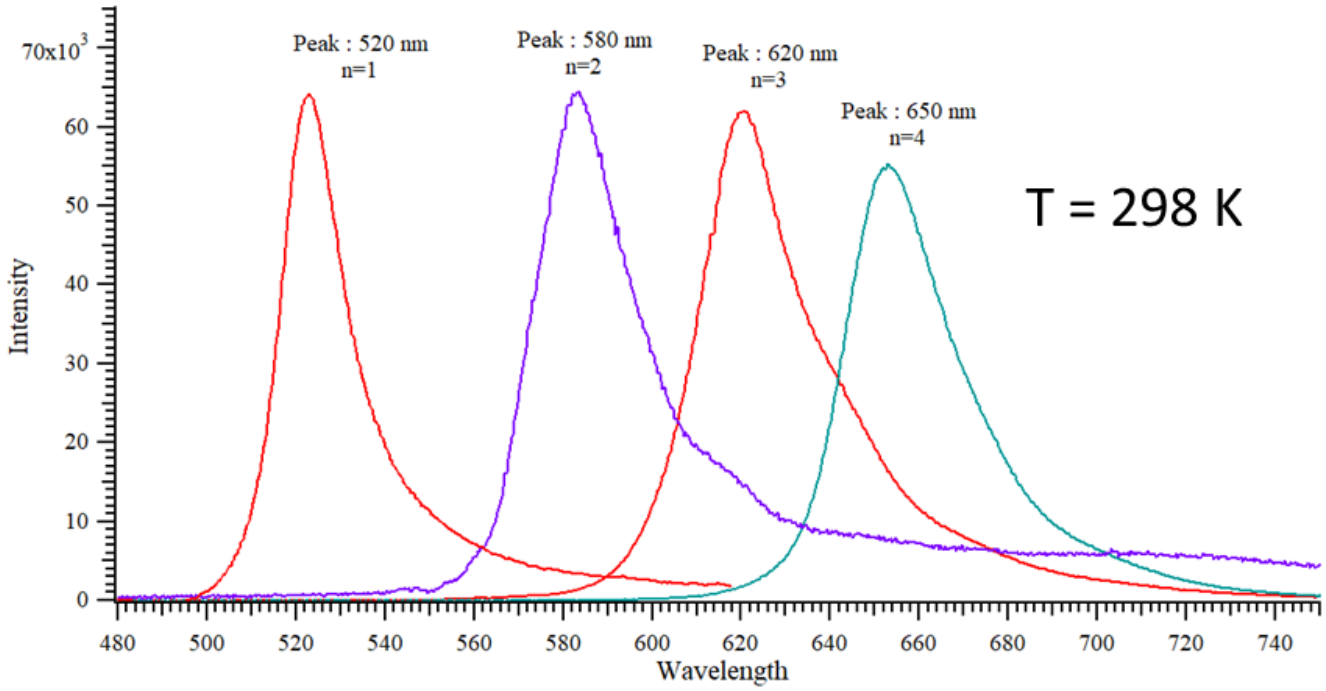

FIGURE 3-13: SOLUTION METHODPHOTOLUMINESCENCE MEASUREMENTS FOR N = 1-4

Photoluminescence Measurements exhibiting perovskite crystals that were fabricated. As it is theoretically suggested, the difference of the n value is realized in difference of the exciton emission due to the change of the thickness between the organic barriers.

In **Fig. 3-13**, PL measurements are seen for 4 different values of n. For all of them, the exciton emission peak is exactly where it was expected and also no other peaks are visible, suggesting that the majority of the sample's crystals are correctly structured and pure, producing stable room temperature excitonic emission.

The wet solution method provides a chemical synthesis formula that exacts promising and consistent results. As aforementioned, the n=1 perovskite crystal is extensively researched and studied and thus, this thesis is almost completely focused in the less known area of the perovskite crystal formula that provides the n = 3 structure. Going forward, fabrication and optimization of the perovskite crystal, includes only the n =3 variation. The next two chapters will focus onto the structural and optical behavior of this crystal showing a variety of measurements required so as for the material to be introduced into cavities for polaritonic applications.

After the chemical team tinkered with the formula's components and amounts, we reached the final and fully optimized result shown in the figures below. From multiple measurements, we can finally see that the crystal resulted well. PL and Reflectivity measurements (**Fig. 3-14, 3-15**) display perfect n=3 excitonic emission at room temperature and at low temperature and it also exhibits almost perfect optical purity -without any other "n" visible- as well as the expected blue shift originating from the structural change of the phase transition. Generally, the formula is expected and tuned for one value of "n", but it is possible to end up with a crystal that possesses multiple "n" values. This is because the amount of the chemical components needs to be extremely accurate or else, we can end up with multiple crystal "n" values in the same solution.

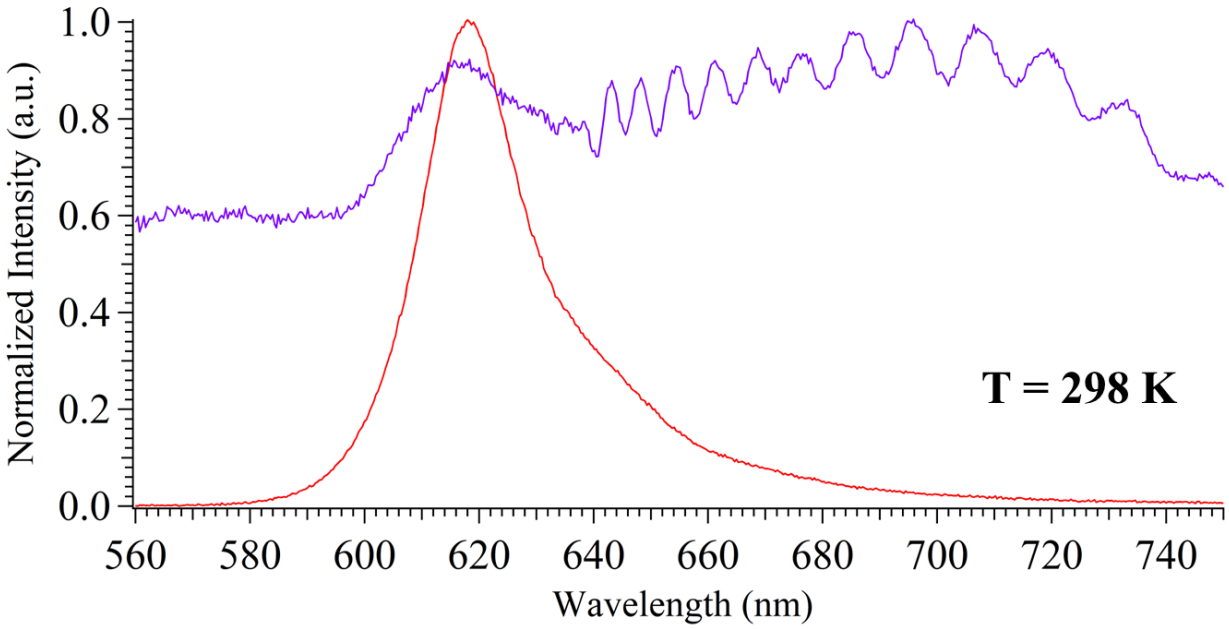

FIGURE 3-14*: ROOM TEMPERATURE PL AND REFLECTIVITY MEASUREMENTS OF OPTIMIZED CRYSTAL*

Perovskite crystal PL/Reflectivity measurements after completing fine tuning of the chemical formula and procedure. As observed, the excitonic peak in the PL is very pure. The reflectivity is somewhat more difficult to observe in room temperature due to the crystal scattering light. The "oscillations" that are exhibited, are assumed to be created because of light bouncing between the crystal's many layers -due to its relatively high thickness-.

Exhibited in **Fig. 3-14**, we display the PL and reflectivity measurements of the perovskite crystal at ambient temperature. The PL exciton peak depicted, clearly proves that the perovskite crystal is optically pure with emission at 620 nm and linewidth of . The excitonic emission in the reflectivity measurement is qualitatively found through the edge of the curve and is generally expected to be slightly blueshifted in the range of **10-15 nm** [27]. This is somewhat obscure in the room temperature measurements as the reflectivity is broadened but it becomes very clear in low temperature measurements (**Fig. 3-15**). In addition, the perovskite scatters light somewhat significantly, making reflectivity measurements more difficult. The "oscillations" that are observed after the exciton emission in the reflectivity measurement are attributed to the thickness of the crystal, meaning that the light bounces between the crystal's layers and produces this behavior. Note that this does not necessarily happen because the crystal does not develop fully flatly onto the substrate surface as seen from the SEM pictures.

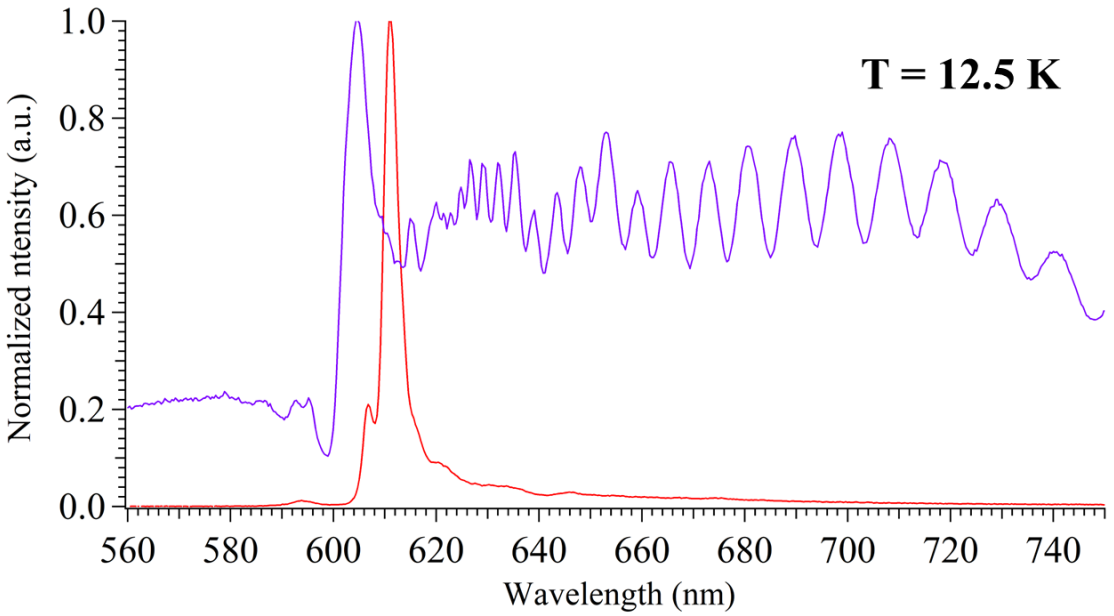

FIGURE 3-15: ***LOW TEMPERATURE PL AND REFLECTIVITY MEASUREMENTS OF OPTIMIZED N=3 CRYSTAL***

Perovskite crystal PL and Reflectivity measurements after completing fine tuning of the chemical formula. As observed, the reflectivity of the perovskite crystal becomes more visible at low temperatures.

Displayed in **Fig. 3-15**, the PL and Reflectivity measurements of the crystal at low temperature (**12.5 K**). The PL peak is as expected blueshifted and at **610 nm**, because of the perovskite's phase transition properties [25]. This will be backed up experimentally as well, a few pages ahead. As aforementioned, the reflectivity of the crystal is now much clearer due to the temperature difference and has its excitonic emission at around **600 nm**, which is an acceptable shift from the PL's peak as it was already stated in the theoretical part.

Conclusively, to accurately measure the reflectivity of those crystals proves difficult due to mainly three facts. The crystals scatter white light too much, thus being difficult to focus the signal of the measurement. Secondly, the crystals tend to grow onto the substrate in angled positions, also making the signal hard to acquire -as already shown and explained from the microscope and SEM images-. Lastly, in grazing incidence -which will be approached in the second chapter- the perovskite crystals are susceptible to polarization changes and this tends to matter when the light angle of incidence gets larger.

3.4.4 Perovskite characterization at 60^0 incidence

Before going directly to the high-angle reflectivity measurements, we first tried to achieve an angle of 60^0 so as to get a better look at how the exciton is behaving when the angle of incidence gets larger.

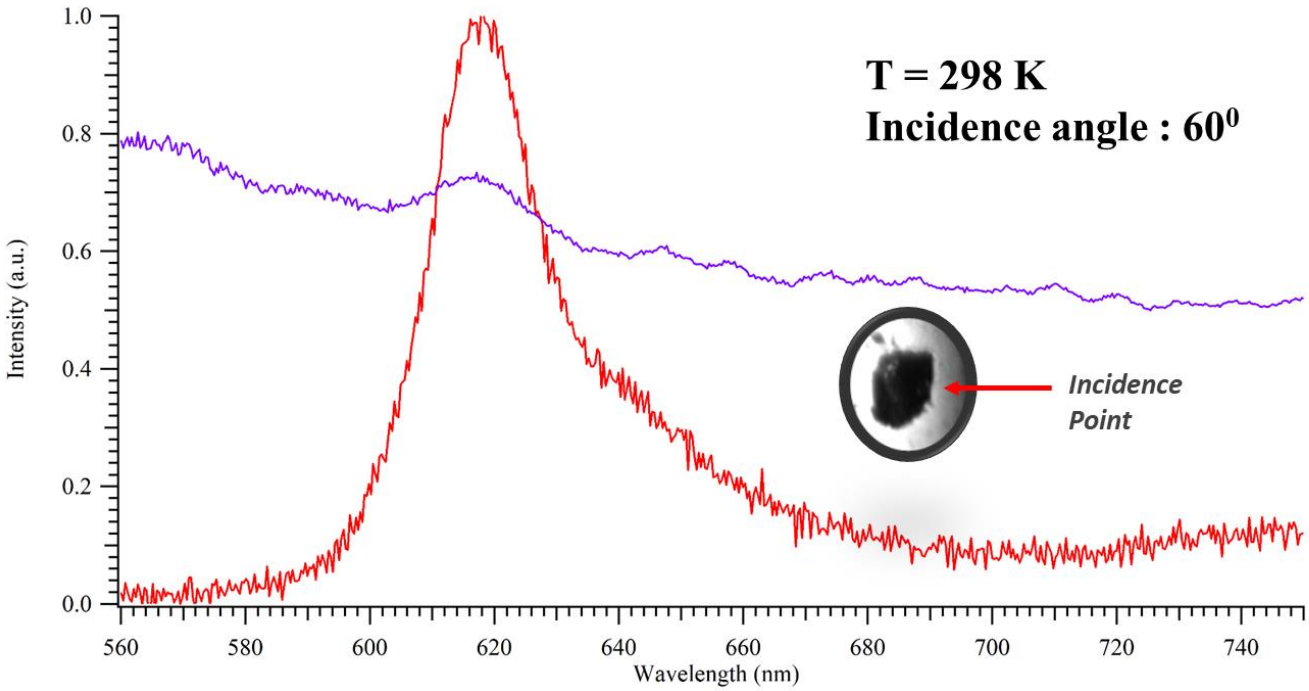

FIGURE 3-16: ***60^0 PL/REFLECTIVITY/IMAGING MEASUREMENT OF N=3 PEROVSKITE***
This plot presents 3 different measurements. PL/Reflectivity/Imaging. Using the 60^0 optical setup, we can accurately pinpoint a perovskite crystal and image it with the help of a camera. Afterwards, we introduce laser to measure the PL of the crystal and white light to measure its reflectivity. The exciton emission is very pure as it only contains 618 nm emission. The reflectivity displays a "peak" also at 618 nm with oscillations following.

The plot from **Fig. 3-16**, contains 3 different measurements that were all done onto the same exact point. Using setup no.2, we are able to accurately pinpoint one individual crystal using incident white light and collecting it into an imaging camera. Afterwards, the alignment of the setup allows us to hit a particular crystal with either laser or white light and collect both PL and Reflectivity measurements at almost the same time.

From the data presented, we can extract that the exciton emission of the particular crystal is as expected at n =3 – 618 nm. The reflectivity is more broadened due to the angle of incidence being much larger than normal, but the exciton feature is still visible. It was anticipated for the larger angle to have lesser intensity signals but still, the measurements are similar. The reflectivity oscillations information is somewhat debatable if they are visible in this measurement, but it can be visible in other measurements. This can also be attributed to the large angle of incidence, creating more losses in the "cavity" between the crystal and the substrate. This one crystal point dataset that was made, allows us to make the assumption that

the exciton and oscillations information in reflectivity is retained through larger angles of incidence.

Continuing below, the PL and Reflectivity temperature dependence measurements are displayed in **Fig. 3-17**.

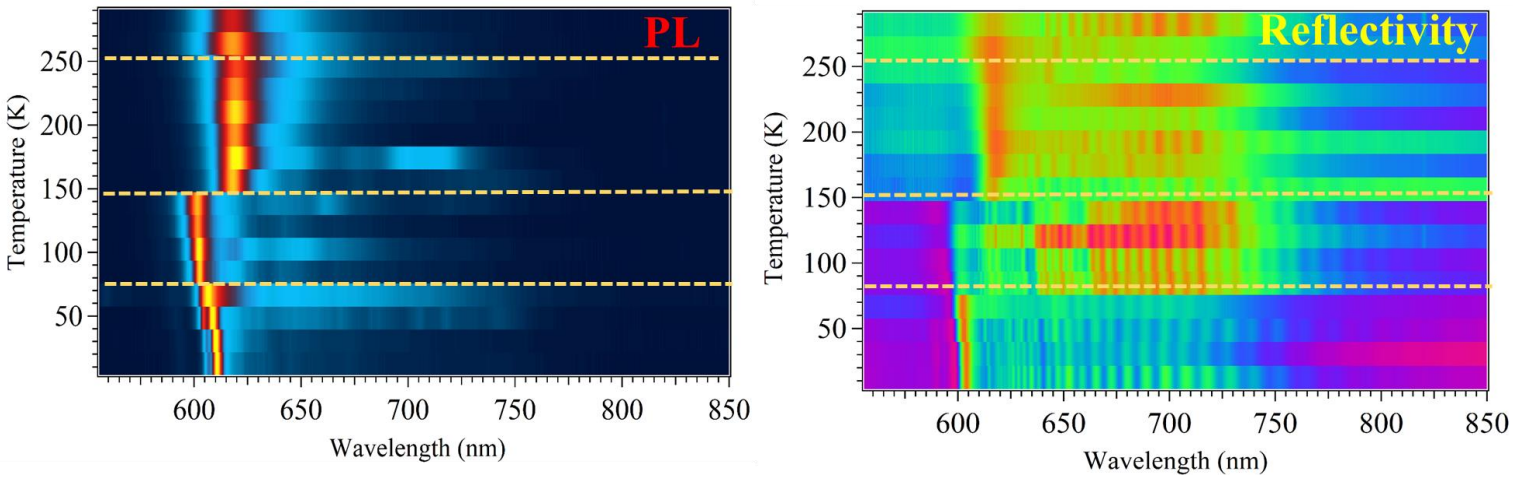

FIGURE 3-17: ***TEMPERATURE DEPENDENCE PL AND REFLECTIVITY MEASUREMENTS FOR N = 3 PEROVSKITE***

Temperature dependence PL (Left) and Reflectivity (Right) measurements. The resulted data are exactly as anticipated. Both theoretical phase transitions of the perovskite crystal are clearly visible at 140K and 50K.

The crystal behaves as expected at room temperature, having an exciton emission of 618 nm. We can observe 3 separate phase transitions for this material and are certain that the structure somehow changes. Yet, it is still unknown what changes the structure undergoes. However, we do know that the temperatures and emissions for the transitions are as follows:

1. **~260 K → Emission wavelength from 620 nm to 617 nm.**
2. **~150 K → Emission wavelength from 617 nm to 601 nm.**
3. **~50 K → Emission wavelength from 601 nm to 610 nm.**

Also known is the fact that at the first phase transition, the organic component of the perovskite crystal shrinks in size and at the second phase transition the inorganic component also shrinks in size. Little is known about the 3rd phase transition and its structural changes.

PL power dependence measurement of the crystals also took place. As **Fig. 3-18** exhibits, the perovskite crystal has approximately 1-1 power-PL intensity behavior as predicted. From these measurements, important result was the materials tolerance to power vs its optical behavior. The two datasets consist of power going from 100 μW to 900 μW upwards and the in the same manner downwards.

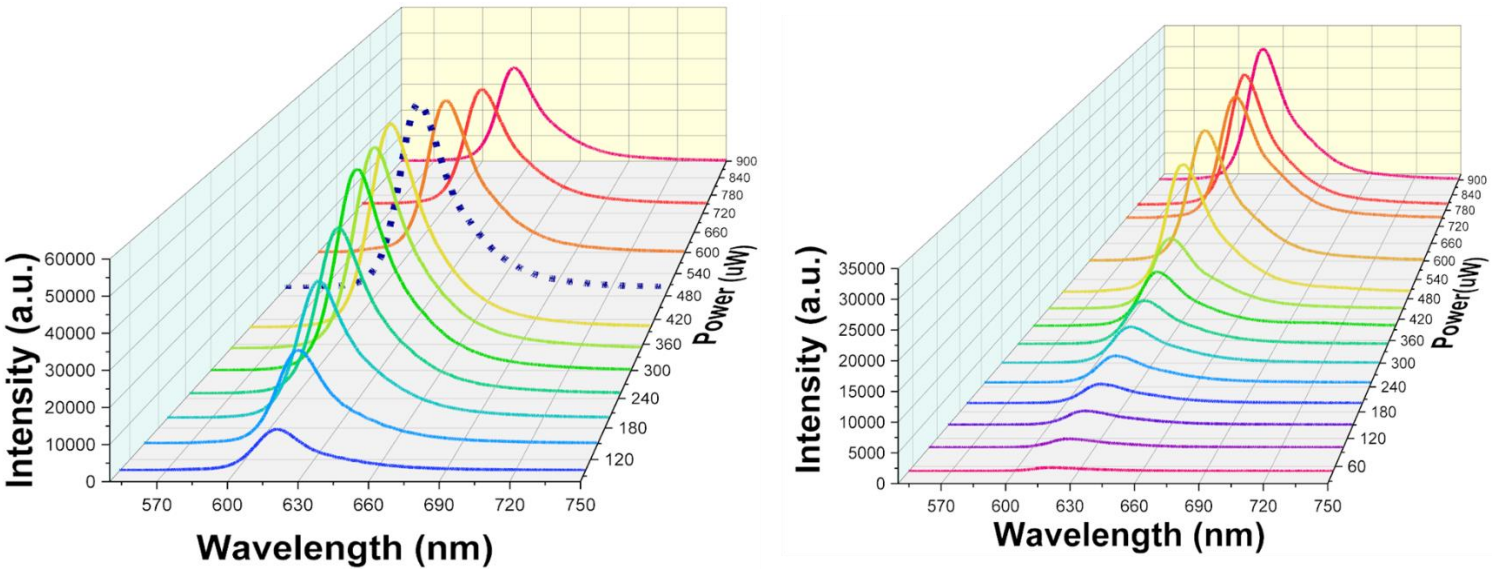

FIGURE 3-18*: POWER DEPENDENCE PL MEASUREMENTS FOR N = 3 PEROVSKITE*
Power dependence PL measurements of the n=3 crystal. The crystal has an almost perfect 1-1 Power-Intensity behavior.

3.4.5 Conclusions

The perovskite crystal was put through an extended number of measurements, both structural (XRD, SEM) as well as optical (PL, Reflectivity at room and low temperatures, resulting in a pure excitonic emission of **620 nm** and a clearly layered rectangle structure of thicknesses varying from **2-8 μm**. The material is now optimized and can be introduced into a cavity (or on a half-cavity) in order to explore strong coupling. At the 60^0 incidence measurements, we provide the result of the perovskite crystal's PL and Reflectivity emission and state that PL is visible and has the correct emission and reflectivity is broadened but still exhibits its features. The chemical formula as well as the fabrication method proved successful with little parameters to control. Main tuning happened to the chemical composition of the formula, temperature control and also different types of magnets were used so as to find a good result. In the next two chapters, two separate techniques are examined. The first one is introducing the perovskite crystal onto a DBR, creating a half-cavity for high angle reflectivity measurements towards strong coupling. The second, introduces the perovskite crystal into a standard cavity between 2 DBRs for again for strong coupling.

4 Perovskite Half-Cavity strong coupling realization

Concluding from the previous chapter, the perovskite crystal is now a good candidate to be introduced into a cavity in order to realize strong coupling. Main advantage of this crystal, is how easy and fast we can formulate and fabricate a high-quality sample for further investigations with facile solution process and low-cost components. In this chapter, the general idea was to a fabricate thin perovskite crystals on top of a DBR, which was specifically made to produce a mode matching this particular crystal's emission, so as to observe polariton through reflectivity measurements at grazing incidence. At first, we will show the DBR's spectra and high-angle reflectivity evanescent mode realization.

4.1 DBR characterization (TE vs TM Polarization)

In this subchapter, we will, theoretically simulate and calculate as well experimentally compare the custom made DBR. All of the simulations and modeling was done in the program **Igor Pro** and the code itself was provided by colleague **Dr. Giannis Paschos**

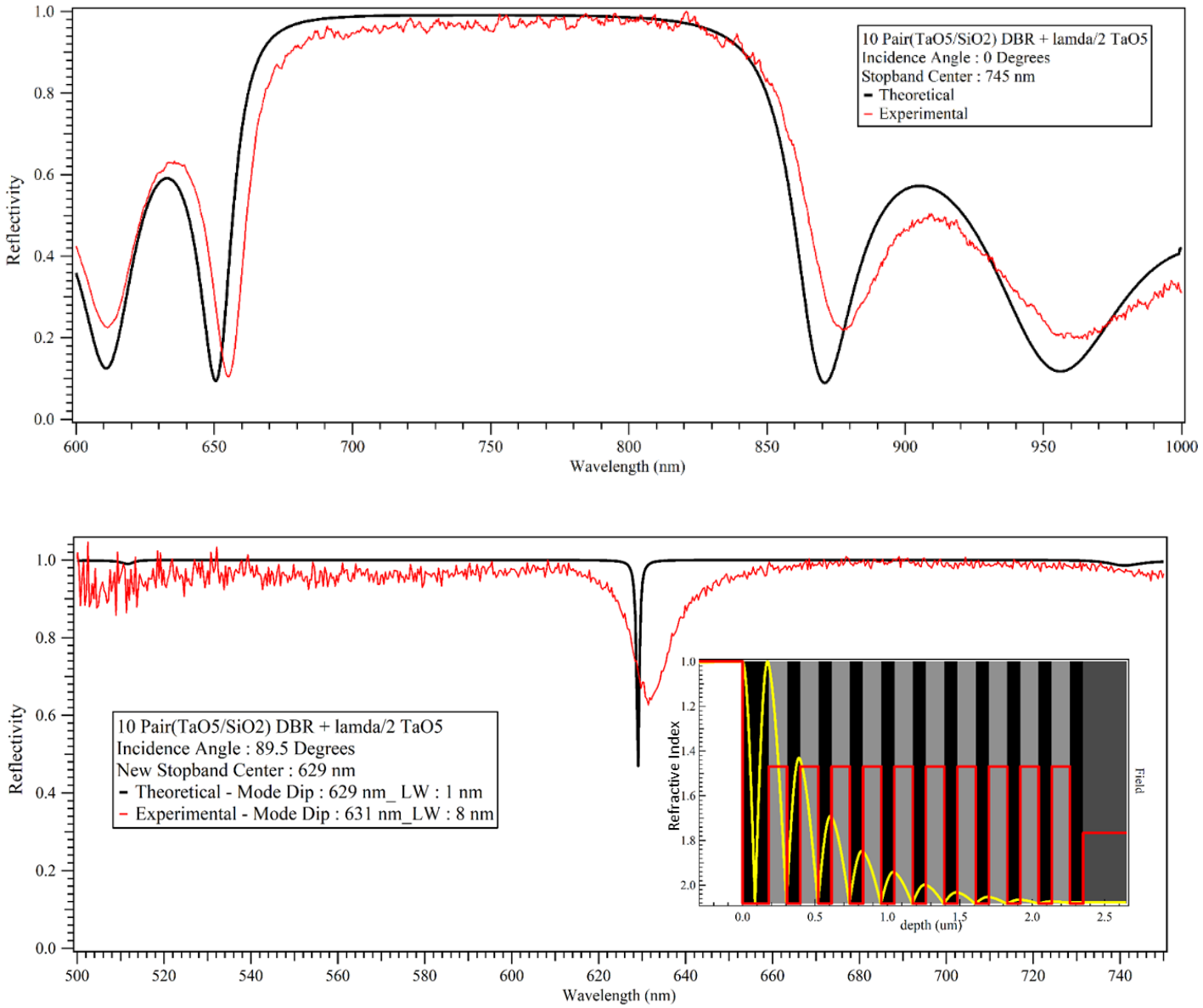

FIGURE 4-1: ***DBR SIMULATION VS EXPERIMENT ON NORMAL AND GRAZING INCIDENCE***

Upper Figure: Theoretical vs Experimental normal incidence Reflectivity measurement of the custom made 10 pair (TaO5/SiO2) + a λ/2 TaO5 layer on top. The middle stopband was calculated to be at 745 nm. Lower Figure: Theoretical vs Experimental 89.5^0 incidence Reflectivity measurement of the custom made DBR and calculated Field Distribution. The difference between the dips is very little, suggesting high quality DBR build. The expected nodes and antinodes in the field distribution are also apparent, showing a node at air/first layer interface followed by antinode and so on.

As we can see from the upper **Fig. 4-1**, the custom made DBR reflectivity measurement matches almost perfectly by its theoretically simulated plot slightly shifted by 4 nm. At grazing incidence, the differences between the simulation and the experiment are the linewidth of the modes which can be attributed to the fact the in the simulation we can just have one and only angle input whereas in the actual experiment we cannot have that accuracy. In actuality, even at grazing incidence, we cannot have just one angle, we have a range of angles of around $89^0 \pm 1^0$. Therefore, the experimental mode is broadened compared to the theoretical one. The stopband has its center at 745 nm with a slight wavelength shift of 2 nm, which can be attributed to a slight thickness difference of the real fabricated DBR.

From the lower **Fig. 4-1**, we exhibit the calculated high-angle reflectivity of the same DBR as well as its experimental counterpart, comparing them with the state of the art. The TE polarized mode is most evident with a difference that in the experimental measurement, we cannot see any of the Bragg modes -most likely they are merged with the background noise- and the mode dip is slightly moved from 629 nm to 631 nm.

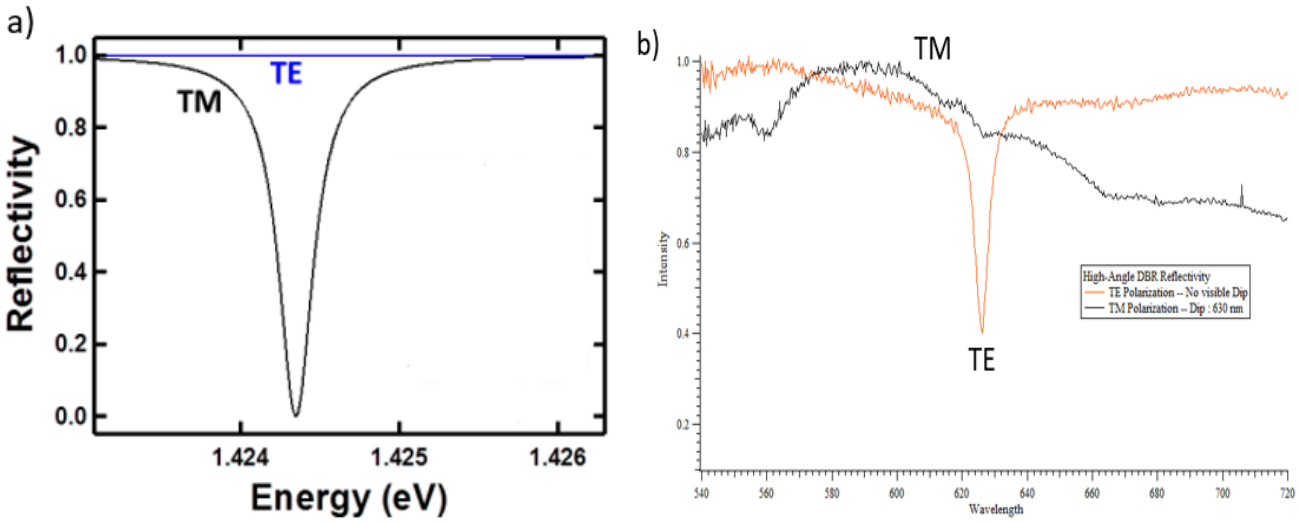

FIGURE 4-2*: TE-TM COMPARISON FOR DBR REFLECTIVITY MODE REALIZATION*

Polarization Dependent reflectivity displaying the mode that appears only in the critical angle of ≈89 Degrees.

a) Calculated Reflectivity of a 25 pair GaAs/AlGaAs DBR system realizing the evanescent mode in TM Polarization and not realizing it in the TE Polarization.

b) Experimentally calculated reflectivity of a 10 pair SiO_2/TaO_5 DBR system

From **Fig. 4-2**, we provide the necessary and clear evidence of the critical angle polarization dependence. With setup no. 3, by having the polarizer fixed at TM polarization, we hit the DBR at grazing incidence resulting in no resonant mode and reflectivity going to 1– *black line at*

(b)-. However, when the polarizer is changed to a fixed TE polarization, the resonant mode is now supported and is a clearly exhibited feature. Of course, the polarization of modes is swapped due to the aforementioned λ/2 thickness stack we have on our DBR structure.

Conclusively, the experimental part of the Brewster-Angle half-cavity mode paid the expected results. The fabricated DBR with the λ/2 thick Ta_2O_5 on top, clearly provides the TE polarization mode dip at **630 nm** (close to the perovskite's 620 nm exciton emission) and with linewidth of **8 nm**. As such we dive into the application of introducing the perovskite crystal -fabricated as explained- to the custom made DBR so as to produce polariton state.

4.1.1 High-Angle Characterization

Having established a fabrication technique as well as non-normal incidence measurements for the material, we now dive onto the one of the two techniques for polariton state realization. The first method is inspired from the idea of the open cavity SCR approach [75,76]. The end goal for this perspective, was to successfully embed thin layer perovskite crystals, on top of the tailored DBR so as to inspect if it can attain SCR as a system. This point of view brings forth some advantages as well as some disadvantages. Mainly, the perovskite crystal sample is very easy to fabricate and takes little time to do so as well as it is a low-cost method. In addition, as the name "open-cavity" suggests, we only need one DBR for this system to work instead of two as it is in the standard cavity approach, need only to change the angle of light incidence to achieve the critical "Brewster-Angle". Last, this method provides only one resonant mode, similarly to a microcavity. The first attempts are seen in **Fig. 4-3** below.

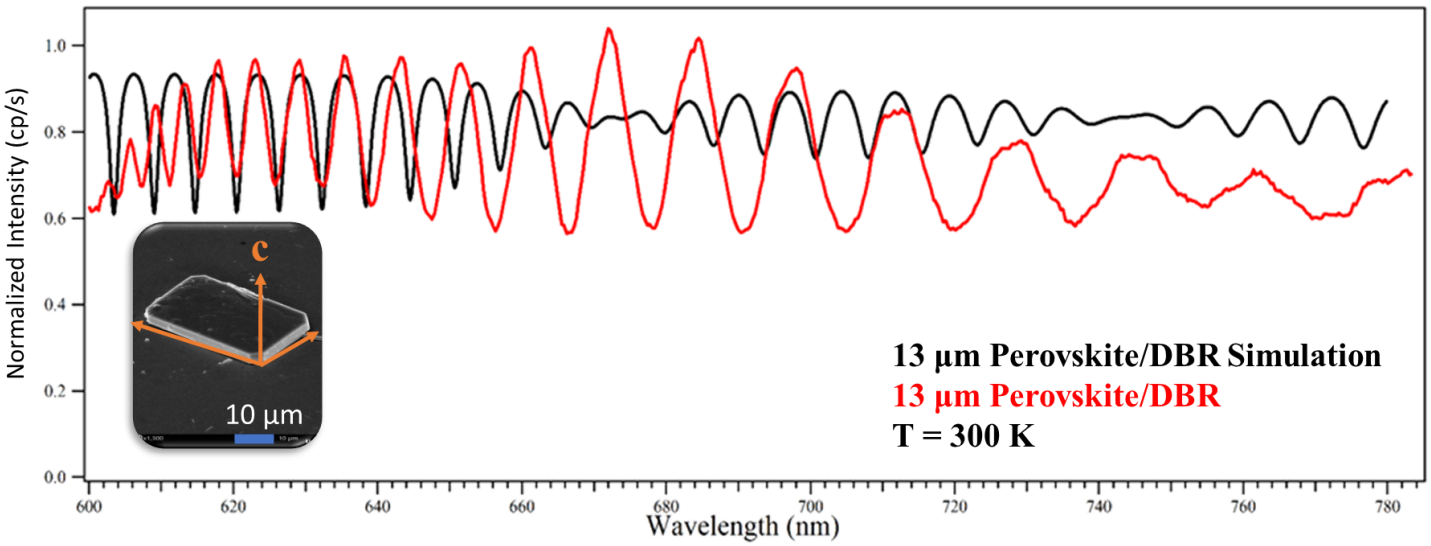

FIGURE 4-3*: SIMULATION(BLACK) AND EXPERIMENTAL(RED) DATA OF A DBR+PEROVSKITE CRYSTAL SYSTEM AT GRAZING INCIDENCE -THICK CRYSTAL-.*

In this figure, we can see the grazing incidence reflectivity measurement of the perovskite crystal. In this sample point, the perovskite layer is way too thick -approximately 13 μm- and this results to two main facts. The DBR mode Dip cannot be detected and the only detectable signal is the oscillations created by the perovskite-DBR "cavity".

From this Figure, we have successfully embedded the perovskite material on top of the DBR. Initial tries prove that we can actually measure the perovskite material successfully. To support this claim, we have made simulations with the exact same DBR system, but on top of it we have incorporated a QW of similar optical parameters with those of the perovskite crystal -at the best of our capabilities- and have assimilated the same thickness with the experimental crystal. From the **Fig.4-3**, we provide qualitative evidence that the modeling of the system is -at least partially- successful, suggesting that with the same simulated perovskite thickness as the crystal's – approximately **13 μm** by simulation's calculations-, we observe the same behavior. This raises the need to make the perovskite crystal as thin as possible so as to minimize the losses that arise from the crystal's scattering and observe the system in more depth. Note for **Fig. 4-3** as well as the next two graphs (**Fig. 4-4**), we can observe a kind of beating behavior in certain wavelengths. For example, at wavelengths 670-680 nm, we can see this behavior. It is assumed to happen because of the two polarization frequencies having phases close to one another. As such, as the two waves propagate, the two phases inevitably become opposite at one time, producing those beatings.

In the **Fig. 3-22** below, we managed to achieve somewhat better results. As displayed, the new tries of the system exhibit experimental thicknesses of the crystal at around **7 μm** and **2 μm**. In those measurements, the oscillations are still visible but clearly less than before, indicating a thinner perovskite sample. By comparing the model with the experiment, we come to assume

that the dip realized at 620 nm in (a) and 630 nm (b) is most likely purely the mode dip. The reason it has changed is most probably because of the crystal's thickness difference.

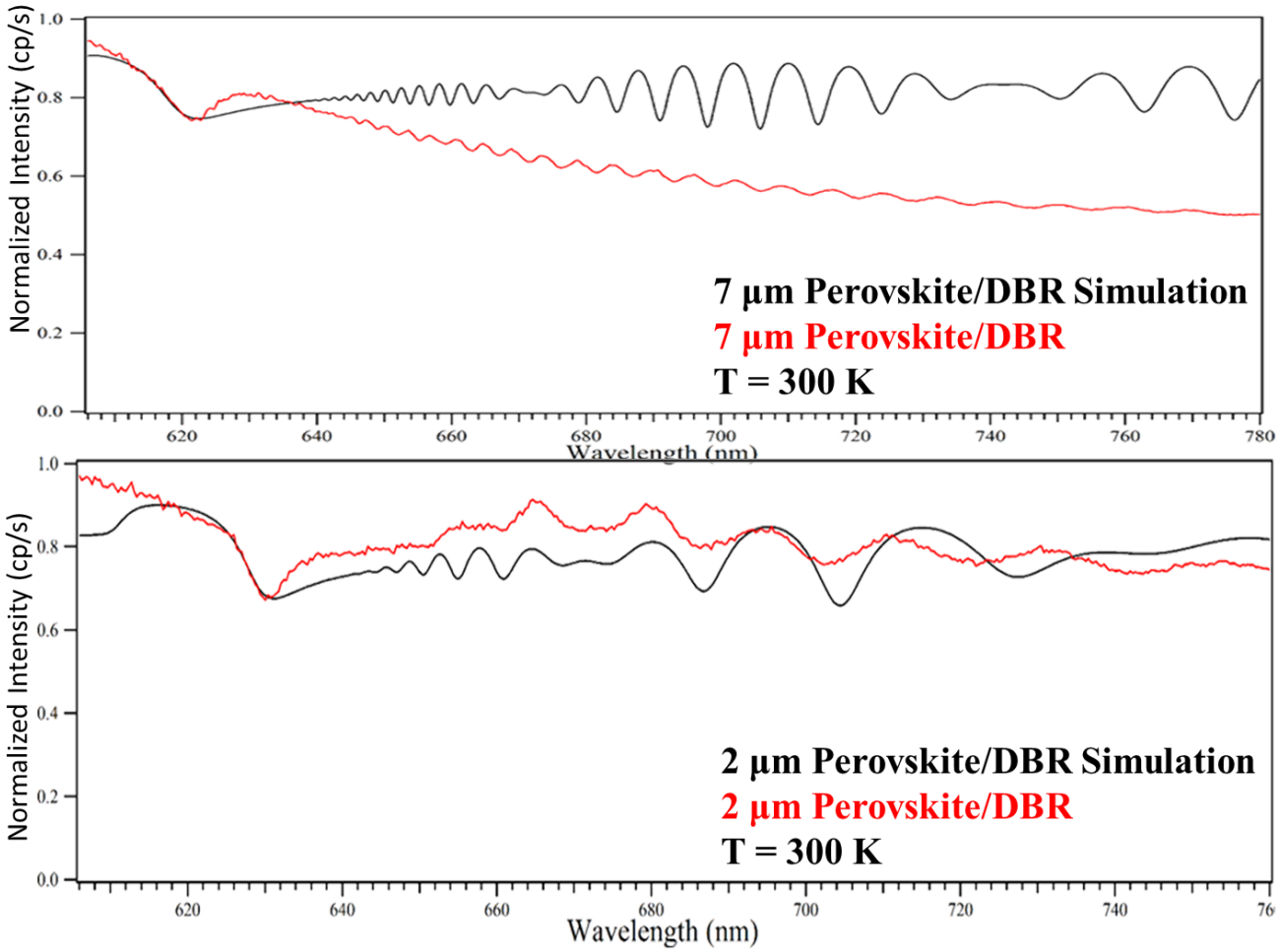

FIGURE 4-4 ***SIMULATION(BLACK) AND EXPERIMENTAL(RED) DATA OF A DBR+PEROVSKITE CRYSTAL SYSTEM AT GRAZING INCIDENCE -THINNER CRYSTAL-.***

As displayed in the figures above, we were able to manage fabricating a perovskite crystal sample that was of thinner nature. Specifically, in (a), we can see that the exciton-mode dip is now visible due to the thinner perovskite crystal's less scattering – around 7 µm- and in (b) the perovskite is even thinner at around 2 µm. The oscillations are visible in both figures, although in (b) they are clearly less because of the thickness being less.

Unfortunately, the fabrication method plus the chemical formula, does not allow us to fully control the size of the perovskite crystals and thus, we were not able to produce a thin perovskite Brewster Cavity System. The best thickness achieved, was a thickness of 2 µm. In spite of this, we qualitatively simulate the results with a Perovskite crystal of 150 nm thickness to provide insight as per the polariton state realization which is seen in the figure below.

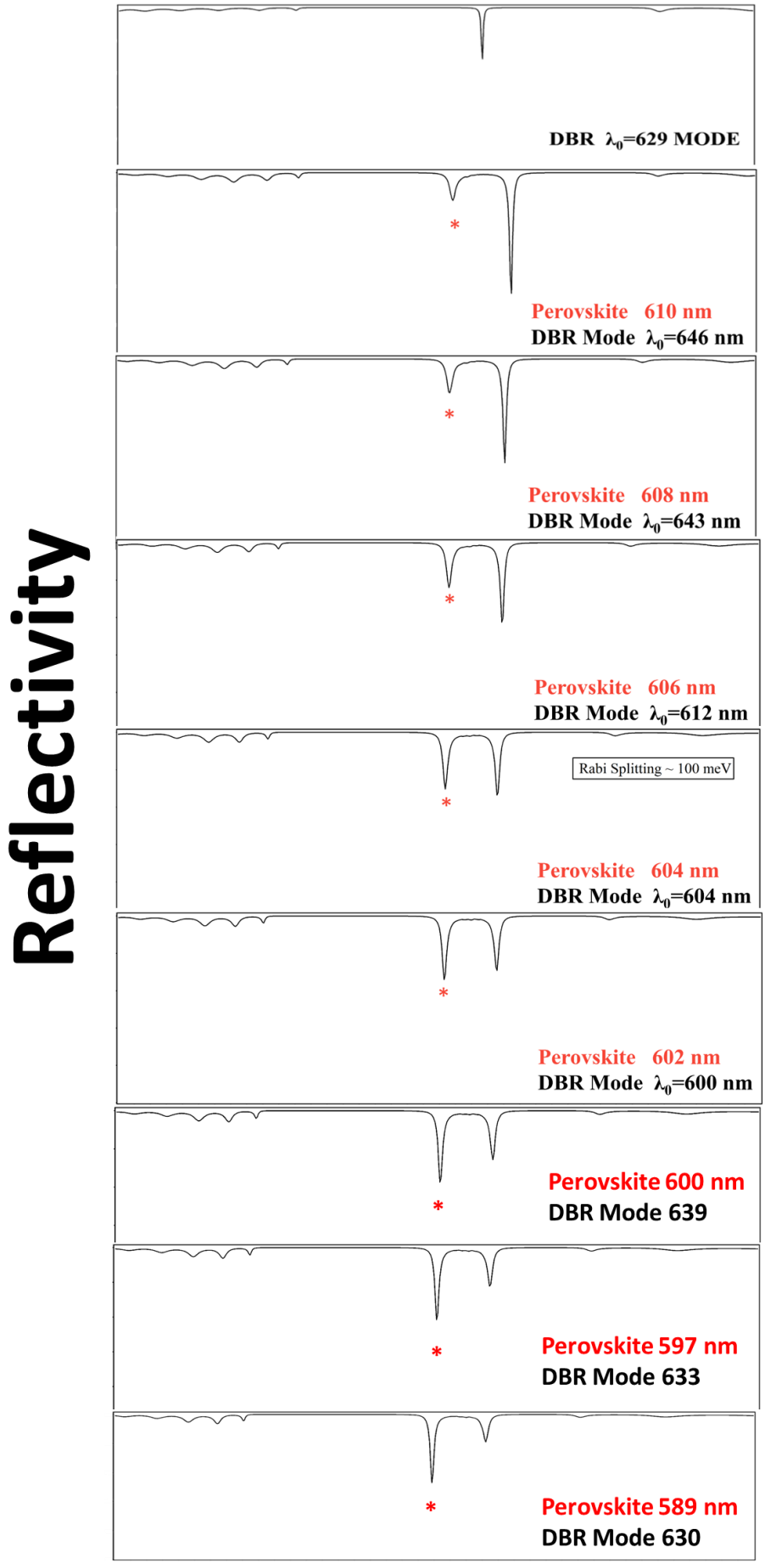
DBR λ_0=629 MODE
Perovskite 610 nm
DBR Mode λ_0=646 nm
Perovskite 608 nm
DBR Mode λ_0=643 nm
Perovskite 606 nm
DBR Mode λ_0=612 nm
Rabi Splitting ~ 100 meV
Perovskite 604 nm
DBR Mode λ_0=604 nm
Perovskite 602 nm
DBR Mode λ_0=600 nm
Perovskite 600 nm
DBR Mode 639
Perovskite 597 nm
DBR Mode 633
Perovskite 589 nm
DBR Mode 630
Reflectivity
Wavelength (nm)

FIGURE 4-5*: DBR + QW HALF-WAVE LAYER THICKNESS SCR SIMULATION*

*These plots, are a simulation of a 150 nm Perovskite with 620 nm emission, embedded on top of the DBR structure. The y-axis is many different plots stacked on top of each other for easier observation. By changing only, the DBR's stopband center wavelength emission, we can tune the Brewster-Cavity mode in order to approach the exciton's wavelength emission. As we can see in the first plot, only the DBR's mode is displayed. In the next plot, we have embedded in the simulation the Perovskite layer 620 nm emission and immediate interaction can be seen, as the Perovskite dip appears at **610 nm** and the mode at **646 nm**. Tuning the mode even closer, produces the behavior we would expect from strong coupling, seeing the two dips that approach at a minimum distance which gives the **Rabi splitting of 100 meV** and open their distance again.*

In this figure, we present a simulation reflectivity measurement which contains the actual DBR structure but instead of perovskite n =3 crystal, we have embedded a Perovskite layer of the 150 nm thickness and 620 nm exciton emission. As displayed at first, the DBR mode can be seen at 629 nm and when we incorporate the Perovskite layer, the two dips that appear are at 603 nm (QW emission) and 647 nm (mode).

We can clearly see from **Fig. 4-6**, that by incorporating a thin layer of the exciton medium, we can directly see the system realizing SCR with **Rabi splitting Energy at: 100 meV**, which is an impressive number. By correlation, we can assume that our system containing the perovskite crystal needs only better thickness tuning for this project's successfulness.

4.1.2 Conclusions

Summarizing, this procedure can prove very promising if the necessary adjustments are made. The perovskite crystal's thickness proved problematic for this SCR approach, measuring from 2-13 μm as well as problematic is the reflectivity behavior of the perovskite due to its high scattering. Best thickness achieved for the perovskite crystal was 2 μm and unfortunately we needed to tune it down to at least the hundreds of nanometers. Even so, many steps have been achieved for this project and by changing the thickness of the active layer, we could safely assume that we can provide a system producing polariton state at room temperature.

5 Perovskite cavity Room Temperature strong coupling realization

In this third and final chapter, we dive into the standard situation for Strong Coupling realization. The perovskite crystal provides us with a very stable exciton emission at room temperature which is already proven above and is structurally suitable to be introduced into a DBR cavity. This chapter was a collaboration between myself and my Ph.D. candidate. The measurements provided below were done by **Mr. Emmanouil Mavrotsoupakis** with the perovskite crystal that was optimized by through this thesis.

5.1.1 Cavity Modes

In this subchapter, we present a DBR microcavity with n = 3 perovskite crystal introduced between it. The total dispersion energy of the system is as follows:

So, to calculate the length of a cavity, we simply need to fine the arithmetic values of 2 consecutive mode wavelength peaks at zero momentum energy and insert them to **eq. 3-3**.

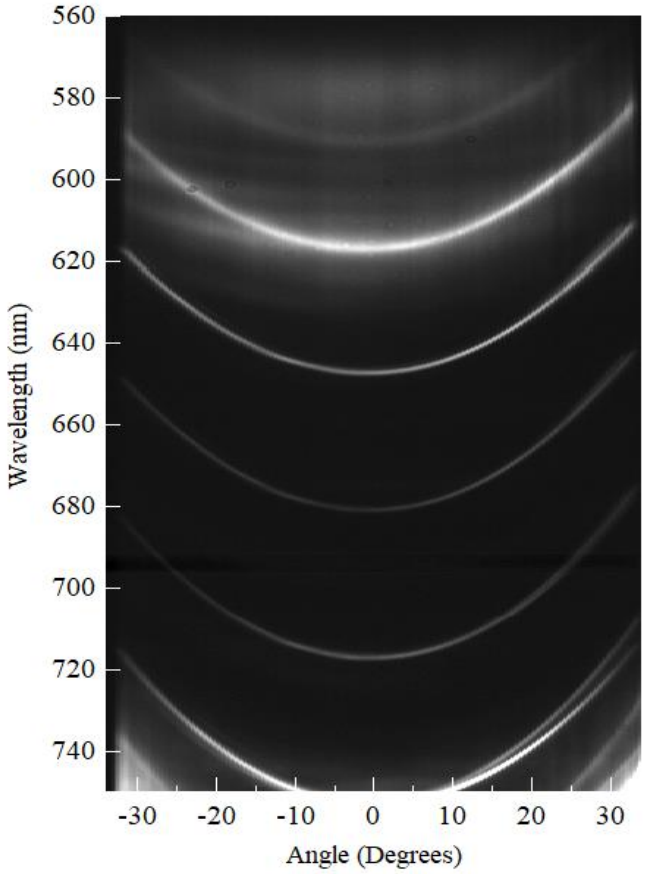

FIGURE 5-1: *DBR-PEROVSKITE N = 3 CAVITY MODES*

Room Temperature Dispersion measurement of the Perovskite Cavity which mostly displays the cavity modes that are realized inside the cavity. The number of modes in the cavity, indicates that this particular cavity system has a relatively high thickness.

As seen from the figure above, this particular cavity thickness has:

$L_c \approx 3.5$ μm with the number of modes being 6 in total. The 2 modes distance **$\Delta d = 40$ nm** was acquired from mode with wavelength peak at 680 nm and its consecutive 720 nm. The first Bragg mode of the cavity is also visible at 610 nm. However, the exciton peak -which would be at n=3 emission of 620 nm- is not visible.

5.1.2 Strong Coupling

Moving forward, on a second point of the same sample as above, we acquire a dispersion measurement seen onto the figure below.

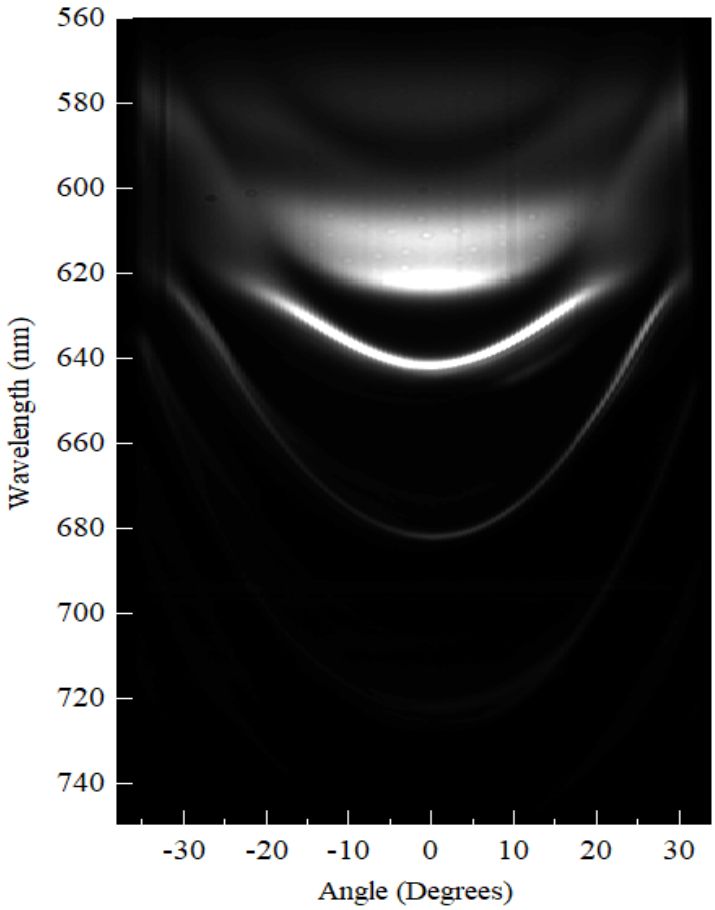

FIGURE 5-2 *DBR-PEROVSKITE N = 3 STRONG COUPLING REGIME*

Room Temperature Dispersion measurement displaying the Perovskite cavity system in the strong coupling regime. Perovskite n = 3 crystal's exciton emission is visible at 620 nm. At high angles the 2 modes' (640nm-curvature observed at 15^0 and 680 nm-curvature observed at 25^0) anticrossing is clearly exhibited, proving that the system has indeed realized a polariton state.

The system is clearly in the strong coupling regime. Here, the exciton emission of the perovskite crystal is clearly visible at 620 nm which is now the Upper Polariton Branch (UPB). We can also observe that 2 cavity modes anticross with the exciton providing Rabi splittings of **100meV (1^{st} LPB) and 75 meV (2^{nd} LPB).** Evidently the perovskite cavity system is

capable to produce polariton state at room temperature with two modes (LPB) interacting strongly at the same time with the exciton (UPB).

5.1.3 Conclusions

In summary, the DBR-Perovskite cavity system, produced a 3.4 μm thick cavity as we calculated. Even so, the crystal's formula and fabrication technique allowed this cavity to achieve **polariton state** at **room temperature** with two separate modes strongly interacting with the exciton with **Rabi splitting of 100 meV and 75 meV**. As such we evidently prove that this system can effectively and directly realize a polariton state at ambient environments and is in general a quite competent system taking into account its simple fabrication and low-cost chemical ingredients.

4. Conclusions

Concluding this thesis, the Perovskite n = 3 crystal has been extensively analyzed. The fabrication and process suggestion for the material was made by two distinct methods that were 1) Liquid Exfoliation and 2) Solution method. From the liquid exfoliation method, the results were consistently difficult. Through PL Reflectivity, microscope and SEM measurements we proved that the crystal was not providing good thickness values (mostly 8-14μm) or correct shape. Due to more parameters, such as spin coating times/speeds as well as correcting amounts of protection polymers, this method proved very difficult to control overall. On the contrary, the second method that was followed was much more fruitful. Through various structural characterization of the crystal such as XRD and SEM images, we concluded that the material was formulated to give high quality results. The optical measurements, such as PL or Reflectivity were also very conclusive and abided by the theory considerably, by producing stable room temperature n = 3 (620 nm) exciton emission as well as having all the visible phase transitions in temperature dependence measurements. After the perovskite crystal was successfully optimized with a crystal thickness of 2-3.5 μm, it was implemented into two different cavity methods in order to achieve polariton state. Many trials have been completed so as to implement this material for half-cavity polariton applications with its advantages being: less growth steps (because we only need one DBR) and easy resonant mode realization (provided the angle of incidence of light is the correct). However, additional work is required to fully realize this technique for polariton applications because of certain disadvantages that originate mainly from: perovskite crystal's difficult reflectivity measurements due to its high scattering as well as the need to overcome the tricky situation of tuning the thickness of the material with this particular formula. However, the qualitative simulations show that with proper thickness of around the hundreds of nanometers, this technique can have the desired results of realizing strong coupling. This method can surely be approached and in the end be implemented for polaritonic applications as it was confirmed through qualitative simulations of a similarly behaving quantum well onto the DBR. Finally, the second technique used was the standard DBR cavity system with the optimized perovskite crystal being introduced inside. This system produced a somewhat thick cavity of 3.5 μm with many resonant modes inside. Despite this fact, the whole system was in the end a very successful one, providing polariton state at room temperature.

References

1. Browne, M. (2013). Physics for Engineering and Science (2nd ed.).
2. Griffiths, D. J. (David J. (1999). Introduction to electrodynamics. Prentice Hall.
3. Singh, D. (2015). Fundamentals of Optics (2nd ed.). PHI Learning Pvt. Ltd.
4. Randy O. Wayne. (2013). Light and Video Microscopy (2nd ed.).
5. J.J. Bernard. (1809). Mémoires de physique et de chimie de la Société d'Arcueil (Vol. 2). Société d'Arcueil.
6. On the laws which regulate the polarisation of light by reflexion from transparent bodies. By David Brewster, LL. D. F. R. S. Edin. and F. S. A. Edin. In a letter addressed to Right Hon. Sir Joseph Banks, Bart. K. B. P. R. SPhil. Trans. R. Soc.105125–159 http://doi.org/10.1098/rstl.1815.0010
7. Marghany, M. (2022). Retrieving Minerals and Rocks in polarimetry Microwave Remote Sensing data. Advanced Algorithms for Mineral and Hydrocarbon Exploration Using Synthetic Aperture Radar, 171–201. https://doi.org/10.1016/B978-0-12-821796-2.00006-9
8. Li, F. (n.d.). Fabrication and characterization of ZnO-based microcavities working in the strong coupling regime: polariton laser. https://tel.archives-ouvertes.fr/tel-00944656
9. R. S. Knox, Theory of excitons, Solid state physics (Ed. by Seitz and Turnbul, Academic, NY), v. 5, 1963.
10. Yu, P.Y., Cardona, M. (2010). Electronic Band Structures. In: Fundamentals of Semiconductors. Graduate Texts in Physics. Springer, Berlin, Heidelberg. https://doi.org/10.1007/978-3-642-00710-1_2
11. Rosencher, E., & Vinter, B. (2002). Optoelectronics (P. Piva, Trans.). Cambridge: Cambridge University Press. doi:10.1017/CBO9780511754647
12. Chatterjee, S.; Ell, C.; Mosor, S.; Khitrova, G.; Gibbs, H.; Hoyer, W.; Kira, M.; Koch, S. W.; Prineas, J.; Stolz, H. (2004). "Excitonic Photoluminescence in Semiconductor Quantum Wells: Plasma versus Excitons". Physical Review Letters **92**.
13. Fox, Mark & Ispasoiu, Radu. (2017). Quantum Wells, Superlattices, and Band-Gap Engineering. 10.1007/978-3-319-48933-9_40.
14. Austerlitz, H. (2003). Analog Signal Transducers. Data Acquisition Techniques Using PCs, 6–28. https://doi.org/10.1016/B978-012068377-2/50002-4.
15. M. Sumetsky, "Mode localization and the Q-factor of a cylindrical microresonator," Opt. Lett. 35, 2385-2387 (2010)
16. Orfanidis, Sophocles J. (2016). Electromagnetic Waves and Antennas. ECE Department, Rutgers University.
17. Rubén Mas-Ballesté et al. (2011). 2D materials: to graphene and beyond. Nanoscale, 1, 20–30.
18. Castro Neto, A. H., Guinea, F., Peres, N. M. R., Novoselov, K. S., & Geim, A. K. (2009). The electronic properties of graphene. Reviews of Modern Physics, 81(1), 109–162. https://doi.org/10.1103/RevModPhys.81.109.
19. Zhang, Y., Nie, K., Yi, L., Li, B., Yuan, Y., Liu, Z., & Huang, W. (2023). Recent Advances in Engineering of 2D Materials-Based Heterostructures for Electrochemical

Energy Conversion. In Advanced Science. John Wiley and Sons Inc. https://doi.org/10.1002/advs.202302301.
20. Wenk, H.-R., & Bulakh, A. G. (Andreĭ G. (2004). Minerals : their constitution and origin. Cambridge University Press.
21. Bednorz, J. G., & Muller, K. A. (n.d.). Perovskite-type oxides The new approach to high-T, superconductivity.
22. Yaffe, O., Chernikov, A., Norman, Z. M., Zhong, Y., Velauthapillai, A., van der Zande, A., Owen, J. S., & Heinz, T. F. (2015). Excitons in ultrathin organic-inorganic perovskite crystals. Physical Review B - Condensed Matter and Materials Physics, 92(4). https://doi.org/10.1103/PhysRevB.92.045414.
23. Liu, M., Johnston, M. B., & Snaith, H. J. (2013). Efficient planar heterojunction perovskite solar cells by vapour deposition. Nature, 501(7467), 395–398. https://doi.org/10.1038/nature12509.
24. Kim, E. B., Akhtar, M. S., Shin, H. S., Ameen, S., & Nazeeruddin, M. K. (2021). A review on two-dimensional (2D) and 2D-3D multidimensional perovskite solar cells: Perovskites structures, stability, and photovoltaic performances. In Journal of Photochemistry and Photobiology C: Photochemistry Reviews (Vol. 48). Elsevier B.V. https://doi.org/10.1016/j.jphotochemrev.2021.100405.
25. Guo, P., Huang, W., Stoumpos, C. C., Mao, L., Gong, J., Zeng, L., Diroll, B. T., Xia, Y., Ma, X., Gosztola, D. J., Xu, T., Ketterson, J. B., Bedzyk, M. J., Facchetti, A., Marks, T. J., Kanatzidis, M. G., & Schaller, R. D. (2018). Hyperbolic Dispersion Arising from Anisotropic Excitons in Two-Dimensional Perovskites. Physical Review Letters, 121(12). https://doi.org/10.1103/PhysRevLett.121.127401.
26. Mitzi, D. B. (1996). Synthesis, crystal structure, and optical and thermal properties of (C 4H9NH3)2MI4 (M = Ge, Sn, Pb). Chemistry of Materials, 8(3), 791–800. https://doi.org/10.1021/cm9505097.
27. Stoumpos, C. C., Cao, D. H., Clark, D. J., Young, J., Rondinelli, J. M., Jang, J. I., Hupp, J. T., & Kanatzidis, M. G. (2016). Ruddlesden-Popper Hybrid Lead Iodide Perovskite 2D Homologous Semiconductors. Chemistry of Materials, 28(8), 2852–2867. https://doi.org/10.1021/acs.chemmater.6b00847.
28. Mao, L., Stoumpos, C. C., & Kanatzidis, M. G. (n.d.). Two-dimensional Hybrid Halide Perovskites: Principles and Promises.
29. Li, X., Hoffman, J. M., & Kanatzidis, M. G. (2021). The 2D halide perovskite rulebook: How the spacer influences everything from the structure to optoelectronic device efficiency. In Chemical Reviews (Vol. 121, Issue 4, pp. 2230–2291). American Chemical Society. https://doi.org/10.1021/acs.chemrev.0c01006.
30. Collings, I. E., Hill, J. A., Cairns, A. B., Cooper, R. I., Thompson, A. L., Parker, J. E., Tang, C. C., & Goodwin, A. L. (2016). Compositional dependence of anomalous thermal expansion in perovskite-like ABX3 formates. Dalton Transactions, 45(10), 4169–4178. https://doi.org/10.1039/c5dt03263f.
31. Jin, L., Sample, A. D., Sun, D., Gao, Y., Deng, S., Li, R., Dou, L., Odom, T. W., & Huang, L. (2023). Enhanced Two-Dimensional Exciton Propagation via Strong Light-Matter Coupling with Surface Lattice Plasmons. ACS Photonics, 10(6), 1983–1991. https://doi.org/10.1021/acsphotonics.3c00466.

32. Liu, B., Soe, C. M. M., Stoumpos, C. C., Nie, W., Tsai, H., Lim, K., Mohite, A. D., Kanatzidis, M. G., Marks, T. J., & Singer, K. D. (2017). Optical Properties and Modeling of 2D Perovskite Solar Cells. Solar RRL, 1(8). https://doi.org/10.1002/solr.201700062.
33. Byun, J., Cho, H., Wolf, C., Jang, M., Sadhanala, A., Friend, R. H., Yang, H., & Lee, T. W. (2016). Efficient Visible Quasi-2D Perovskite Light-Emitting Diodes. Advanced Materials, 28(34), 7515–7520. https://doi.org/10.1002/adma.201601369.
34. Myae Soe, C. M., Nagabhushana, G. P., Shivaramaiah, R., Tsai, H., Nie, W., Blancon, J. C., Melkonyan, F., Cao, D. H., Traoré, B., Pedesseau, L., Kepenekian, M., Katan, C., Even, J., Marks, T. J., Navrotsky, A., Mohite, A. D., Stoumpos, C. C., & Kanatzidis, M. G. (2019). Structural and thermodynamic limits of layer thickness in 2D halide perovskites. Proceedings of the National Academy of Sciences of the United States of America, 116(1), 58–66. https://doi.org/10.1073/pnas.1811006115.
35. Ishihara, T., Takahashi, J., & Goto, T. (1989). EXCITON STATE IN TWO-DIMENSIONAL PEROVSKITE SEMICONDUCTOR (CIoH21NH3)2PbI4. In Solid State Communications (Vol. 69, Issue 9).
36. Papavassiliou, G. C., Patsis, A. P., Lagouvardos, D. J., & Koutselas, I. B. (1993). SPECTROSCOPIC STUDIES OF (C10H2INH3)2PbI4, (CH3NH3)(CIoH21NH3)2Pb217z (CH3NH3) PbI3, AND SIMILAR COMPOUNDS.
37. Ishihara, T., Takahashi, J., & Goto, T. (1990). Optical properties due to electronic transitions in two-dimensional semiconductors (CnH2n+1NH3)2PbI4. Physical Review B, 42(17), 11099–11107. https://doi.org/10.1103/PhysRevB.42.11099.
38. Tanaka, K., Takahashi, T., Kondo, T., Umebayashi, T., Asai, K., & Ema, K. (2005). Image charge effect on two-dimensional excitons in an inorganic-organic quantum-well crystal. Physical Review B - Condensed Matter and Materials Physics, 71(4). https://doi.org/10.1103/PhysRevB.71.045312.
39. Hong, X., Ishihara, T., & Nurmikko, A. v. (1992). Dielectric confinement effect on excitons in PbI4-based layered semiconductors. Physical Review B, 45(12), 6961–6964. https://doi.org/10.1103/PhysRevB.45.6961.
40. Leguy, A. M. A., Hu, Y., Campoy-Quiles, M., Alonso, M. I., Weber, O. J., Azarhoosh, P., van Schilfgaarde, M., Weller, M. T., Bein, T., Nelson, J., Docampo, P., & Barnes, P. R. F. (2015). Reversible hydration of CH3NH3PbI3 in films, single crystals, and solar cells. Chemistry of Materials, 27(9), 3397–3407. https://doi.org/10.1021/acs.chemmater.5b00660.
41. Grishunin, K., Huisman, T., Li, G., Mishina, E., Rasing, T., Kimel, A. v., Zhang, K., Jin, Z., Cao, S., Ren, W., Ma, G. H., & Mikhaylovskiy, R. v. (2018). Terahertz Magnon-Polaritons in TmFeO3. ACS Photonics, 5(4), 1375–1380. https://doi.org/10.1021/acsphotonics.7b01402.
42. Boulier, T., Jacquet, M. J., Maître, A., Lerario, G., Claude, F., Pigeon, S., Glorieux, Q., Amo, A., Bloch, J., Bramati, A., & Giacobino, E. (2020). Microcavity Polaritons for Quantum Simulation. Advanced Quantum Technologies, 3(11). https://doi.org/10.1002/qute.202000052.
43. Mischok, A., Hillebrandt, S., Kwon, S., & Gather, M. C. (n.d.). Highly efficient polaritonic light emitting diodes with angle-independent narrowband emission.

44. Deng, H., Haug, H., & Yamamoto, Y. (2010). Exciton-polariton Bose-Einstein condensation. Reviews of Modern Physics, 82(2), 1489–1537. https://doi.org/10.1103/RevModPhys.82.1489.
45. Liew, T. C. H., Rubo, Y. G., & Kavokin, A. v. (2014). Exciton-Polariton Oscillations in Real Space. https://doi.org/10.1103/PhysRevB.90.245309.
46. Kavokin, A., Malpuech, G., & Laussy, F. P. (2003). Polariton laser and polariton superfluidity in microcavities. In Physics Letters A (Vol. 306). www.elsevier.com/locate/pla.
47. Kasprzak, J., Richard, M., Kundermann, S., Baas, A., Jeambrun, P., Keeling, J. M. J., Marchetti, F. M., Szymánska, M. H., André, R., Staehli, J. L., Savona, V., Littlewood, P. B., Deveaud, B., & Dang, L. S. (2006). Bose-Einstein condensation of exciton polaritons. Nature, 443(7110), 409–414. https://doi.org/10.1038/nature05131.
48. Deng, H., Haug, H., & Yamamoto, Y. (2010). Exciton-polariton Bose-Einstein condensation. Reviews of Modern Physics, 82(2), 1489–1537. https://doi.org/10.1103/RevModPhys.82.1489.
49. Balslev, I. (1981). Exciton polaritons at surfaces of GaAs. Solid State Communications, 39(2), 359–362. https://doi.org/10.1016/0038-1098(81)90690-6.
50. J. Kusano, Y. Segawa, M. Mihara, Y. Aoyagi, & S. Namba. (1989). Quantum size effect on the exciton polariton in GaAs thin films. Solid State Communications, 72, 215–218. https://doi.org/https://doi.org/10.1016/0038-1098(89)90526-7.
51. Rose, A. H., Dunklin, J. R., Zhang, H., Merlo, J. M., & van de Lagemaat, J. (2020). Plasmon-Mediated Coherent Superposition of Discrete Excitons under Strong Exciton-Plasmon Coupling in Few-Layer MoS2at Room Temperature. ACS Photonics, 7(5), 1129–1134. https://doi.org/10.1021/acsphotonics.0c00233.
52. Gu, J., Chakraborty, B., Khatoniar, M., & Menon, V. M. (2019). A room-temperature polariton light-emitting diode based on monolayer WS2. In Nature Nanotechnology (Vol. 14, Issue 11, pp. 1024–1028). Nature Publishing Group. https://doi.org/10.1038/s41565-019-0543-6.
53. Datta, B., Khatoniar, M., Deshmukh, P., Thouin, F., Bushati, R., de Liberato, S., Cohen, S. K., & Menon, V. M. (2022). Highly nonlinear dipolar exciton-polaritons in bilayer MoS2. Nature Communications, 13(1). https://doi.org/10.1038/s41467-022-33940-3.
54. Zhao, J., Fieramosca, A., Dini, K., Bao, R., Du, W., Su, R., Luo, Y., Zhao, W., Sanvitto, D., Liew, T. C. H., & Xiong, Q. (2023). Exciton polariton interactions in Van der Waals superlattices at room temperature. Nature Communications, 14(1). https://doi.org/10.1038/s41467-023-36912-3.
55. Litinskaya, M., Reineker, P., & Agranovich, V. M. (2006). Exciton-polaritons in organic microcavities. Journal of Luminescence, 119–120(SPEC. ISS.), 277–282. https://doi.org/10.1016/j.jlumin.2006.01.016.
56. Takazawa, K., Inoue, J. I., Mitsuishi, K., & Takamasu, T. (2010). Fraction of a millimeter propagation of exciton polaritons in photoexcited nanofibers of organic dye. Physical Review Letters, 105(6). https://doi.org/10.1103/PhysRevLett.105.067401.
57. Zhang, C., Zou, C. L., Yan, Y., Hao, R., Sun, F. W., Han, Z. F., Zhao, Y. S., & Yao, J. (2011). Two-photon pumped lasing in single-crystal organic nanowire exciton polariton

resonators. Journal of the American Chemical Society, 133(19), 7276–7279. https://doi.org/10.1021/ja200549v.

58. Keeling, J., & Kéna-Cohen, S. (2020). The Annual Review of Physical Chemistry is online at. Annu. Rev. Phys. Chem. 2020, 71, 435–459. https://doi.org/10.1146/annurev-physchem-010920.
59. Su, R., Diederichs, C., Wang, J., Liew, T. C. H., Zhao, J., Liu, S., Xu, W., Chen, Z., & Xiong, Q. (2017). Room-Temperature Polariton Lasing in All-Inorganic Perovskite Nanoplatelets. Nano Letters, 17(6), 3982–3988. https://doi.org/10.1021/acs.nanolett.7b01956.
60. Leguy, A. M. A., Hu, Y., Campoy-Quiles, M., Alonso, M. I., Weber, O. J., Azarhoosh, P., van Schilfgaarde, M., Weller, M. T., Bein, T., Nelson, J., Docampo, P., & Barnes, P. R. F. (2015). Reversible hydration of CH3NH3PbI3 in films, single crystals, and solar cells. Chemistry of Materials, 27(9), 3397–3407. https://doi.org/10.1021/acs.chemmater.5b00660.
61. Bouteyre, P., Nguyen, H. S., Lauret, J.-S., Allard-Trippé, G., Delport, G., Lédée, F., Diab, H., Belarouci, A., Seassal, C., Garrot, D., Bretenaker, F., & Deleporte, E. (2018). Room temperature cavity polaritons with 3D hybrid perovskite - Towards low-cost polaritonic devices. https://doi.org/10.1021/acsphotonics.9b00625.
62. Hossain, A., Bandyopadhyay, P., & Roy, S. (2018). An overview of double perovskites A2B′B″O6 with small ions at A site: Synthesis, structure and magnetic properties. In Journal of Alloys and Compounds (Vol. 740, pp. 414–427). Elsevier Ltd. https://doi.org/10.1016/j.jallcom.2017.12.282.
63. Chen, Y., Shi, Y., Gan, Y., Liu, H., Li, T., Ghosh, S., & Xiong, Q. (2023). Unraveling the Ultrafast Coherent Dynamics of Exciton Polariton Propagation at Room Temperature. Nano Letters. https://doi.org/10.1021/acs.nanolett.3c02547.
64. Masharin, M. A., Shahnazaryan, V. A., Iorsh, I. v., Makarov, S. v., Samusev, A. K., & Shelykh, I. A. (2023). Room-Temperature Polaron-Mediated Polariton Nonlinearity in MAPbBr3 Perovskites. ACS Photonics, 10(3), 691–698. https://doi.org/10.1021/acsphotonics.2c01773.
65. Lourenço, S. A., Figueredo, L. S., da Silva, M. A. T., & Fernandes, R. v. (2023). Effect of incorporation of PbS nanocrystals on optical properties of the hybrid organic-inorganic MAPbI3 perovskite. Synthetic Metals, 297. https://doi.org/10.1016/j.synthmet.2023.117400.
66. Grancini, G., & Nazeeruddin, M. K. (2019). Dimensional tailoring of hybrid perovskites for photovoltaics. In Nature Reviews Materials (Vol. 4, Issue 1, pp. 4–22). Nature Publishing Group. https://doi.org/10.1038/s41578-018-0065-0.
67. Zhou, N., Shen, Y., Li, L., Tan, S., Liu, N., Zheng, G., Chen, Q., & Zhou, H. (2018). Exploration of Crystallization Kinetics in Quasi Two-Dimensional Perovskite and High Performance Solar Cells. Journal of the American Chemical Society, 140(1), 459–465. https://doi.org/10.1021/jacs.7b11157.
68. Gao, Y., Wei, Z., Yoo, P., Shi, E., Zeller, M., Zhu, C., Liao, P., & Dou, L. (2019). Highly Stable Lead-Free Perovskite Field-Effect Transistors Incorporating Linear Π-Conjugated Organic Ligands. Journal of the American Chemical Society, 141(39), 15577–15585. https://doi.org/10.1021/jacs.9b06276.

69. Yin, J., Maity, P., de Bastiani, M., Dursun, I., Bakr, O. M., Brédas, J.-L., & Mohammed, O. F. (2017). P H Y S I C S Molecular behavior of zero-dimensional perovskites. https://www.science.org.
70. Trifiletti, V., Asker, C., Tseberlidis, G., Riva, S., Zhao, K., Tang, W., Binetti, S., & Fenwick, O. (2021). Quasi-Zero Dimensional Halide Perovskite Derivates: Synthesis, Status, and Opportunity. Frontiers in Electronics, 2. https://doi.org/10.3389/felec.2021.758603.
71. Anantharaman, S. B., Stevens, C. E., Lynch, J., Song, B., Hou, J., Zhang, H., Jo, K., Kumar, P., Blancon, J. C., Mohite, A. D., Hendrickson, J. R., & Jariwala, D. (2021). Self-Hybridized Polaritonic Emission from Layered Perovskites. Nano Letters, 21(14), 6245–6252. https://doi.org/10.1021/acs.nanolett.1c02058.
72. Jin, L., Sample, A. D., Sun, D., Gao, Y., Deng, S., Li, R., Dou, L., Odom, T. W., & Huang, L. (2023). Enhanced Two-Dimensional Exciton Propagation via Strong Light-Matter Coupling with Surface Lattice Plasmons. ACS Photonics, 10(6), 1983–1991. https://doi.org/10.1021/acsphotonics.3c00466.
73. Sun, S., Lu, M., Gao, X., Shi, Z., Bai, X., Yu, W. W., & Zhang, Y. (2021). 0D Perovskites: Unique Properties, Synthesis, and Their Applications. In Advanced Science (Vol. 8, Issue 24). John Wiley and Sons Inc. https://doi.org/10.1002/advs.202102689.
74. Wang, S., Chen, Y., Yao, J., Zhao, G., Li, L., & Zou, G. (2021). Wafer-sized 2D perovskite single crystal thin films for UV photodetectors. Journal of Materials Chemistry C, 9(20), 6498–6506. https://doi.org/10.1039/d1tc00408e.
75. Christmann, G., Trifonov, A. v., Tzimis, A., Hatzopoulos, Z., Iorsh, I. v., Baumberg, J. J., & Savvidis, P. G. (2019). High-angle optically accessible Brewster cavity exciton-polaritons. Physical Review B, 99(24). https://doi.org/10.1103/PhysRevB.99.241402.
76. Askitopoulos, A., Mouchliadis, L., Iorsh, I., Christmann, G., Baumberg, J. J., Kaliteevski, M. A., Hatzopoulos, Z., & Savvidis, P. G. (2011). Bragg polaritons: Strong coupling and amplification in an unfolded microcavity. Physical Review Letters, 106(7). https://doi.org/10.1103/PhysRevLett.106.076401.
77. Mahlein, H. F. (n.d.). Generalized Brewster-angle conditions for quarter-wave multilayers at non-normal incidence.
78. Notomi, M. (2010). Manipulating light with strongly modulated photonic crystals. Reports on Progress in Physics, 73(9). https://doi.org/10.1088/0034-4885/73/9/096501
79. Amnon Yariv, & Pochi Yeh. (n.d.). Optical waves in crystals. Propagation and Control of Laser Radiation. Wiley and Sons Inc.
80. Paton, Keith R; Varrla, Eswaraiah; Backes, Claudia; Smith, Ronan J; Khan, Umar; O'Neill, Arlene; et al. (2014). Scalable production of large quantities of defect-free few-layer graphene by shear exfoliation in liquids. University of Sussex. Journal contribution. https://hdl.handle.net/10779/uos.23306465.v1.
81. Li, Z., Young, R. J., Backes, C., Zhao, W., Zhang, X., Zhukov, A. A., Tillotson, E., Conlan, A. P., Ding, F., Haigh, S. J., Novoselov, K. S., & Coleman, J. N. (2020). Mechanisms of Liquid-Phase Exfoliation for the Production of Graphene. ACS Nano, 14(9), 10976–10985. https://doi.org/10.1021/acsnano.0c03916.

82. Coleman, J. N., Lotya, M., O'Neill, A., Bergin, S. D., King, P. J., Khan, U., Young, K., Gaucher, A., De, S., Smith, R. J., Shvets, I. v., Arora, S. K., Stanton, G., Kim, H. Y., Lee, K., Kim, G. T., Duesberg, G. S., Hallam, T., Boland, J. J., … Nicolosi, V. (2011). Two-dimensional nanosheets produced by liquid exfoliation of layered materials. Science, 331(6017), 568–571. https://doi.org/10.1126/science.1194975Jonathan N. Coleman et al., Two-Dimensional Nanosheets Produced by Liquid Exfoliation of Layered Materials.Science331,568-571(2011). DOI:10.1126/science.1194975.
83. Wei, K., Yang, L., Deng, J., Luo, Z., Zhang, X., & Zhang, J. (2022). Facile Exfoliation of the Perovskite Thin Film for Visualizing the Buried Interfaces in Perovskite Solar Cells. ACS Applied Energy Materials, 5(6), 7458–7465. https://doi.org/10.1021/acsaem.2c00948.